Trap mediated piezoresponse of silicon in the space charge limit.

Heng Li

To cite this version:

Heng Li. Trap mediated piezoresponse of silicon in the space charge limit.. Condensed Matter [cond-mat]. Université Paris Saclay (COmUE), 2019. English. NNT : 2019SACLX039 . tel-02319092

HAL Id: tel-02319092
https://theses.hal.science/tel-02319092

Submitted on 17 Oct 2019

universite
PARIS-SACLAY

NNT : 2019SACLX039

ÉCOLE POLYTECHNIQUE
UNIVERSITÉ PARIS-SACLAY

Space charge limited piezo-response of silicon in the presence of electronic traps

Thèse de doctorat de l'Université Paris-Saclay
préparée à L'Ecole Polytechnique

École doctorale n°573 Interfaces : approches interdisciplinaires, fondements, applications et innovation
Spécialité de doctorat: Physique

Thèse présentée et soutenue à Palaiseau, le 19/09/2019, par

M.Heng LI

Composition du Jury :

M. Alois Lugstein Professeur, Technische Universität Wien	Rapporteur
M. Paul Hurley Professeur, Tyndall National Institute at University College Cork	Rapporteur
M. Francois Rochet Professeur, Sorbonne Université (UMR 7614)	Examinateur
M. Yvan Bonnassieux Professeur, Institut Polytechnique de Paris/CNRS (UMR 7647)	Président
M. Alistair Rowe Chargé de Recherche, Institut Polytechnique de Paris/CNRS (UMR 7643)	Directeur de thèse
M. Steve Arscott Directeur de Recherche, Université Lille 1/CNRS (UMR 8520)	Co-Directeur de thèse
M. Fausto Sirotti Directeur de Recherche, Institut Polytechnique de Paris/CNRS (UMR 7643)	Invité

Thèse de doctorat

Acknowledgements

Working in LPMC as a Ph.D. candidate would be a precious experience in my life, but finishing the thesis means I have to put an ending to the story. Taking this opportunity, I thank all those who along with me during these three years.

First, I would like to express my sincere gratitude to Alistair Rowe, my supervisor, for providing this Ph.D. research subject to me, and also thanks for his continuous support. During these three years, he is always available, the countless time discussion with him let me know how to think like a researcher. And he is honest, he will let me know when I could do better. I will always be grateful for all of these.

Then I would like to mention Steve Arscott, my co-supervisor, without his support of well-designed and reliable silicon devices, I can bend nothing. On the other hand, I feel guilty to him, because I broke many of these silicon devices. I would specially thank my mentor Fausto Sirotti, who provides excellent guidance in the XPS experiment and in how to make a good presentation.

Additionally, I would thank Lucio Martinelli and Fabien Cadiz who gave me many help in the experiments, thank André Wack who provides a very nice and fancy sample holder, thank Abel Thayil for his excellent effort in simulation work, thank Prof. Jeffrey McCallum for many useful discussions. Most importantly, I want to thank all the members in the Lab, your kindness and help made me feel comfortable, so that I can quickly adapt to life in the lab.

Besides, I am grateful for my defense jury members: Prof. Alois Lugestein, Prof. Paul Hurley, Prof. Francois Rochet and Prof. Yvan Bonnassieux for their insightful comments and suggestion, and also for the questions which incented me to widen my research from various perspectives.

Finally, I would like to acknowledge my parents for giving me a loving home and the encouragement to chase my dreams, and my girlfriend Ruan for always being by my side and feeding me so well.

Thanks for all your encouragement!

Abstract

This thesis is a contribution to the study of giant, anomalous piezo-resistance in fully-depleted silicon micro- and nano-objects. Piezo-resistance in bulk silicon is a technologically important phenomenon in which mechanical stress changes the electrical resistivity via a change in the charge carrier effective masses. Nowadays, a wide range of commercial applications are based on silicon's piezo-resistance, such as strained-silicon CMOS, strain gauges, accelerometers, and all-electrical MEMS. As silicon device dimensions are reduced as described observationally by Moore's Law, it is of interest therefore to explore and understand the piezo-resistance of silicon micro- and nano-objects.

In this context giant piezo-resistance and piezo-resistance of anomalous sign have been reported in silicon nanowires and nano-membranes in recent years, but the physical origin of these effects remains unclear. In some cases, even the veracity of the claimed results has been questioned. Some basic elements of the claimed effects are agreed upon by the entire community, for example the fact that all claims of giant or anomalous piezo-resistance are made in surface depleted nanostructures i.e. where the surface depletion layer widths are larger than the smallest dimension of the sample. This places the nanostructures in the so-called space charge limit where assumptions of local charge neutrality are no longer valid, where electrical transport is no longer Ohmic, and where transport is described by so-called space charge limited currents (SCLC).

In this thesis the details of the stress-dependence of the non-equilibrium charge dynamics, in particular charge trapping and emission rates at fast electronic traps, during space charge limited transport in fully depleted silicon-on-insulator is probed using impedance spectroscopy. This, combined with an X-ray photo-electron spectroscopy study of statically deflected silicon cantilevers, strongly suggests that giant, non-steady-state piezo-resistance in the SCLC regime is due to stress-induced changes to hole trapping dynamics at intrinsic interface states. In contrast, under steady-state conditions like those used in all previous studies, giant piezo-resistance is not observed, even in the presence of interface traps. On the other hand, anomalous piezo-resistance is observed in the steady-state in defect (silicon divacancy) engineered SCLC devices, and this is shown to be the result of a voltage bias induced type change of the majority carrier.

In chapter 1, the history of piezo-resistance in semiconductors from its discovery in silicon in 1954 will be introduced. The giant and anomalous piezo-resistance, proposed physical models, and the controversy surrounding the experimental claims, are subsequently discussed.

Chapter 2 presents the physical description of piezo-resistance in bulk silicon when transport occurs in the neutral, quasi-equilibrium regime (Drude model). Far from equilibrium charge transport in the space charge limit is then introduced, including both the large-signal limit applicable to the steady-state response obtained using DC current measurements, and the small-signal limit applicable to the non-steady state response obtained using impedance spectroscopy.

Chapter 3 introduces the experimental details and the samples used throughout this work.

Chapter 4 contains the principal results obtained using impedance spectroscopy. A 25 *MPa* uniaxial mechanical stress applied parallel to the $\langle 110 \rangle$ crystal direction on a (001) fully-depleted silicon-on-isolator device and giant, anomalous piezo-resistance with a value of $-1100 \times 10^{-11}\ Pa^{-1}$ and a novel piezo-capacitance are observed under non-steady-state conditions. Comparison of data with the models introduced in Chapter 2 indicate that the devices operate in the SCLC regime in the presence of fast traps. By using a stress dependent form of these models it is argued that the giant, anomalous piezo-resistance results from the stress dependence of the charge capture (ω_c) and emission (ω_e) rates of fast traps. This results in large, stress-induced changes to the concentration of non-equilibrium charge carriers injected from the device contacts. In an effort to tentatively identify the fast traps responsible for the observations, the even symmetry of the piezo-response in stress is compared with the stress-dependence of the Fermi level pinning at oxidized silicon surfaces in the following chapter. The importance of these observations in clarifying the physical origin, and the veracity of previous reports of steady-state, giant piezo-resistance, is discussed.

Chapter 5 reports on the Raman spectroscopy and X-ray photo-electron spectroscopy (XPS) mapping experiments on statically deflected silicon cantilevers whose top surface is terminated by a native oxide. The comparison of Raman and XPS maps provides a spectroscopic measurement of the stress-dependence of the pinned surface Fermi level natively oxidized (001) silicon surfaces. A simplified analysis of the observed even symmetry of the stress-induced Fermi level shifts suggests that intrinsic interface defects (Pb_0) are likely responsible for the giant, anomalous piezo-response reported in the previous chapter.

Chapter 6 reports the DC applied bias dependence of the piezo-resistance in non-intentionally doped $n-$type silicon devices into which silicon divacancy defects have been engineered by self-implantation of Si+ ions. Using the formalism introduced in Chapter 2, the space charge limited characteristic of the devices exhibit three regimes; an Ohmic regime at low biases where conduction is dominated by equilibrium electrons, a modified Mott-Gurney regime at intermediate biases where conduction is space charge limited and dominated by holes injected from p^{++} contacts, and a plasma regime at high biases where conduction is space charge limited and non-negligible densities of both electrons and holes are present in the device. The measured piezo-resistance is shown to depend on the majority carrier type in each of these regimes; at low biases the usual $n-$type bulk, piezo-resistance is observed (i.e. the sign is negative); at intermediate biases the piezo-resistance switches to the bulk $p-$type (i.e. positive) piezo-resistance; in the plasma regime, the piezo-resistance is a combination of the bulk electron and hole values and has a net positive value that is slightly smaller than the usual bulk, piezo-resistance. As per the observation in chapter 4, no giant piezo-resistance is observed in the steady state. The results help shed light on observations of steady-state anomalous (i.e. sign reversed) piezo-resistance in depleted silicon nano-objects.

Finally, chapter 7 summarizes the conclusions and introduces possible future research directions.

Résumé

Cette thèse apporte une contribution à l'étude des effets géants et anormaux de piézo-résistance observés dans les micro- et nano-objets en silicium. La piézo-résistance du silicium massif est devenue, depuis les années 2000, la clé de voûte de nombreuses technologies dont le ≪strained silicon≫, les capteurs de contraintes, les accéléromètres et autres microsystèmes tout électriques. Comme l'industrie micro-électronique vise toujours des dispositifs de dimensions de plus en plus réduites, il est logique d'investiguer le comportement piézo-résistif du silicium à des échelles spatiales submicronique voire même nanométrique.

Dans ce contexte, depuis une dizaine d'années les nanofils et nano-membranes de silicium ont révélé l'existence d'une piézo-résistance géante et d'une piézo-résistance d'amplitude ≪normale≫ mais de signe anormal. Cependant l'origine de ces effets reste peu claire et dans certains cas, la véracité même des observations a été remise en cause. L'ensemble de ces effets semble corrélé à un appauvrissement en porteurs libres liés à la surface, ce qui place ces nano-objets dans la limite dite ≪charge d'espace≫, pour laquelle la neutralité électrique locale n'est plus assurée. Dans cette limite le transport électrique n'est plus ohmique; on parle alors de courants limités par la charge d'espace (en anglais ≪space charge limited current≫ ou SCLC) portés par des charges loin de l'équilibre.

Cette thèse met en lumière la dépendance en contrainte mécanique de la dynamique de charges hors équilibre, et plus spécifiquement la dépendance en contrainte des taux de capture et d'émission de porteurs libres sur des pièges liés aux défauts cristallins. Pour ce faire, nous utilisons la technique de spectroscopie d'impédance qui, alliée à la spectroscopie de photoémission, suggère très fortement que les pièges électro-mécaniquement actifs générant la piézo-résistance géante sont les pièges liés aux défauts intrinsèques de surface. La piézo-résistance géante n'est observée qu'en dehors du régime stationnaire. Dans le régime stationnaire, situation dans laquelle se situe l'ensemble des études précédentes, nous n'observons pas de piézo-résistance géante, même en présence des pièges. Par contre une piézo-résistance de signe anormal est mesurée en régime stationnaire dans le silicium dans lequel une densité de défauts bien choisis (des bi-lacunes de silicium) a été introduite. Nous démontrons que cette piézo-résistance anormale est due à un changement de type de porteur majoritaire induit par la tension appliquée en régime SCLC.

Le chapitre 1 aborde l'historique de la piézo-résistance en silicium depuis sa découverte en 1954 jusqu'aux observations controversées de la piézo-résistance géante et anomale dans les nano-objets en silicium.

Le chapitre 2 présente les modèles physiques de la piézo-résistance dans le silicium massif en régime de transport quasi-neutre (modèle de Drude). La théorie des SCLCs est ensuite introduite, à la fois en terme de grand signal, applicable à des mesures de piézo-résistance en régime stationnaire, et en terme de petit signal, applicable à des mesures effectuées hors du régime stationnaire avec l'analyseur d'impédance.

Le chapitre 3 présente les dispositifs expérimentaux, les procédures de mesure ainsi que les échantillons étudiés durant la thèse.

Le chapitre 4 contient les principaux résultats obtenus par la spectroscopie d'impédance. Une contrainte uniaxe de 25 MPa appliquée le long de la direction cristalline $\langle 110 \rangle$ d'un dispositif fabriqué sur du silicium-sur-isolant donne lieu à une piézo-résistance géante de $-1100 \times 10^{-11}\ Pa^{-1}$. Nous mettons aussi en évidence un nouvel effet de piézo-capacitance. Une comparaison des données avec la théorie introduite dans le chapitre 2 indique que les dispositifs opèrent dans la limite de charge d'espace en présence de pièges électroniques rapides. En prenant en compte la dépendance en contrainte dans ces modèles, nous démontrons que la piézo-résistance géante résulte de la dépendance en contrainte des taux de capture et d'émission de ces pièges rapides. Ceci donne lieu à des changements importants de densités de porteurs hors du régime stationnaire. Pour essayer d'identifier les pièges responsables de la piézo-réponse, la symétrie paire en contrainte de celle-ci est comparée dans le chapitre suivant à la symétrie en contrainte du ≪pinning≫ du niveau de Fermi à la surface. Ce chapitre se termine sur une discussion, revisitée à la lumière de nos résultats, des effets controversés de piézo-résistance géante publiés dans la littérature.

Le chapitre 5 traite la mesure de la dépendance en contrainte du ≪pinning≫ du niveau de Fermi de surface, réalisée en combinant cartographie Raman et photoémission rayons X sur des leviers en silicium statiquement fléchis. La surface (001) des micro-leviers est terminée par une couche d'oxyde native. Une contrainte uniaxe en tension, ou en compression, appliquée à la surface supérieure des leviers et parallèlement à la direction cristalline $\langle 110 \rangle$ induit un déplacement du niveau de Fermi de surface pair en contrainte. Ceci tend à montrer que la dynamique de piégeage sur les défauts intrinsèques de surface (type Pb_0) et sa dépendance en contrainte sont à l'origine des effets géants présentés dans le chapitre 4.

Le chapitre 6 aborde les mesures en régime stationnaire de piézo-résistance du silicium dans la limite de charge d'espace, pour laquelle une densité prédéterminée de bi-lacunes de silicium a été introduite par auto-implantation d'ions $Si+$. En utilisant le formalisme introduit dans le chapitre 2, la caractéristique courant-tension hors contrainte montre trois comportements différents: à basse tension une loi ohmique dominé par les électrons majoritaires; à des tensions intermédiaires une loi de Mott-Gurney modifiée selon laquelle les porteurs principaux de charge sont les trous hors équilibre injectés depuis les contacts p^{++}; à haute tension un régime plasma pour lequel un mélange de trous et d'électrons hors équilibre porte le courant. La piézo-résistance est déterminée par le porteur majoritaire. A basse tension un comportement du silicium type$-n$ est observé (i.e. de signe négatif) tandis qu'aux tensions intermédiaires une piézo-résistance similaire à celle du silicium type$-p$ est observée (i.e. de signe positive, et donc anomale par rapport aux électrons d'équilibre). A haute tension la piézo-résistance correspond à la somme des valeurs attendues pour le silicium type n et p, conséquence directe de la présence d'électrons et de trous dans le régime plasma.

Le chapitre 7, tout en résumant les conclusions principales de cette thèse développe également les directions futures à explorer.

Table of contents

List of figures

List of tables

Chapter 1

Introduction and Context

1.1 History of piezo-resistance in semiconductors

Since the first report of strain-induced changes to the resistance of iron and copper by William Thomson in 1856 [1], the effects of strain and strain direction on the conductivity of a variety of conductors, dubbed *piezo-resistance* (PZR) by Cookson in 1935 [2], have been widely investigated [3–9]. Base on these previous works, the tensor notation of mechanical stress applied on single crystal materials, as well as a generalized Hooke's Law, were used to better express the PZR effect [10, 11]. The expression of PZR in a crystalline solid is generally written as:

$$\pi_{ijkl} = \frac{\Delta 1}{\rho_{ij,0}} \frac{\partial \rho_{ij}}{\partial X_{kl}} \tag{1.1}$$

where tensor notation has been used. The stress, X, is written in tensor form, as is the resistivity ρ_{ij}, yielding a PZR π-coefficient, π_{ijkl}. Here, $\rho_{ij,0}$ is the zero-stress resistivity. In this thesis we will be concerned only by situation in which the mechanical stress is applied parallel to the direction of current flow in cubic crystals. In this case, a scalar longitudinal $\pi-$coefficient can be defined:

$$\pi_l = \frac{1}{\rho_0} \frac{\partial \rho}{\partial X}. \tag{1.2}$$

Moreover, the applied stresses used throughout correspond to strains of at most 10^{-3}. In this case geometric stress-induced changes to the resistance are negligible, and we may write:

$$\pi_l = \frac{1}{R_0} \frac{\partial R}{\partial X} \approx \frac{1}{X} \frac{\Delta R}{R_0}, \tag{1.3}$$

where ΔR is the stress-induced resistance change, and R_0 is the zero-stress resistance.

The PZR $\pi-$coefficient of a large number of metals is summarized according to Bridgman's effort [12, 13] and shown in Fig. 1.1. The measured PZR $\pi-$coefficients are represented as circles around the elements in the periodic table. The radius of these circles is proportional to the logarithm of the measured PZR $\pi-$coefficient. The obvious variation of circle radius along the rows and down the columns demonstrates that PZR is an electronic structure effect [14]. The details of how mechanical stress modifies silicon's electronic structure will be given in section 2.2.

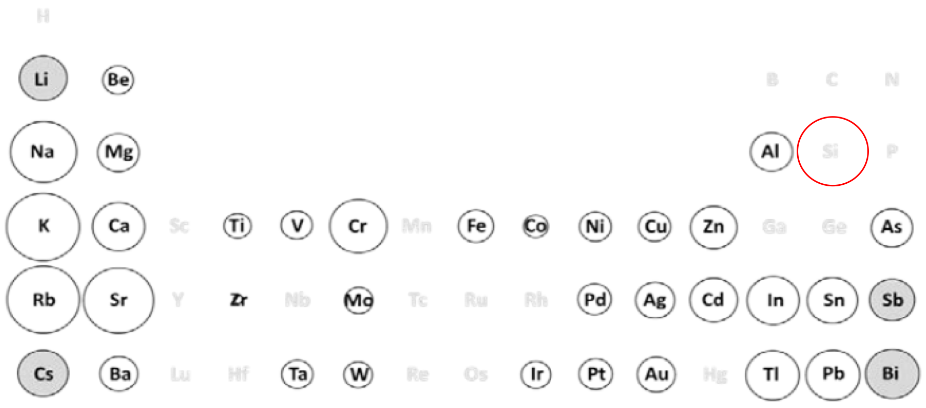

Fig. 1.1 The measured PZR $\pi-$coefficient of metals under hydrostatic pressure according to Bridgman's work [12, 13] are represented as circles around the elements in the periodic table. The radius of each circle corresponds to the logarithm of the measured PZR $\pi-$coefficient. Shaded circle (for example, Li) means the resistance increases with increasing pressure, i.e. the PZR $\pi-$coefficient is negative, while the white circles correspond to decreasing resistance with increasing pressure, i.e. the PZR $\pi-$coefficient is positive. The elements without circles means that these metals were not measured. Extracted from Ref. [14]

After more than 80 years of study the first application of PZR was the metallic strain gauge as proposed by Edward Simmons [15]. The single crystal semiconductors in general have higher PZR than metallic conductors [16], and have subsequently found applications as high sensitivity strain gauges. In 1954, the important experiment on PZR of silicon and germanium was reported by Smith [17], and a large PZR was reported. The longitudinal PZR $\pi-$coefficient, π_l, along the $\langle 110 \rangle$ crystal direction for $n-$ and $p-$type silicon are $-31 \times 10^{-11}\ Pa^{-1}$ and $71 \times 10^{-11}\ Pa^{-1}$ respectively [17]. The red circle in Fig. 1.1 corresponds to $\pi_l = 100 \times 10^{-11}\ Pa^{-1}$ for $n-$type silicon along the $\langle 100 \rangle$ direction and it can be seen that the PZR of bulk silicon is already large compared to most metallic elements. Kanda subsequently, graphically presented the angular variation of the PZR $\pi-$coefficients for $n-$ and $p-$type bulk silicon [18]. Since then, PZR in silicon has found many applications such as pressure, force and inertial sensors. Perhaps most importantly, stressed silicon is one of the key elements of the The International Technology Roadmap for Semiconductors (ITRS) [19]. A famous application of stressed silicon is shown in Fig. 1.2 as an example. Uniaxial compressive stress is applied along the $\langle 110\rangle$ crystal direction on a 45 *nm* $p-$type MOSFET by a $Si_{1-x}Ge_x$ deposition layer, whereas a uniaxial tensile stress is applied along $\langle 110\rangle$ crystal direction on $n-$type MOSFETs via deposition of a nitride-capping layer [20]. In both cases, the charge carrier mobilities are increased resulting in increases in the transconductance gain. The explanation for this increase in mobility can be found in section 2.2.

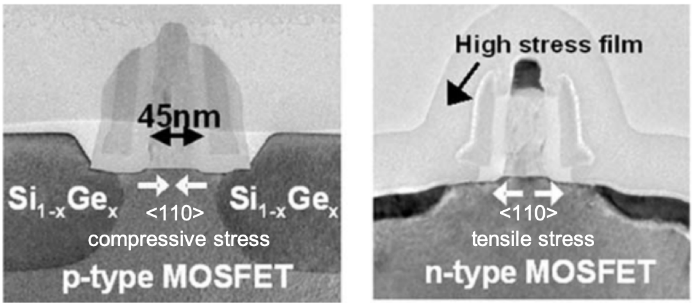

Fig. 1.2 TEM graphs of a 45 *nm* $p-$type and $n-$type silicon MOSFETs. The direction of arrows indicates that the compressive stress is applied on the $p-$type silicon MOSFET, while tensile stress is applied on the $n-$type silicon MOSFET. This results in increased electron and hole mobilities which improves the transistor performance. Extracted from Ref. [20]

1.2 Reports of giant piezo-resistance in nano-silicon

The order of magnitude of PZR $\pi-$coefficients in silicon has been shown in the previous section. However, a so-called giant piezo-resistance (GPZR) with much larger magnitude was reported in bottom-up grown, (110)-oriented, $p-$type silicon nanowires (SINWs) by He and Yang [21] in 2006,a variety of SINWs with variable diameters and resistivities were tested. Fig. 1.3(a) shows an example of used SINW. The current-voltage characteristics are measured under compressive and tensile stress shown as Fig. 1.3(b), which presents current increases under compressive stresses and decreases under tensile stresses. In the relative small scale of applied voltage, the current-voltage characteristics are linear. The non-linearity of $(\Delta\sigma/\sigma_0)$ versus X was observed, the slope of which is the PZR. According to the behaviour of $(\Delta\sigma/\sigma_0)$ in stress, the nonlinearities were classified into four categories: 'I' represents a relatively linear curve, 'C' represents a concave curve, 'L' is for curves with greater slope under compression, and a 'Z' curve is convex with compression and concave with tension. Compared to $p-$type bulk silicon PZR (shown as a linear dotted line in the Fig.

1.3(c)), the non-linearity is the first atypical point. The second point is the steep slope shown in Fig. 1.3(c) which corresponds to $\pi_l = 3550 \times 10^{-11}\ Pa^{-1}$, 50 times larger than the usual silicon PZR in this crystal direction [17]. This result attracted wide attention since it is the first experimental measurement of GPZR in SINWs. Indeed, prior works on SINWs didn't

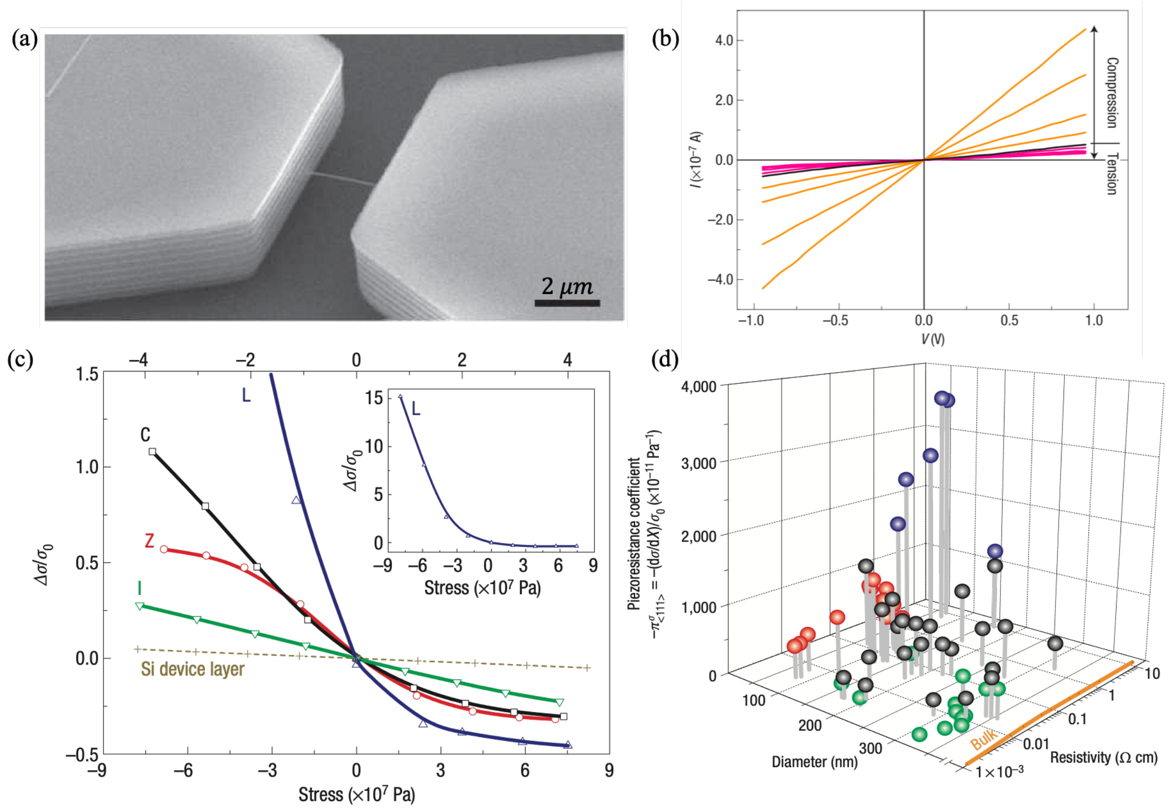

Fig. 1.3 The principle result of He and Yang's work [21]. (a) A p-type lateral SINW are shown between 2 Ohmic metallic contacts as example, the scale bar is 2 μm. (b) The current of a p-type SINW increases under compressive stresses and decreases under tensile stresses. (c) Relative variations in conductivity with applied stress, where Four types non-linear variations are observed and labelled with letters I, C, L and Z. Compared to the variation in $p-$type bulk silicon sample (dotted line), the slopes are much steeper. (d) The PZR plotted as a function of resistivity and diameter of SINWs. PZR up to 30-50 times larger than bulk effect in $p-$type silicon are reported in SINWs with high resistivities and small diameters. Extracted from Ref. [21]

show a giant effect. Polycrystalline nanowires [22] and top-down fabricated single crystal SINWs [23, 24] show a 50 % increase in PZR over the bulk effect but this was attributed to stress concentration effects. Much later, stress concentration effects were also shown to yield apparent GPZR [25]. (Apart from the first report of GPZR [21], the GPZR also reported by several other groups [26–29]. Interestingly, almost all GPZR were measured in samples with either or both high resistivity and small dimension.)

To explain the GPZR in SINWs, initial work focused on a physical description based on a quantum mechanical confinement effects [30–33]. According to these models GPZR appears when the minimum dimension of the sample (the diameter in the case of SINWs) is comparable to few nanometers. Indeed, unusual PZR has been observed in inversion layers at silicon surfaces [34]. However, in the recent experimental GPZR literature, minimum device dimensions are significantly larger than the quantum length scale. This significantly weakens arguments based on quantum confinement effect.

It is important to note that GPZR is always reported in silicon nanowires with small diameter and high resistivity, in other words, the GPZR was apparently observed only in carrier-depleted nanowires which are characterized by the diameter d being smaller than the depletion layer width W.

1.3 Proposed physical description of giant piezo-resistance (GPZR)

An oxidized silicon surface contains dangling bonds, surface defects, and disorder that leads to a distribution of localized surface states shown as short lines in Fig. 1.4. The density of these surface states is approximately the same order of magnitude as the density of surface atoms [35]. At such high densities, the surface Fermi level falls near a peak in the surface density of states labelled E_T, and one speaks of surface Fermi level pinning. In order to fill the surface states of energy lower than E_T charge in removed from the near surface Bloch band leading to band bending and a surface space charge layer (SCL) of width W shown in Fig. 1.4 for $p-$type material.

Imagine the initial contact between the surface and bulk. In order to attain equilibrium the Fermi levels of the surface and the bulk must align and this is achieved via a transfer of holes from the valence band to the surface states, leaving behind the negatively charged bulk acceptors. This space charge results in an internal electric field in the band bending region which opposes the transfer of holes to the surface. The transfer continuous until the internal electric field perfectly balances the transfer of holes via diffusion at which point the SCL has a W given by [36]:

$$W = \sqrt{\frac{2\varepsilon\psi_S}{qN_A}}. \tag{1.4}$$

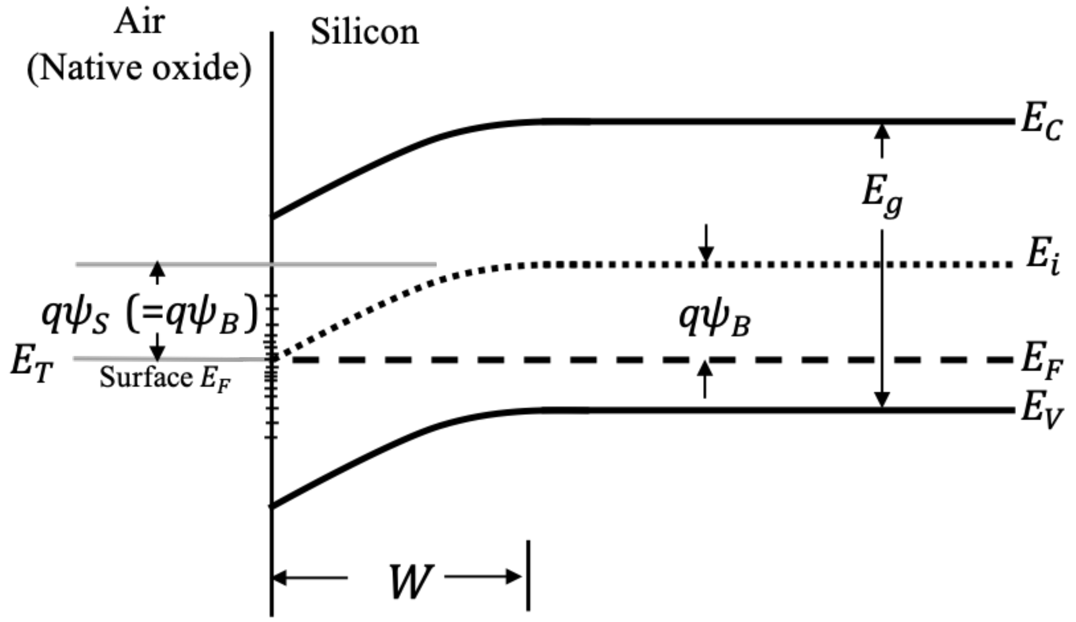

Fig. 1.4 $P-$type silicon energy band diagram. The surface bands downward bend due to surface states, the surface potential ψ_S is measured with respect to the intrinsic Fermi level E_i and is equivalent to zero in the bulk silicon. In case of high surface states density, the Fermi level is pinned at the mid of band gap.

Here ε is dielectric constant, N_A is acceptor concentration. The initial difference in Fermi levels at the surface and in the bulk appears as a surface potential ψ_S whose value is related to E_T as shown in Fig. 1.4. According to Boltzmann statistics the density of holes in the valence band at the surface is then [36]:

$$p_S = p_{p0} exp(-\frac{q\psi_S}{k_B T}), \tag{1.5}$$

where p_{p0} is the equilibrium density of holes in the $p-$type bulk silicon, k_B is Boltzmann's constant and T is absolute temperature in Kelvin.

Three regimes are shown in Fig. 1.5 according to the surface depletion layer width value. In the case of highly $p-$type doped bulk silicon resistor, since both resistor sides are exposed in the air, the native oxide layers are therefore formed on both sides. If the smallest dimension, d is much larger than the depletion layer width, W, as shown in Fig. 1.5(a). The energy bands in the gray regime do not bend, this regime is defined as the bulk channel, in this channel, the Fermi level is flat, dopant dominates the thermal equilibrium charge carriers, the free carriers in the surface depletion area are negligible. According to Eq. (1.4), the depletion layer width W can be increased by reducing the doping concentration until d is comparable to $2W$ as shown in Fig. 1.5(b) and the bulk channel no longer exists. Charge transport parallel to the surface then occurs in the SCL i.e. it is an SCLC. The energy band bending is still visible, however the bulk channel is *pinched-off* by surface potential [37]. When $W \gg d$, the energy bands are completely flat as shown in Fig. 1.5(c).

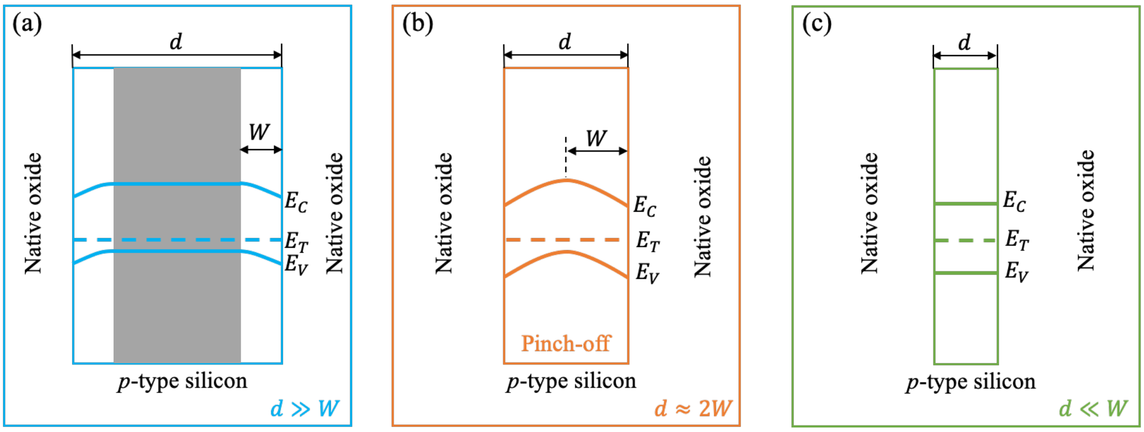

Fig. 1.5 A schematic energy band of *p*-type silicon. The ratio between depletion layer width W and smallest dimension of device d defines the limits of charge transport. In the case of $d \gg W$, the gray bulk channel short circuits the surface depletion areas, thermal dopant excitons dominates surface excitons. When $d \approx 2W$, the bulk channel is *pinched-off*, the thermal surface states excitons begin to dominate the free charge carriers. In the extreme condition $d \ll W$, the energy bands are flat, the dopants are negligible, this semiconductor device is more like insulator.

Since GPZR is only measured in silicon nanowires with the smallest diameters (d) and highest resistivities, according to the energy schema in Fig. 1.5(c), it was postulated that the GPZR is related to the stress dependence of the pinned surface Fermi level [37]. In this so-called *piezo-pinch* model, the surface Fermi energy varies linearly in stress resulting in exponential changes in the carrier density according to Eq. (1.5). This is fundamentally different from the usual bulk PZR which is due to the stress dependence of the mobility (see section 2.2). The piezo-pinch model seems to describe well the initial report of GPZR [21] and a variation of it was used to qualitatively describe the PZR of SINMs [29]. Moreover, the PZR of SINWs was shown to depend strongly on the surface crystal facets [26], further lending support to the notion that the stress dependence of the surface states is related to GPZR [27].

1.4 Absence of GPZR in Si nano-objects

This is not the end of the story as many other groups reported PZR similar to the bulk effect even in the space charge limited regime [23, 26, 28, 38–43]. It is unclear why such different

PZR behaviour has been measured in very similar nano-objects. Milne's work [38] offers a controversial explanation of this and posed the question: does GPZR really exist? As is well known, for a depleted sample ($d \ll W$), the measured current will drift with time independent of stress. The behaviour of the drift depends on the applied voltage or previously applied voltage due to dielectric relaxation of positive and negative charge traps at Si/SiO_2 interface or in the SiO_2 layer [38, 44, 45]. As shown in Fig. 1.6(a) two measured currents as a function of time with zero (red curve) and 13 MPa compressive (blue curve) stress applied using the stress modulation technique. At $t = 0$, the voltage $V_{ds} = 0.5\ V$ is applied on the a 200 $nm \times 2000\ nm \times 30\ \mu m$ depleted silicon nano-ribbon, the current drift can be seen due to surface traps dielectric relaxation. The current is expected to drop back to relative constant when all the traps are relaxed and for $t > 8000\ s$, the current is tentatively constant. But during the relaxation time, the current drift can be significantly larger than stress-induced current changes. However, the PZR measured by stress modulation technique can ignore the dielectric relaxation effect, allow us to measured only bulk PZR as shown in Fig. 1.6(b). This suggests that if the stress modulation technique is not used, separation of true PZR from current drift is difficult and may lead to a false identification of GPZR.

Other groups who used the stress modulation technique also observe bulk PZR, even in the space charge limit ($d \ll W$) [28, 46]. Another possible explanation for the GPZR is geometric stress concentration and McClarty [25] reported PZR of giant magnitude in top-down fabricated SINWs due to this. Putting this possibility aside, to date nobody has claimed GPZR when using the stress modulation technique.

1.5 Anomalous piezo-resistance

Apart from GPZR, an anomalous piezo-resistance (APZR), i.e. of opposite sign but similar magnitude to bulk PZR, has been observed by many groups as well.

Lugstein et al. measured PZR of a set of intrinsic $p-$type vapor-liquid-solid (VLS) grown silicon nanowires by applying various uniaxial tensile stresses, from low to ultra-high stress [46]. While positive bulk-like PZR was observed at low-level stress, APZR was observed at ultra-high stress as shown in Fig. 1.7(a). Jang et al. reported APZR in highly doped $p-$type ($\sim 10^{17}\ cm^{-3}$) silicon nano-membranes (SINMs) with varying thickness from 15 nm to 100 nm [47]. The principal result is shown in Fig. 1.7(b) in which the relative change in resistance of SINMs as a function of time with various thicknesses of samples is shown. The green zone means the 0.3 % tensile strain is applied on the SINMs, while the white zone is a stress-free period. It is seen that the bulk-like PZR is observed in the thickest SINMs but that it decreases as thickness decreases, eventually changing sign in the thinnest SINMs.

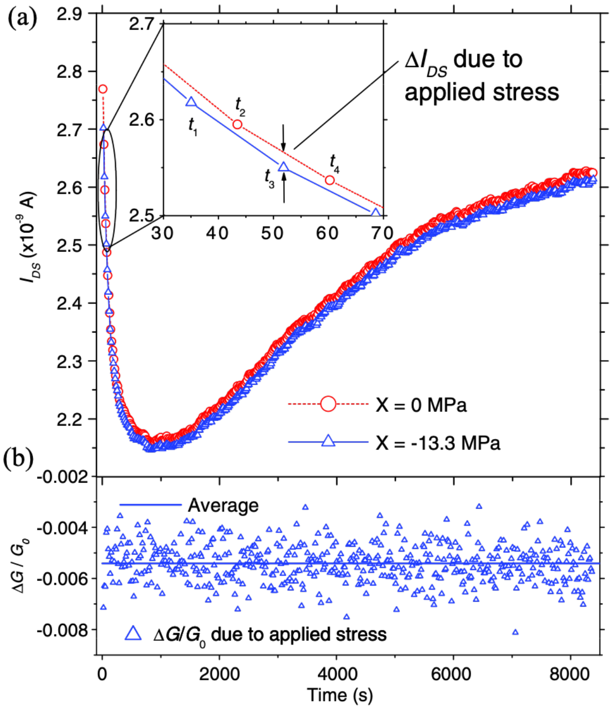

Fig. 1.6 (a) Current of a $n-$type nano-ribbon with 0 MPa and 13 MPa compressive stress respectively. The dielectric relaxation of traps induced current drift will significantly affect the measurement of PZR. The inset indicates the sequence of measurements used in the stress modulation technique. (b) Relative conductance change measured by stress modulation technique, which is only due to stress. Extracted from Ref. [38]

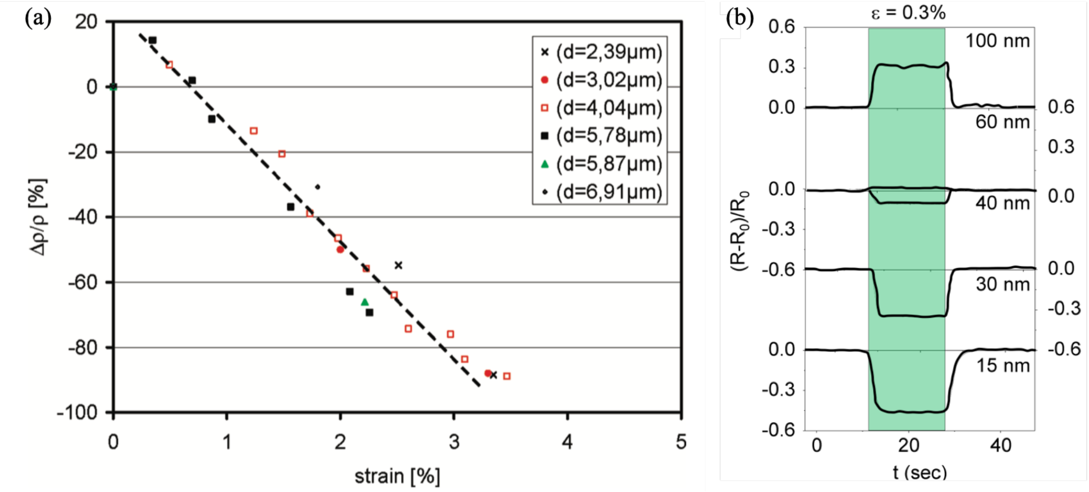

Fig. 1.7 (a) Relative changes in resistivity as function of strain of SINWs with 100 nm diameter. The symbols correspond to different SINW lengths. Extracted from Ref. [46]. (b) Relative changes in resistance versus time for different thickness of SINMs. Extracted from Ref. [47]

Table 1.1 Observed PZR in SINMs with variable thickness [47].

Thickness (nm)	$\pi/10^{-11}$ (Pa^{-1})	Depleted
100	+60	No
60	+5	No
40	-20	Yes
30	-80	Yes
15	-114	Yes

The results are summarised in Table 1.1. For the SINMs with 100 nm thickness the PZR $\pi-$coefficient is about 60×10^{-11} Pa^{-1}, whereas it changes sign at a thickness of 40 nm, and is equal to -114×10^{-11} Pa^{-1} at a thickness of 15 nm.

The stress modulation technique [38] is used in these experiments [46, 47] in order to separate resistance drift due to dielectric relaxation. Therefore the measured PZR is reliable. The APZR is likely linked to the surface states [29, 48], since the APZR is always observed in the large surface-to-volume ratio of silicon nano-objects, almost all of these devices are depleted. Lugstein realized this phenomenon and use the chemical technique to deposit the different cover layer on the surface of $p-$type SINWs to modify the nature of surface states. SINWs with as grown native oxide and Al_2O_3 deposition present $p-$type conduction, then positive, similar to $p-$type bulk-like PZR has been measured. SINWs with SiO_2 coated deposition presents $n-$type conduction, thus a negative PZR is obtained, it consists with the $n-$type bulk-like PZR. So that, the APZR might be non-existent, it only depends on the conduction of SINWs sample [48]. In other words, surface states play a dominant role in the electrical properties, further in PZR for the depleted samples.

1.6 Conclusion

From the discussion above, the current state-of-the-art in nano-silicon PZR becomes clearer. In experiments where the stress modulation technique is used to separate resistance drift from true PZR, only anomalous PZR is measured and reported. Reports of GPZR may be the result of resistance drift due to dielectric relaxation, or perhaps simply the result of stress concentration. The existence of a true GPZR is still unclear.

Recent reports of PZR in $p-$type silicon nano-objects are arranged in order of published year and shown in Fig. 1.8. Depleted nano-objects are presented as red dots, whereas charge neutral objects are shown as black dots. The measured values of PZR are separated into three regions: GPZR (top blue region), bulk-like PZR (middle gray region) and APZR (bottom yellow region). All reports of giant or anomalous PZR, are made in nano-objects with the smallest dimensions and the highest resistivities i.e. in the space charge limited. For more heavily doped samples where $W \ll d$, the measured PZR is bulk-like. Therefore, the

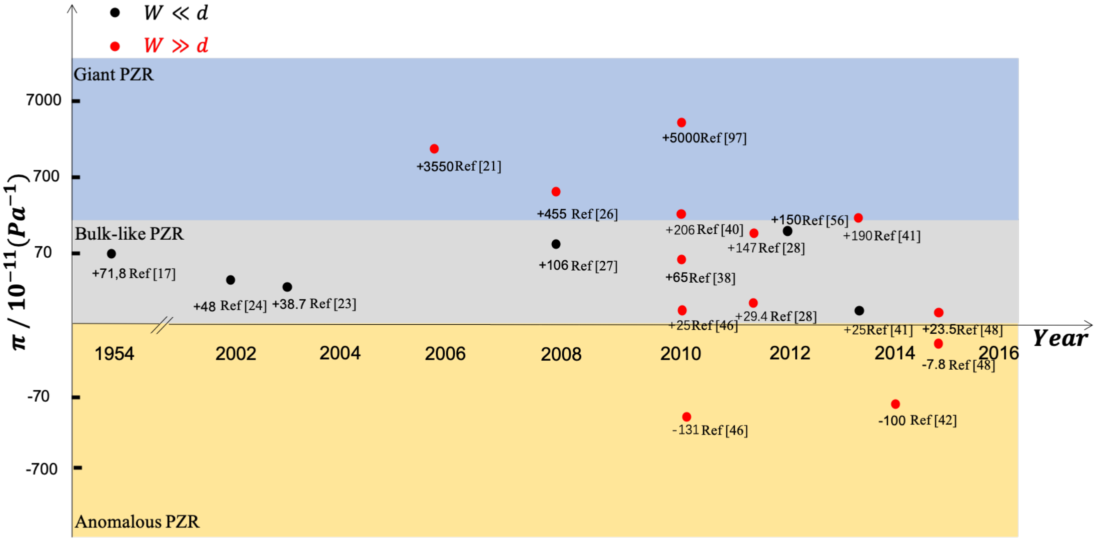

Fig. 1.8 Time line of mainly reported giant, anomalous PZR in $p-$type silicon nano-objects. Depleted nano-objects are presented by red dots, otherwise presented by black dots.

depletion layer width is the keyword for observing the giant and anomalous PZR in silicon nano-objects, the structure and current-voltage characteristic of devices are shown in Table. 1.2. The symbol '-' presents the missing information from the literature. Since many groups use semiconductor parameter analyzer to sweep DC voltage applied on the device in order to obtain current-voltage characteristic, the PZR measured by this method are labelled as 'voltage swept'. For depleted silicon nano-objects, the resistance is always very high, and although the electrodes are Ohmic contacts, the measured current-voltage characteristic is non-linear [25, 46, 48, 49]. This is symptomatic of the so-called space-charge-limited current (SCLC) regime. In this limit the current is principally carried by a significant density of non-equilibrium charge carriers injected into silicon nano-objects from the contacts. For applied DC voltages in the SCLC limit, the current is proportional to the square of the voltage (see section 2.3). For all the reports of PZR in the literature mentioned above, this DC measurement method is used. Nobody has previously attempted PZR measurements in the small-signal limit in the SCLC regime. However, as is well-known, the impedance of SCLC samples is frequency dependent (see section 2.3), so that the PZR may possibly depend on the frequency as well. Giant or anomalous PZR may be dependent on the frequency of the applied AC voltage, and it is important and novel contribution to explore the frequency dependence of the giant and anomalous PZR effect (see Chapter 4).

Table 1.2 Summary of longitudinal $\pi-$coefficient in bulk and nanostructured silicon.

Ref.	PZR type	Depleted	Structure	I-V response
[21]	Giant	Yes	Lateral nanowires	Linear
[23]	Bulk	No	Lateral nanowires	Linear
[24]	Bulk	No	Lateral nanowires	Linear
[26]	Giant	Yes	Lateral nanowires	- (voltage swept)
[27]	Bulk	No	Lateral nanowires	- (voltage swept)
[28]	Bulk	Yes	Lateral nanowires	Linear (voltage swept)
[38]	Bulk	Yes	Lateral nanowires	Linear (voltage swept)
[50]	Giant	Yes	Lateral nanowires	-
[41]	Bulk	No	Lateral nanowires	Linear
[41]	Giant	Yes	Lateral nanowires	-
[47]	Anomalous	Yes	Nanomembranes	-
[46]	Anomalous	Yes	Lateral nanowires	Nonlinear
[48]	Anomalous	Yes	Lateral nanowires	Nonlinear
[49]	Giant	Yes	Lateral nanowires	Nonlinear
[51]	Bulk	No	Bulk silicon	Linear

1.7 Objectives of this thesis

Exploring and understanding the existence and origin of giant and anomalous PZR in nano-silicon is the main objective of this thesis. To do this, impedance spectroscopy will be used as an entirely new experimental approach to the problem. Unlike the DC current-voltage techniques used previously by all groups including our own, this method potentially gives access to the characteristic physical time scale associated with space charge limited transport. It will be seen that this characteristic time corresponds to the charge trapping and emission rates as fast electronic traps associated with intrinsic interface defects (see Chapters 4 and 5). It will be shown explicitly that stress-induced modifications to these trapping and emission times can result in both giant and anomalous PZR under certain conditions (see Chapter 4). The first attempts at deliberately introducing volume defects into silicon will be shown to yield APZR under DC conditions, and it will be demonstrated that this is due to a charge carrier type change induced by the applied DC voltage in the SCLC limit.

Chapter 2

Background theory

In this chapter, the basic idea and fundamental concepts of silicon PZR are established, in particular how mechanical stress changes the electronic structure of bulk silicon. In section 2.1, the theoretical relations between stress, resistivity, and resistance are discussed. The expressions for and the experimental values of the bulk longitudinal and transverse π-coefficients are introduced. In section 2.2, the physical understanding of $n-$type and $p-$type bulk PZR are established, and are shown to be principally due to stress-induced changes in the effective mass of charge carriers. In section 2.3, space charge limited current (SCLC) transport in semiconductor is introduced and an approximate analytical model for the steady-state and non-steady-state impedance are given. The effect of fast charge traps on the impedance is then discussed. In section 2.4, the voltage dependence of the trap emission rates due to Poole-Frenkel like effects is introduced. These concepts are important for the interpretation of the data presented in Chapter 4 and 6.

2.1 Effect of mechanical stress on electronic structure

The strain, ε_{long}, refers to the relative deformation of a material parallel to the applied mechanical stress, $\varepsilon_{long} = \Delta l/l$, where Δl is the stress-induced length change, and l is the zero-stress length. Poisson's effect dictates that a change in the dimensions along the transverse direction, ε_{trans} according to: $\nu = -d\varepsilon_{trans}/d\varepsilon_{long}$. Here ν is Poisson's ratio. According to the definition of the resistance (R) are of a rectangular parallel-piped material,

$$R = \frac{\rho l}{A}, \tag{2.1}$$

where ρ is the resistivity and A is the cross-sectional area of the material. The mechanically stressed resistance can be written $R' = \rho l(1+\varepsilon_{long})/(A(1-\nu\varepsilon_{long})^2)$, so that the relative resistance change due solely to stress-induced geometry changes is:

$$\frac{R'-R}{R}=\frac{\frac{(1+\varepsilon_{long})}{(1-\nu\varepsilon_{long})^2}-1}{1}\approx\varepsilon_{long}(1+2\nu)\tag{2.2}$$

for the case of $\varepsilon_{long}\ll 1$. For volume conservation ν equals 0.5 so $(R'-R)/R=2\varepsilon_{long}$. In addition to geometry changes, mechanical stress can also modify the material's resistivity. This phenomenan is known as **PIEZO-RESISTIVITY**. In this case, Eq. (2.2) must be re-written:

$$\frac{R'-R}{R}=\frac{\Delta R}{R}=\varepsilon_{long}(1+2\nu)+\frac{\Delta\rho}{\rho}.\tag{2.3}$$

The geometry and resistivity induced changes in resistance are presented as the first and second terms in Eq. (2.3) respectively. For silicon, since the first term is generally much smaller than second the term, the first term is usually ignored (see section 2.2). The piezoresistivity is independent of geometric structure and can be described by a π-coefficient already given in Eq. (1.1):

$$\frac{\Delta\rho}{\rho_0}=\pi X.\tag{2.4}$$

In the case of small relative changes in ρ, $\Delta\rho/\rho\ll 1$, $\Delta\rho/\rho_0$ can be expressed as $\Delta\rho/\rho_0\approx -\Delta\sigma/\sigma_0=\pi X$, where $\sigma=1/\rho$ is the electrical conductivity and X is the mechanical stress.

In general ρ and X are second order tensors, while π is a fourth order tensor. Using Einstein's notation, Eq. (2.4) becomes:

$$\frac{\Delta\rho_{ij}}{\rho_0}\approx-\frac{\Delta\sigma_{ij}}{\sigma_0}=\pi_{ijkl}X_{kl},\tag{2.5}$$

The indices (i,j,k,l) vary from 1 to 3, hence ρ_{ij} and X_{kl} contain 3^2=9 independent components, while π_{ijkl} contains 3^4=81 independent components. Onsager's relations for the resistivity and stress tensors dictate however that $\pi_{ijkl}=\pi_{jikl}$, so the number of independent components can be reduced to 45. The six-vector notation is often applied in Eq. (2.5), which becomes:

$$\frac{\Delta\rho_m}{\rho_0}\approx-\frac{\Delta\sigma_m}{\sigma_0}=\pi_{mn}X_n.\tag{2.6}$$

The indices (m,n) vary from 1 to 6, and the piezo-resistivity tensor is further reduced to 36 independent components. For the cubic symmetry of silicon (face-centered cubic unit cell), there are only 3 non-zero independent components (π_{11}, π_{12} and π_{44}) in the piezoresistivity

Table 2.1 π-coefficients in bulk $p-$type and $n-$type silicon at room temperature [17].

Type	π_{11}	π_{12}	π_{44}
	$10^{-11}\ Pa^{-1}$	$10^{-11}\ Pa^{-1}$	$10^{-11}\ Pa^{-1}$
n	-102.2	+53.4	-13.6
p	+6.6	-1.1	+138.1

tensor [52], so that the $\pi-$coefficient tensor becomes:

$$\pi = \begin{bmatrix} \pi_{11} & \pi_{12} & \pi_{12} & 0 & 0 & 0 \\ \pi_{12} & \pi_{11} & \pi_{12} & 0 & 0 & 0 \\ \pi_{12} & \pi_{12} & \pi_{11} & 0 & 0 & 0 \\ 0 & 0 & 0 & \pi_{44} & 0 & 0 \\ 0 & 0 & 0 & 0 & \pi_{44} & 0 \\ 0 & 0 & 0 & 0 & 0 & \pi_{44} \end{bmatrix}. \tag{2.7}$$

Among the piezo-resistivity coefficients, π_{11} describes the piezoresistive effect along one principal crystal axis for stress along this principal crystal axis (longitudinal piezoresistive effect), π_{12} describes the piezoresistive effect along one principal crystal axis for stress directed along one of the other perpendicular crystal axes (transverse piezoresistive effect), and π_{44} describes the piezoresistive effect induced by in-plane shear stress. The value of the π-coefficient components depends on whether one is considering the conduction or the valence band i.e. on whether one is considering $n-$type or $p-$type material [18]. According to Smith's pioneering experimental work on silicon PZR [17], the value of the π-coefficients are given in Table 2.1. The physical origin of this non-zero value of the $\pi-$coefficient will be given in the section 2.2.

Resistivity tensor

The piezo-resistivity effect and its tensor in silicon is discussed above. To correctly measure the π-coefficients of silicon we need to consider the direction of the applied electrical field $\vec{E}$ and the current density $\vec{J}$. According to Ohm's law, $\vec{E} = \rho\vec{J}$, where $\vec{E}$ and $\vec{J}$ are vectors. In the matrix form, Ohm's law is:

$$\begin{bmatrix} E_x \\ E_y \\ E_z \end{bmatrix} = \begin{bmatrix} \rho_{xx} & \rho_{xy} & \rho_{xz} \\ \rho_{yx} & \rho_{yy} & \rho_{yz} \\ \rho_{zx} & \rho_{zy} & \rho_{zz} \end{bmatrix} \begin{bmatrix} J_x \\ J_y \\ J_z \end{bmatrix}. \tag{2.8}$$

Note that Eq. (2.8) is valid only for the quasi-equilibrium transport case where charge neutrality holds (Drude's limit). In the space charge limit to be considered later in this thesis, when injected charge carriers appear densities much greater than the equilibrium values and the current-voltage characteristic, is no longer linear. In this case, Eq. (2.8) is no longer valid. Nevertheless, here we focus on Ohm's law in order to better understand the expressions for the bulk PZR. According to Onsager's theorem [53], the resistivity tensor is symmetric, i.e. $\rho_{ij} = \rho_{ji}$. By using the notation $\rho_1 = \rho_{xx}$, $\rho_2 = \rho_{yy}$, $\rho_3 = \rho_{zz}$, $\rho_4 = \rho_{yz}$, $\rho_5 = \rho_{zx}$ and $\rho_6 = \rho_{xy}$, the resistivity tensor becomes:

$$\rho = \begin{bmatrix} \rho_1 & \rho_6 & \rho_5 \\ \rho_6 & \rho_2 & \rho_4 \\ \rho_5 & \rho_4 & \rho_3 \end{bmatrix}. \tag{2.9}$$

It can be shown [54] that the cubic symmetry of silicon imposes for the constraints on the elements of this tensor, in particular that $\rho_1 = \rho_2 = \rho_3 = \rho_0$ and $\rho_4 = \rho_5 = \rho_6 = 0$. Thus,

$$\begin{bmatrix} E_x \\ E_y \\ E_z \end{bmatrix} = \begin{bmatrix} \rho_0 & 0 & 0 \\ 0 & \rho_0 & 0 \\ 0 & 0 & \rho_0 \end{bmatrix} \begin{bmatrix} J_x \\ J_y \\ J_z \end{bmatrix}. \tag{2.10}$$

Here ρ_0 will denote the zero-stress resistivity. Once the crystal is deformed by a stress, its symmetry is changed and Eq. (2.10) is no longer valid. The relationship between $\vec{E}$ and $\vec{J}$ needs to be redefined. By using Eq. (2.7), the resistivity after stress is applied on the silicon:

$$\begin{bmatrix} \rho_1 \\ \rho_2 \\ \rho_3 \\ \rho_4 \\ \rho_5 \\ \rho_6 \end{bmatrix} = \begin{bmatrix} \rho_0 \\ \rho_0 \\ \rho_0 \\ 0 \\ 0 \\ 0 \end{bmatrix} + \rho_0 \begin{bmatrix} \pi_{11} & \pi_{12} & \pi_{12} & 0 & 0 & 0 \\ \pi_{12} & \pi_{11} & \pi_{12} & 0 & 0 & 0 \\ \pi_{12} & \pi_{12} & \pi_{11} & 0 & 0 & 0 \\ 0 & 0 & 0 & \pi_{44} & 0 & 0 \\ 0 & 0 & 0 & 0 & \pi_{44} & 0 \\ 0 & 0 & 0 & 0 & 0 & \pi_{44} \end{bmatrix} \begin{bmatrix} X_1 \\ X_2 \\ X_3 \\ X_4 \\ X_5 \\ X_6 \end{bmatrix} \tag{2.11}$$

where $X_1 = X_{xx}$, $X_2 = X_{yy}$, $X_3 = X_{zz}$, $X_4 = X_{yz}$, $X_5 = X_{zx}$ and $X_6 = X_{xy}$. For example, in the six-element notation, a stress with magnitude of X_0 applied parallel to $\langle 110 \rangle$ crystal direction is:

$$X = \begin{bmatrix} X_0/2 \\ X_0/2 \\ 0 \\ X_0/2 \\ 0 \\ 0 \end{bmatrix}. \tag{2.12}$$

This crystal direction is the most relevant for this thesis, and expressions for the longitudinal and transverse PZR will be discussed along in this $\langle 110 \rangle$ direction. To further understand how stress direction will influence PZR rotations of the coordinate system will be discussed.

Rotations of the coordinate system

The Cartesian coordinate system O-XYZ shown in Fig. 2.1 [55] may be rotated to a new coordinate system O-$X'Y'Z'$ as shown. The relationship between O-XYZ and O-$X'Y'Z'$ can be described by three rotation angles (θ, ϕ and ψ) which are known as Euler's angles. The

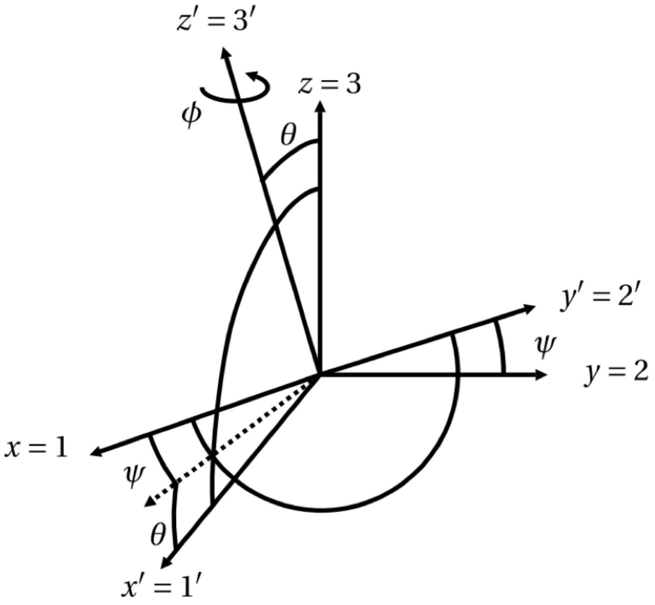

Fig. 2.1 Coordinate rotation angles used to determine for different crystal directions. Extracted from [55]

relationship between the two coordinate systems O-XYZ and O-$X'Y'Z'$ is described by three independent matrices A, B and C, which correspond to the three rotation operations:

$$A=\begin{bmatrix} sin\phi & -cos\phi & 0 \\ cos\phi & sin\phi & 0 \\ 0 & 0 & 1 \end{bmatrix} B=\begin{bmatrix} 1 & 0 & 0 \\ 0 & cos\theta & sin\theta \\ 0 & -sin\theta & cos\theta \end{bmatrix} C=\begin{bmatrix} -sin\psi & cos\psi & 0 \\ -cos\psi & -sin\psi & 0 \\ 0 & 0 & 1 \end{bmatrix} \qquad (2.13)$$

The product of the matrices A, B and C is the general rotation matrix, i.e., the transformation matrix M:

$$\begin{aligned} M &= ABC \\ &= \begin{bmatrix} \cos\psi\cos\theta\cos\phi-\sin\psi\sin\phi & \cos\psi\cos\theta\sin\phi+\sin\psi\cos\phi & -\cos\psi\sin\phi \\ -\sin\psi\cos\theta\cos\phi-\cos\psi\sin\phi & -\sin\psi\cos\theta\sin\phi+\cos\psi\cos\phi & \sin\psi\sin\phi \\ \sin\theta\cos\phi & \sin\theta\sin\phi & \cos\theta \end{bmatrix}, \end{aligned} \qquad (2.14)$$

so that the relationship between two coordinate systems O-XYZ and O-$X'Y'Z'$ can be expressed by operating with the transformation matrix:

$$\begin{bmatrix} x' \\ y' \\ z' \end{bmatrix} = M \begin{bmatrix} x \\ y \\ z \end{bmatrix} = \begin{bmatrix} l_1 & m_1 & n_1 \\ l_2 & m_2 & n_2 \\ l_3 & m_3 & n_3 \end{bmatrix} \begin{bmatrix} x \\ y \\ z \end{bmatrix}, \qquad (2.15)$$

where l_i, m_i and n_i, $i \in \{1,2,3\}$ are the direction cosines. In the O-$X'Y'Z'$ coordinate system, the relationship between electric field and current density can be expressed as:

$$E' = \rho' J'. \qquad (2.16)$$

Using the transformation matrix in Eq. (2.16), we have:

$$E = \rho J = M^{-1}\rho' M J. \qquad (2.17)$$

Then the expression ρ' = Mρ M^{-1} could be obtained from Eq. (2.17). Further developing this equation, the transformation matrix between ρ' and ρ in 6-vector notation can be written here:

$$\begin{bmatrix} \rho_1' \\ \rho_2' \\ \rho_3' \\ \rho_4' \\ \rho_5' \\ \rho_6' \end{bmatrix} = \begin{bmatrix} l_1^2 & m_1^2 & n_1^2 & 2m_1n_1 & 2n_1l_1 & 2l_1m_1 \\ l_2^2 & m_2^2 & n_2^2 & 2m_2n_2 & 2n_2l_2 & 2l_2m_2 \\ l_3^2 & m_3^2 & n_3^2 & 2m_3n_3 & 2n_3l_3 & 2l_3m_3 \\ l_2l_3 & m_2m_3 & n_2m_3 & m_2n_3+m_3n_2 & n_2l_3+n_3l_2 & m_2l_3+m_3l_2 \\ l_3l_1 & m_3m_1 & n_3m_1 & m_3n_1+m_1n_3 & n_3l_1+n_1l_3 & m_3l_1+m_1l_3 \\ l_1l_2 & m_1m_2 & n_1m_2 & m_1n_2+m_2n_1 & n_1l_2+n_2l_1 & m_1l_2+m_2l_1 \end{bmatrix} \begin{bmatrix} \rho_1 \\ \rho_2 \\ \rho_3 \\ \rho_4 \\ \rho_5 \\ \rho_6 \end{bmatrix} = \alpha \begin{bmatrix} \rho_1 \\ \rho_2 \\ \rho_3 \\ \rho_4 \\ \rho_5 \\ \rho_6 \end{bmatrix} \tag{2.18}$$

The simplified notation for Eq. (2.18) is $\rho' = \alpha\ \rho$, α is the transformation matrix shown in the last formula. The coordinate transformation relationship can also be used in stress and piezo-resistance tensor, like $X' = \alpha X$ and $(\rho/\rho_0)' = \alpha\ \rho/\rho_0$.

Similar to the process used in Eq. (2.17), the relationship between π' and π can be extracted and shown to be:

$$\pi' = \alpha\pi\alpha^{-1}. \tag{2.19}$$

According to Eq. (2.19), the components of π' can be written by the relation:

$$\pi_{ij} = \sum_{k,l=1}^{6} \alpha_{ik}\pi_{kl}\alpha_{lj}^{-1}. \tag{2.20}$$

Using Eq. (2.20), for example, the rotated $\pi-$coefficient π_{11}' and can be written as:

$$\pi_{11}' = \sum_{k,l=1}^{6} \alpha_{1k}\pi_{kl}\alpha_{l1}^{-1}, \tag{2.21}$$

where $\pi_{k,l}$ is the piezo-resistance coefficient tensor shown as Eq. (2.7). Since $\pi_{k,l}$ has 12 non-zero components which composed of 3 independent components, π_{11}, π_{12} and π_{44}, the rotated $\pi-$coefficient π_{11}' can be simplified as:

$$\begin{aligned} \pi_{11}' = {} & \pi_{11}(\alpha_{11}\alpha_{11}^{-1} + \alpha_{12}\alpha_{21}^{-1} + \alpha_{13}\alpha_{31}^{-1}) \\ & + \pi_{12}(\alpha_{11}\alpha_{21}^{-1} + \alpha_{12}\alpha_{31}^{-1} + \alpha_{12}\alpha_{11}^{-1} + \alpha_{12}\alpha_{31}^{-1} + \alpha_{13}\alpha_{11}^{-1} + \alpha_{13}\alpha_{21}^{-1}) \\ & + \pi_{44}(\alpha_{14}\alpha_{41}^{-1} + \alpha_{15}\alpha_{51}^{-1} + \alpha_{16}\alpha_{61}^{-1}) \end{aligned} \tag{2.22}$$

The components of α are shown in Eq. (2.18), similarly the components of $\alpha's$ transposed matrix α^{-1} are also easy to obtain. Since that, we have:

$$\begin{aligned}\pi'_{11} &= \pi_{11}(l_1^2 l_1^2 + m_1^2 m_1^2 + n_1^2 n_1^2) \\ &+ \pi_{12}(l_1^2(m_1^2+n_1^2) + m_1^2(l_1^2+n_1^2) + n_1^2(l_1^2+m_1^2)) \\ &+ \pi_{44}(2m_1^2 n_1^2 + 2n_1^2 l_1^2 + 2l_1^2 m_1^2) \qquad (2.23)\end{aligned}$$

By using the relationship for the direction cosines, $l_i^2 + m_i^2 + n_i^2 = 1 (i = 1,2,3)$ and $l_i l_j + m_i m_j + n_i n_j = 0 (i \neq j)$, the π'_{11}, i.e. the longitudinal $\pi-$coefficient can be expressed as:

$$\pi_L = \pi'_{11} = \pi_{11} - 2(\pi_{11} - \pi_{12} - \pi_{44})(l_1^2 m_1^2 + m_1^2 n_1^2 + l_1^2 n_1^2) \qquad (2.24)$$

Similarly, transverse π-coefficient π_T are able to be expressed as [17, 18]:

$$\pi_T = \pi'_{12} = \pi_{12} + 2(\pi_{11} - \pi_{12} - \pi_{44})(l_1^2 l_1^2 + m_1^2 m_1^2 + n_1^2 n_1^2) \qquad (2.25)$$

In this thesis we will principally be interested in $p-$type silicon in which current flows parallels to the applied stress along the $\langle 110 \rangle$ crystal direction. This is the configuration used in much of the PZR literature concerning nano-silicon, and it also the technologically important direction for $p-$channel strained silicon device (see section 1.1). When stress is applied in the $\langle 110 \rangle$ crystal direction on a (001) silicon wafer, there is no rotation of x and y, i.e. θ and ψ in Fig. 2.1 are zero. The only rotation is around the $z-$axis by an angle ϕ as shown in Fig. 2.1. The transformation matrix M can therefore be written:

$$M = \begin{bmatrix} l_1 & m_1 & n_1 \\ l_2 & m_2 & n_2 \\ l_3 & m_3 & n_3 \end{bmatrix} = \begin{bmatrix} cos\phi & sin\phi & 0 \\ -sin\phi & cos\phi & 0 \\ 0 & 0 & 1 \end{bmatrix} = \begin{bmatrix} \frac{1}{\sqrt{2}} & \frac{1}{\sqrt{2}} & 0 \\ -\frac{1}{\sqrt{2}} & \frac{1}{\sqrt{2}} & 0 \\ 0 & 0 & 1 \end{bmatrix}, \qquad (2.26)$$

where $\phi = \frac{\pi}{4}$ is the angle between the [100] principle axes and the $\langle 110 \rangle$ direction. Therefore from Eqs. (2.24) and (2.25) the longitudinal coefficient π_L and transverse coefficient π_T in the $\langle 110 \rangle$ direction are:

$$\pi_L = \frac{1}{2}(\pi_{11} + \pi_{12} + \pi_{44}) \qquad (2.27)$$

and

$$\pi_T = \frac{1}{2}(\pi_{11} + \pi_{12} - \pi_{44}). \qquad (2.28)$$

Table 2.2 The longitudinal piezoresistive π_L and transverse piezoresistive π_T in bulk $p-$type and $n-$type bulk (001) silicon under $\langle 110\rangle$ direction stress at room temperature [17].

Type	π_L	π_T
	$10^{-11}\ Pa^{-1}$	$10^{-11}\ Pa^{-1}$
n	-31.2	-17.6
p	+71.8	-66.3

According to the PZR $\pi-$coefficients shown in Table 2.1, the estimation of π_L and π_T in $p-$type and $n-$type bulk (001) silicon under $\langle 110\rangle$ stress direction are shown in Table 2.2. In Chapters 4 and 6 of this thesis the standard (i.e. non-giant, non-anomalous) PZR of silicon will be taken to be these values for $p-$type and $n-$type silicon. The giant or anomalous PZR of nano-silicon obtained in this work will be compared with these values.

2.2 Piezo-resistance in charge neutral silicon

Let's take a step back and look at Eq. (2.3), the PZR consists of two terms, the geometric and resistivity changes induced by stress. Dividing both sides of this formula by the applied mechanical stress, the resistance π-coefficient can be related to known resistivity π-coefficient. According to Hooke's law, the mechanical stress is written as: $X = E\varepsilon$, E is Young's modulus, Eq. (2.3)is:

$$\frac{\Delta R}{R_0}\frac{1}{X} = (1+2\nu)\frac{1}{E} + \frac{\Delta\rho}{\rho_0}\frac{1}{X}, \tag{2.29}$$

$\frac{\Delta\rho}{\rho_0}\frac{1}{X} = \pi_\rho$, is the resistivity π-coefficient. Similarly $\frac{\Delta R}{R_0}\frac{1}{X} = \pi_R$ refers to the resistance π-coefficient. People always measure π_R instead of π_ρ, because they always measure resistance and not resistivity. In the case of (001) silicon with the $\langle 110\rangle$ crystal direction mechanical stress, Young's modulus E is about 169 GPa [56], and Poisson's ratio, $\nu = 0.27$. The first term in Eq. (2.29) is therefore approximately $0.91\times 10^{-11}\ Pa^{-1}$. The second term according to Table 2.2 measured by Smith [17] is $71.8\times 10^{-11}\ Pa^{-1}$ so that $\pi_R = 72.71\times 10^{-11}\ Pa^{-1} \approx \pi_\rho$. Therefore in silicon, a resistance $\pi-$coefficient measurement gives us approximately π_ρ. Note that, this is not necessary true for all the materials.

The question we could ask ourselves is: *why exactly does the resistivity change with applied stress?* To answer this question, we need to take a look at the formula for resistivity. In the case of charge neutral $n-$type silicon (electrons are majority carriers), ρ is expressed as:

$$\rho = \frac{1}{n\mu_n q} = \frac{m^*}{nq^2\tau_m}, \tag{2.30}$$

where n is free electron density, μ_n is mobility of election, q is the absolute value of the electronic charge, τ_m is the momentum relaxation time and m^* is the electron's effective mass. We can see that the PZR may be the result of either a stress-induced effective mass change, a concentration change or a change in momentum relaxation time. The concentration change due to stress is principally the result of stress-induced volume changes which are expected to be of the order of the first term of Eq. (2.29) i.e. 0.91×10^{-11} Pa^{-1}. In fact the largest contribution to PZR in silicon is that due to stress-induced effective mass changes i.e. to changes in the mobility. The resistivity can be written as a function of stress:

$$\rho = \rho(X) = \frac{m^*(X)}{nq^2\tau_m}, \tag{2.31}$$

PZR in $n-$type bulk silicon

Stress-induced effective mass changes in $n-$type silicon are described by the many-valley charge transfer model [57]. The conduction band of silicon consists of six valleys whose constant energy surfaces are ellipsoids of revolution, and whose long axes are along the [100] crystal directions. In the absence of mechanical stress, the six ellipsoids are degenerate and therefore equally populated with electrons as shown in the left inset of Fig. 2.2 [14]. One refers to longitudinal and transverse valleys in the context of current flow. For example, for current flow along $\langle 100\rangle$ direction (see arrow in the inset of Fig. 2.2), the two $\langle 100\rangle$ valleys become the longitudinal valleys, while the $\langle 010\rangle$ and $\langle 001\rangle$ valleys become the transverse valleys. Because the valleys are ellipsoidal and not spherical, there are two effective masses associated with each valley: one corresponding to the major axis of the ellipse and one corresponding the minor axis of the ellipse. In the aforementioned example of current flow along the $\langle 100\rangle$ direction, the major axis of the two longitudinal valleys is parallel to the current flow direction, and the effective mass which counts in Drude's law is the longitudinal or parallel effective mass, $m_{\|}$. For the four transverse valleys however it is the effective mass associated with the minor axis of the ellipsoid which counts, the so-called transverse or perpendicular effective mass, $m_{\perp}$. The longitudinal effective mass $m_{\|} = 0.97m_0$ which is larger than transverse effective mass $m_{\perp} = 0.19m_0$ in silicon, $m_{\|} > m_{\perp}$ [57]. When a $\langle 100\rangle$ compressive stress is applied on the sample, the ellipsoids in the $\langle 100\rangle$ direction will shift down in energy with a deformation potential approximate 12.1 eV with respect to the four other ellipsoids [58, 51]. Since electrons always occupy lower energy states first, this will result in a transfer of electrons from the transverse valleys to the $\langle 100 \rangle$ crystal direction valleys (see middle insert in Fig. 2.2). Because $m_{\|}$ is larger than $m_{\perp}$, the density-of-states weighted effective mass of $n-$type silicon therefore increases due to compressive stress parallel to $\langle 100 \rangle$ crystal direction. According to Eq. (2.30), resistivity is proportional to effective mass, the resistivity increases. This effect has been studied many other works [16, 57, 59] and has been verified by recent work up to 3 *GPa* mechanical compressive stress parallel to $\langle 100 \rangle$ crystal direction on $n-$type silicon as shown in Fig. 2.2 [51]. The current flows parallel to the stress as shown inset, and the symbols denote measurements on different samples. Should be noted here: in convention, compressive stress is negative while tensile stress is positive. In this case, the slope of curves shown in Fig. 2.2 indicates the π-coefficient and the sign of π-coefficient shown in Fig. 2.2 is negative due to the definition in Eq. (2.4). Up to 1 *GPa* stress, the π-coefficient is relative constant due to linear slope. When stress is larger than 1 *GPa*, the π-coefficient begins to saturate. This is because under such high stress almost all the electrons in the transverse valleys have already transferred to the longitudinal valleys as shown in the right insert. This saturation observation well verifies the charge-transfer model.

PZR in $p-$type bulk silicon

The $\pi-$coefficient in $p-$type silicon is different from that of $n-$type silicon [60] because of the stress-induced redistribution of holes between valence bands, and due to band warping [20, 61–65]. For $p-$type silicon under zero stress, the heavy-hole band and light-hole band are degenerate at the Γ-point as shown in the left insert in Fig. 2.3. Under uniaxial compressive stress, the degeneracy is lifted and band warping occurs (i.e. the curvature of the energy band changes due to stress). The light-hole band moves to higher energy while the heavy-hole band moves to lower energy resulting in a band anti-crossing as shown in the middle insert in Fig. 2.3. Since the holes always occupy the maximum energy position in the valence band, then the holes in the heavy-hole band will transfer to the light-hole band. This is a very important point to have a PZR effect in $p-$type silicon, because the stress therefore reduces the density-of-states weighted holes effective mass. Since resistivity is proportional to effective mass, the resistance will decrease as well. The reported $p-$type PZR under uniaxial compressive stress up to 3 *GPa* confirmed this in Fig. 2.3 [51]), where $\frac{\Delta R}{R_0}$ approximately linearly decreases from 0 to 1 *GPa*. When the stress is larger than 1 *GPa* the slope of $\frac{\Delta R}{R_0}$ as a function of stress decreases, and continuously drops under higher stress. This is because under the increasing stress, the gap of anti-crossing band is increasing, like the right insert shown in Fig. 2.3. So that more and more holes in heavy-hole band will transfer to light-hole band, the holes in the light-hole band gradually dominate effective mass

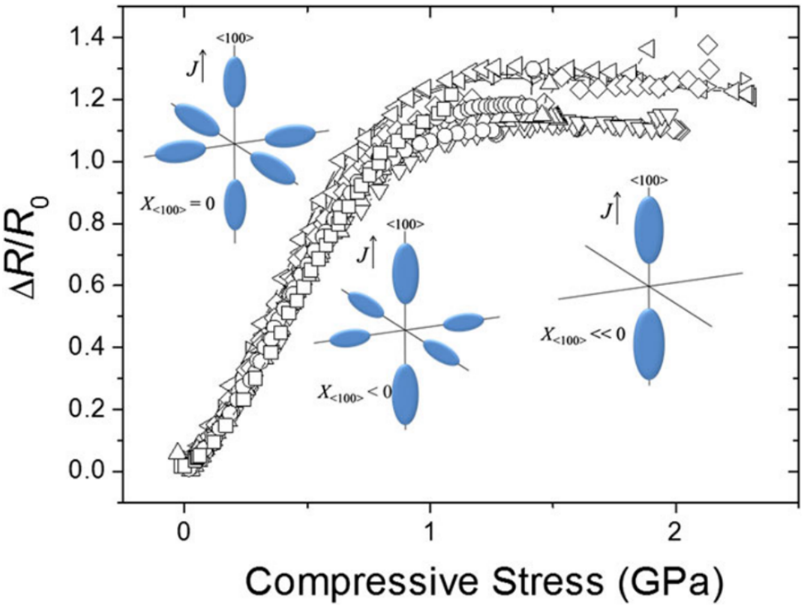

Fig. 2.2 The stress induced relative changes in resistance as function of compressive stress in $n-$type silicon [14] (results come from reference [51]). The process describe by the charge-transfer model is shown as schematic inserts. In the absence of stress, the six conduction band valleys are degenerate. Applying $\langle 100 \rangle$ compressive stress up to 1 *GPa* causes electrons to be transferred from the valleys perpendicular to the stress to the valleys parallel to the stress, and the π-coefficient is relatively constant. Further increases in stress yield a saturation in resistance because charge transfer between valleys is already complete.

in p-type silicon. Although we can't see from Fig. 2.3, a saturation of $\frac{\Delta R}{R_0}$ is expected at higher stresses.

In a conclusion, PZR in both $n-$type and $p-$type bulk silicon are due to a stress induced changes in the transport effective mass of carriers.

2.3 Space charge limited transport

Space-charge-limited currents (SCLC) can occur in lightly doped semiconductors, in insulators and even in vacuum between two electrodes. When a high voltage is applied across the electrodes, electrical charges are injected into the intervening space or material, forming a space-charge region. The current-voltage characteristic between the electrodes was first studied by Clement D. Child in 1911 [66]. A full investigation of SCLCs requires the frequency dependence of the impedance since in this way the physical time associated with SCLCs is revealed. This has previously been considered by several authors [67–77]. Here

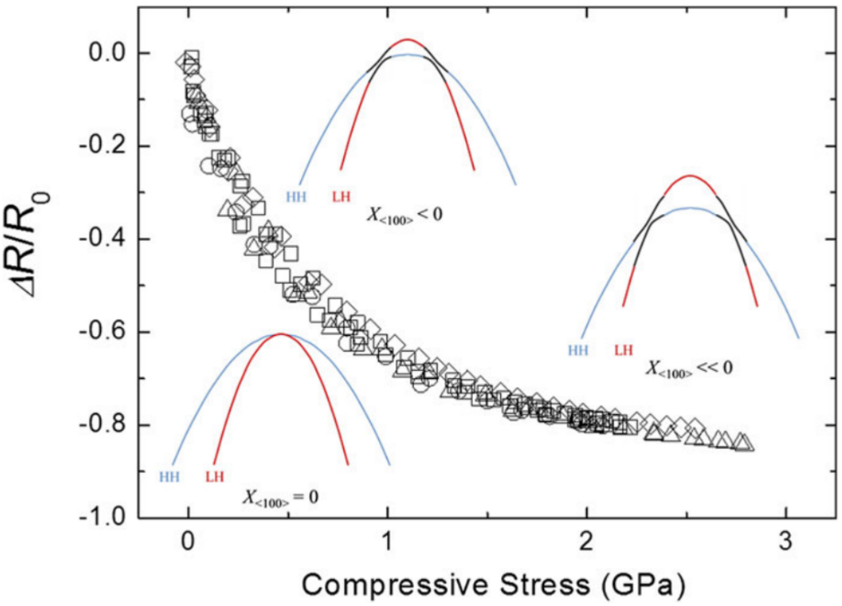

Fig. 2.3 The stress induced relative changes in resistance as a function of compressive stress in $p-$type silicon [14] (results come from reference [51]). The process is shown as schematic inserts. In the absence of stress, the heavy-hole and light-hole band are degenerate at the Γ-point. Applying compressive stress up to 1 GPa, the holes will transfer from the heavy-hole band to the light-hole band, and the π-coefficient is relatively constant. Further increases in the stress leads to a gradual saturation of $\frac{\Delta R}{R_0}$ as charge transfer becomes complete.

we will follow the presentation given by Shao and Wright [67]. Which considers an ideal dielectric material with the following assumptions:

- The medium is trap free.
- The medium has no thermally generated charge, any charge in the system is injected from the electrodes.
- The electrodes are low resistance Ohmic contacts.
- Only one type of carrier is present in the system (i.e. the unipolar case).

The one-dimensional current flows between two Ohmic contacts parallel to the x-direction, and the spacing between the electrodes is d. The overall current has three components: drift, diffusion and displacement currents expressed as:

$$J = \rho v + qD\frac{dp}{dx} + \varepsilon_0 \varepsilon_r \frac{\partial \mathscr{E}}{\partial t}. \tag{2.32}$$

Note that in this section of the thesis ρ refers to charge density, $\rho = pq$, where p is the hole density and q is the electronic charge. Since the devices used in this work are fabricated from $p-$type silicon, the above expression is written for holes, but an equivalent expression for electrons may also be used. To simplify this equation, one important assumption is made: the diffusion current is neglected compare to the drift current. Poisson's equation in one-dimensional is:

$$\frac{\partial \mathscr{E}}{\partial x} = \frac{pq}{\varepsilon_0 \varepsilon_r}, \tag{2.33}$$

where ε_0 and ε_r are the permittivity of the medium. The hole velocity, v, in the electric field $\mathscr{E}$ is:

$$v = \mu \mathscr{E}, \tag{2.34}$$

where μ is the hole mobility. Since the electric field is space and time dependent $(E(x,t))$ and the these two variables are dependent, $x = x(t)$, so that the differential equation of electric field with time can be written as two partial differential equation:

$$\frac{d\mathscr{E}}{dt} = \frac{\partial \mathscr{E}}{\partial x}\frac{dx}{dt} + \frac{\partial \mathscr{E}}{\partial t}, \tag{2.35}$$

so that Eq. (2.35) becomes:

$$\frac{d\mathscr{E}}{dt} = \frac{pq\mu\mathscr{E}}{\varepsilon_0 \varepsilon_r} + \frac{\partial \mathscr{E}}{\partial t}. \tag{2.36}$$

Substituting this into Eq. (2.32) yields:

$$J = \varepsilon_0 \varepsilon_r \frac{d\mathscr{E}}{dt}. \tag{2.37}$$

Further substitution of Eq. (2.34) into Eq. (2.37) gives:

$$J = \frac{\varepsilon_0 \varepsilon_r}{\mu}\frac{dv}{dt}. \tag{2.38}$$

Note that the current density J only exhibits a time dependence (and not a space dependence) since it's conserved throughout the medium. When a relatively small sinusoidal voltage (AC) is applied on a large steady (DC) voltage, the resulting current can be written as:

$$J = J_0 + J_1 exp(j\omega t), \tag{2.39}$$

where J_0 is the steady-current and J_1 is the amplitude of the small sinusoidal current. Substituting Eq. (2.39) into Eq. (2.38), we have that:

$$\frac{dv}{dt} = \frac{\mu}{\varepsilon_0 \varepsilon_r}(J_0 + J_1 exp(j\omega t)) \tag{2.40}$$

which, when integrated yields:

$$v = \frac{\mu}{\varepsilon_0 \varepsilon_r}(J_0 t + \frac{J_1 exp(j\omega t)}{j\omega}) + const. \tag{2.41}$$

We impose boundary conditions such that the electric field is 0 at $x = 0$ see Fig. 2.4 and the velocity of holes is also 0 at this point. Let t_c be the time that holes leave the electrode at $x = 0$ so that $v = 0$ when $t = t_c$. By using these conditions, Eq. (2.41) becomes:

$$v = \frac{\mu}{\varepsilon_0 \varepsilon_r}(J_0(t - t_c) + \frac{J_1 exp(j\omega t)}{j\omega} - \frac{J_1 exp(j\omega t_c)}{j\omega}). \tag{2.42}$$

Fig. 2.4 Boundary conditions used to determine SCLCs in a perfect dielectric medium.

Integrating again with the condition that $x = 0$ when $t = t_c$ yields

$$x = \frac{\mu}{\varepsilon_0 \varepsilon_r}(J_0(t - t_c)^2 + \frac{J_1 exp(j\omega t)}{(j\omega)^2} - \frac{J_1 exp(j\omega t_c)}{(j\omega)^2} - (t - t_c)\frac{J_1 exp(\omega t_c)}{j\omega}). \tag{2.43}$$

Consider the transit time $T_0 = t - t_c$ that the hole takes to travel a distance x in the medium. Then in steady-state the applied voltage is constant and $J_1 = 0$. Eq. (2.43) becomes:

$$x = \frac{\mu}{\varepsilon_0 \varepsilon_r}\frac{J_0 T_0^2}{2} \tag{2.44}$$

It can also be shown [67] that:

$$v = \frac{\mu}{\varepsilon_0\varepsilon_r}(J_0T_0) + \frac{\mu}{\varepsilon_0\varepsilon_r}\frac{1}{T_0}(\frac{J_1T_0}{j\omega} - \frac{J_1}{(j\omega)^2} + \frac{J_1exp(-pT_0)}{(j\omega)^2})exp(j\omega t). \tag{2.45}$$

This expression for the velocity can be separated into a steady-state component and a time-dependent component, as:

$$v = v_0 + v_1exp(j\omega t) \tag{2.46}$$

$$v_0 = \frac{\mu}{\varepsilon_0\varepsilon_r}(J_0T_0) \tag{2.47}$$

$$v_1 = \frac{\mu}{\varepsilon_0\varepsilon_r}\frac{1}{T_0}(\frac{J_1T_0}{j\omega} - \frac{J_1}{(j\omega)^2} + \frac{J_1exp(-j\omega T_0)}{(j\omega)^2}) \tag{2.48}$$

According to Eq. (2.34), the electric field $\mathscr{E}$ is proportional to v, and therefore the applied voltage V between the electrodes at $x = 0$ and $x = d$ (see Fig. 2.4) is :

$$V = \int_0^d \mathscr{E}\partial x = \frac{1}{\mu}\int_0^d v\partial x. \tag{2.49}$$

From Eq. (2.44) the relation between x and T_0 will be:

$$\partial x = \frac{\mu}{\varepsilon_0\varepsilon_r}J_0T_0\partial T_0. \tag{2.50}$$

We define here T_a as the transit time for a hole between the two electrodes, so that:

$$V = \frac{1}{\varepsilon_0\varepsilon_r}\int_0^{T_a}(v_0 + v_1exp(j\omega t))J_0T_0\partial T_0. \tag{2.51}$$

The applied voltage can also be separated into a steady-state component and a time-dependent component:

$$V = V_0 + V_1exp(j\omega t), \tag{2.52}$$

where

$$V_0 = \frac{1}{\varepsilon_0\varepsilon_r}\int_0^{T_a} v_0J_0T_0\partial T_0 \tag{2.53}$$

and

$$V_1 = \frac{1}{\varepsilon_0 \varepsilon_r} \int_0^{T_a} v_1 J_0 T_0 \partial T_0. \tag{2.54}$$

2.3.1 Steady state, space charge limited transport in semiconductors

From Eq. (2.53) it is possible to obtain the steady-state relationship between the current and the applied voltage in a space charge limited dielectric. Substituting for the steady-state velocity v_0 from Eq. (2.47), Eq. (2.53) for V_0 becomes:

$$V_0 = \frac{\mu}{\varepsilon_0^2 \varepsilon_r^2} J_0^2 \int_0^{T_a} T_0^2 \partial T_0. \tag{2.55}$$

Integrating Eq. (2.55) we obtain the steady applied voltage V_0 as a function of the hole transit time T_a:

$$V_0 = \frac{1}{3} \frac{\mu}{\varepsilon_0^2 \varepsilon_r^2} J_0^2 T_a^3. \tag{2.56}$$

Using Eq. (2.44) with $T_0 = T_a$ and $x = d$ yields the DC current-voltage characteristic of a SCLC in dielectric:

$$J = \frac{9}{8} \varepsilon_0 \varepsilon_r \mu \frac{V_0^2}{d^3} \tag{2.57}$$

This result is known as the Mott-Gurney law [78] and demonstrates that a non-linear current-voltage characteristic is the signature of an SCLC. This fact will be used throughout Chapters 4 and 6 of this thesis. The current density simulation according to Mott-Gurney law (see Eq. (2.57)) is shown in Fig. 2.5 as an example, the current is proportional to the voltage square. The permittivity used here is 11.9 for silicon, the vacuum permittivity is 8.85×10^{-12} Fm^{-1}, mobility μ is 425 cm^{-2}/Vs for very lightly boron doped silicon device and distance d between 2 contacts is 100 m.

Finally, by combining Eq. (2.56) and (2.57), the ratio between steady current and voltage is obtained and may be regarded as a "resistance" R:

$$R = \frac{V_0}{I_0} = \frac{V_0}{AJ_0} = \frac{2T_a d}{3A\varepsilon_0 \varepsilon_r} = \frac{2T_a}{3AC_g} \tag{2.58}$$

where A is the cross-sectional area of current flow and $C_g = \varepsilon_0 \varepsilon_r / d$ is the geometric capacitance of the device. The incremental resistance r can be obtained from Eq. (2.57) and (2.58)

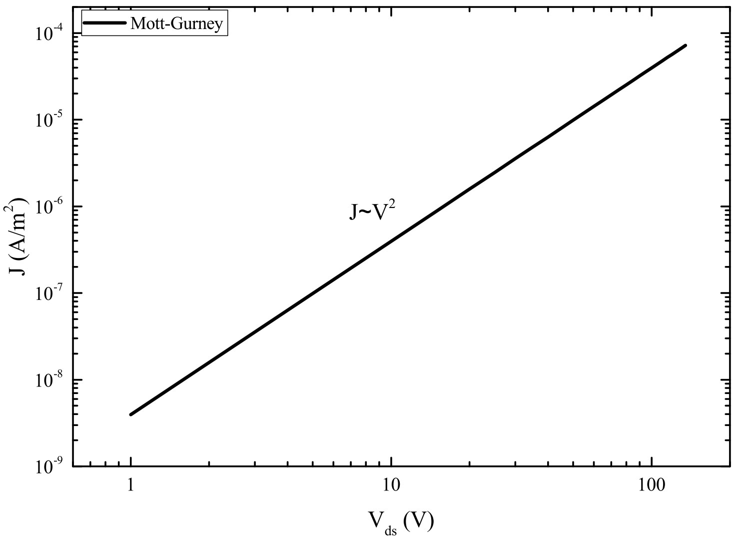

Fig. 2.5 The current density followed by Mott-Gurney law, since the plot is in log scale and slope is 2 which indicates that the current density is proportional to voltage square.

as:

$$r = \frac{\partial V_0}{\partial I_0} = \frac{V_0}{2I_0} = \frac{R}{2} = \frac{T_a}{3AC_g} \tag{2.59}$$

2.3.2 Small-signal, space charge limited transport in semiconductors

Now let's consider the small-signal situation in the material. The incremental admittance can be obtained by using the ratio between the time dependent components of the current and voltage. Substituting Eq. (2.48) into Eq. (2.54) and integrating, we obtain:

$$V_1 = \frac{\mu}{\varepsilon_0 \varepsilon_r} \frac{J_0 J_1}{(j\omega)^3} \left(\frac{(j\omega)^2 T_a^3}{2} - j\omega T_a - exp(-j\omega T_a) + 1 \right). \tag{2.60}$$

The incremental admittance is $Y_1 = I_1/V_1 = G_1 + j\omega C_1$, where:

$$G_1 = \frac{g\gamma^3}{6} \frac{\gamma - sin(\gamma)}{(\gamma - sin(\gamma))^2 + (\gamma^2/2 + cos(\gamma) - 1)^2} \tag{2.61}$$

and

$$\omega C_1 = \frac{g\gamma^3}{6} \frac{\gamma^2/2 + cos(\gamma) - 1)^2}{(\gamma - sin(\gamma))^2 + (\gamma^2/2 + cos(\gamma) - 1)^2}, \tag{2.62}$$

where the so-called transit angle is

$$\gamma = \omega T_a. \tag{2.63}$$

In these equations, $g = 1/r$ is the steady-current incremental conductance given as the inverse of the Eq. (2.59). This expression for the incremental admittance has been experimentally verified [67, 69, 70, 72, 74]. The frequency dependence of the normalized admittance is plotted in Fig. 2.6, where $G_g = g$. We can see from Fig. 2.6, for a trap free space charge limited medium, the conductance decreases and the capacitance increases as frequency increases, here we use $T_a = 10^{-4}$ s. This is the signature of a trap-free SCLC measured in the small-signal limit using the impedance spectroscopy techniques described in Chapter 3. At low frequencies, $\omega T_a \leq 1$, the impedance is constant and equal to $Y_1 = g + j\omega 3C_g/4$. At very high frequencies, $\omega T_a \geq 10$, the conductance and capacitance begin to oscillate, and eventually arrive at a constant value with $G(\omega T_a \geq 10) \approx 2G_g/3$ and $C(\omega T_a \geq 10) \approx C_g$. In the case of space charge limit, the carriers are injected from contact and contribute to the current. For the AC signal, the carriers are injected into the system during the positive half period and pull the carrier out at the negative half period. For the relatively low frequencies, $\omega T_a \ll 1$, the injection process is slow, the carriers are injected from one contact in the positive half period and reach to another contact in the same half period. At higher frequencies, $\omega T_a > 1$, the injection process is fast, the injected carriers do not have time to reach to another contact in the same half period, therefore the conductance decreases and capacitance increases when frequency increases. Hence, the space charge limited semiconductor can be represented as an equivalent circuit of R and C in parallel, for the case $\omega T_a \leq 1$, $R = G_g^{-1}$ and $C = 3C_g/4$; for the case $\omega T_a \geq 10$, $R = 3G_g^{-1}/2$ and $C = C_g$.

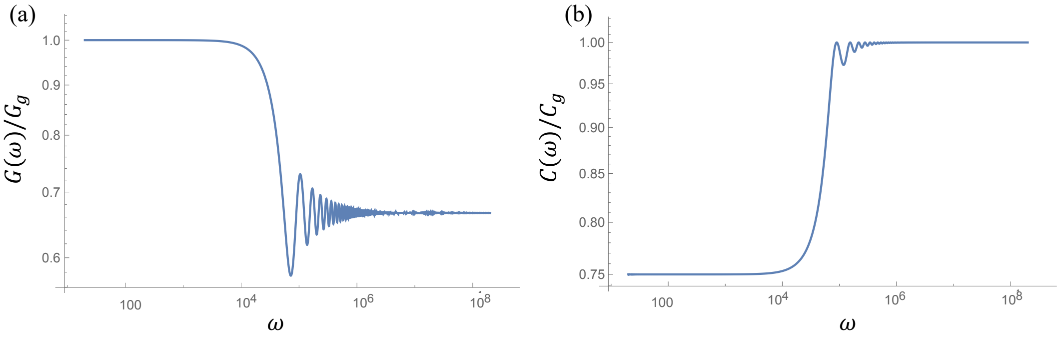

Fig. 2.6 (a) Normalized conductance and (b) normalized capacitance of a trap free space charge limited semiconductor versus the normalized angular frequency ω.

2.3.3 Small-signal space charge limited transport with a single trap type

We already discussed the admittance corresponding to a trap free space charge limited current, and will now consider the case where charge can be trapped in the medium during transport. Trapping of charge in semiconductors is usually treated using the Shockley-Read-Hall model (SRH) [79] in which the trap capture and trap emission rates, ω_c and ω_e are:

$$\omega_c(x,t) = C_p \frac{N_T - p_t(x,t)}{N_T} \tag{2.64}$$

and

$$\omega_e(x,t) = C_p \frac{p(x,t) + p_1}{N_T}, \tag{2.65}$$

where $p_t(x,t)$ is the trapped hole density, N_T is the trap density, $p(x,t)$ is the free hole density, p_1 is the density of holes that would be obtained if the Fermi energy lay at the trap energy ($E_F = E_T$) and C_p is the Shockley-Read-Hall capture constant for holes [79]. It should be noted that in the SRH model, $p_{t0}(x,t)$ and p_0 are space and time dependent, and so therefore are ω_c and ω_e.

The resolution of a full set of differential equations that includes Poisson's equation, Eq. (2.33), the current conservation equation, Eq. (2.32), and a rate equation for trapped charge containing both $\omega_c(x,t)$ and $\omega_e(x,t)$ has not been published. However, Kassing [74] has developed a simplified analytical model in which the equilibrium free hole density p_0 and the equilibrium trapped hole density p_{t0} are space and time independent, i.e. ω_c and ω_e are constant. In this approach only a single type of trap is present in the space charge limited semiconductor, meaning that the trap capture rate ω_c and emission rate ω_e are identical for all the traps.

Thus Kassing simplifies the expressions for ω_c and ω_e to be constant:

$$\omega_c = C_p \frac{N_T - p_{t0}}{N_T} \tag{2.66}$$

and

$$\omega_e = C_p \frac{p_0 + p_1}{N_T}. \tag{2.67}$$

While this approximation is clearly not representative of true space charge conditions where concentrations of holes vary strongly in space, it allows for a number of useful predictions to be made. In particular, the admittance is estimated to be [73, 74]:

$$Y(\omega) = \frac{g}{6}\frac{1}{\alpha}\{\sum_{k=0}^{\infty}\frac{(-i\omega\alpha T_a)^k}{(W+1)_{k+1}(k+3)}\}^{-1}. \tag{2.68}$$

The quantity α is frequency dependent and given by:

$$\alpha(\omega) = 1 + \frac{\omega_c}{i\omega_c + \omega_e}, \tag{2.69}$$

and W which appears in Eq. (2.68) is the product $\beta\alpha$, where $\beta^{-1} = \alpha(0)$. The notation $(W+1)_{(k+1)}$ is the so-called Pochhammer symbol:

$$(W+1)_{(k+1)} = \frac{\Gamma(W+k+2)}{\Gamma(W+1)}. \tag{2.70}$$

The real part of Eq. (2.68) yields the frequency dependent $G(\omega)$ while the imaginary part normalized to ω yields the frequency dependent $C(\omega)$. Generally speaking, the traps of interest in Chapter 4 are fast traps, meaning that $\omega_c \gg \omega_e$. As in the trap-free case treated previously, the values of $G(\omega)$ and $C(\omega)$ depend upon the medium's geometric capacitance C_g and conductance G_g and the source-to-drain transit time T_a. In addition they now also depend on the traps' characteristic capture (ω_c) and emission (ω_e) rates. The trap's properties (ω_c and ω_e) will result in a relaxation process which could produce an additional frequency dependence of admittance besides the transit time oscillation effect shown in Fig. 2.6. Note here, the product of transit time and trap capture rate $\omega_c T_a$ is generally much smaller than 1, which means $1/T_a \gg \omega_c$. Otherwise the transit time oscillation effect will dominate trap-induced relaxation process. The frequency dependence of the admittance according to Eq. (2.68) is shown in the Fig. 2.7.

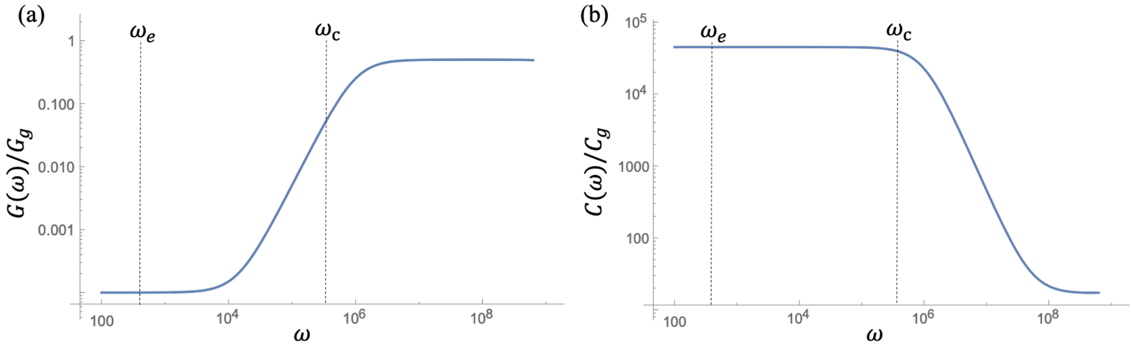

Fig. 2.7 (a) Normalized conductance and (b) normalized capacitance of a space charge limited medium versus the frequency ω in the presence of traps.

Several points which are critical for the interpretation of data shown in Chapter 4 should be noted:

- At low frequencies in Kassing's model, $\omega \ll \omega_c \ll 1/T_a$, the applied voltage period is long compare to the lifetime of injected carriers in the band $(2\pi/\omega_c)$, so that the injected, non-equilibrium charge fully relaxes from the band within a voltage cycle, i.e. the free charge population reaches steady-state. Results of conductance obtained in this frequency range are therefore directly comparable with those obtained using DC methods. For a fast traps, $\omega_e \ll \omega_c$, the majority of injected carriers are trapped in the steady-state [74], and the free carrier density in the band is approximately a factor $\theta = p_0/(p_0 + p_{t0})$ smaller than the trap-free case. This factor is also used by Murgatroyd [80] to describe trap-induced modifications to the Mott-Gurney law, Eq. (2.57), which will be used in Chapter 6 for the case of a DC voltage applied in the space charge limit in a semiconductor with a single implanted trap type. In the steady-state, the capacitance is maximum due to the large density of trapped charge [74]. The conductance and capacitance in the steady-state limit can be expressed as:

  $$G(\omega \to 0) \approx \frac{\omega_e}{\omega_c} G_g \approx \theta G_g \tag{2.71}$$

  and

  $$C(\omega \to 0) \approx \frac{1}{\omega_c T_a} C_g. \tag{2.72}$$

- At high frequencies, for example, $\omega \geq \omega_c$, the voltage period is short compared to $(2\pi/\omega_c)$ so that relaxation of injected charge from the band is negligible; in effect the medium behaves as if no traps were present. To within a factor of the order of unity, $G_0 \to G_g$ and $C_0 \to C_g$. The transition between this high-frequency limit and the steady-state limit occurs when $\omega \approx \omega_c$. This explains well the increasing conductance and decreasing capacitance with increasing frequency shown in Fig. 2.7.

2.4 Implication of Poole-Frenkel like effects

In the last section, the trap emission rate ω_e and ω_c were assumed to be constant in order to sufficiently simplify the model and to obtain an analytical expression for the admittance. However, the trap emission rate ω_e can be a function of applied DC voltage, on example of which is the Poole-Frenkel effect [81]. In equilibrium the traps contain a constant density of localized charge carriers determined by the dynamic balance of capture and emission processes. The emission rate from the trap level in the band gap of a semiconductor is exponentially proportional to the ionization energy E_i according to the Arrhenius equation [36]:

$$\omega_e = AT^2 exp(-\frac{E_i}{k_B T}), \tag{2.73}$$

where A is the Richardson constant. Generally speaking, when a strong electric field is applied on the semiconductor in the presence of the traps, the dynamic balance of the capture and emission process might change resulting in a change in the density of trapped charge carriers. This effect is illustrated as Fig. 2.8. With the application of an electric field, the potential barrier is lowered and trapped charge carriers need less energy to escape from the trap. This field-assisted emission could be due to a Poole-Frenkel effect or to phonon-assisted tunneling as shown in Fig. 2.8. In the Poole-Frenkel effect case, the barrier decreases by $\Delta\phi_{PF}$, which is proportional to the square root of the applied electric field $\mathscr{E}$ [81]:

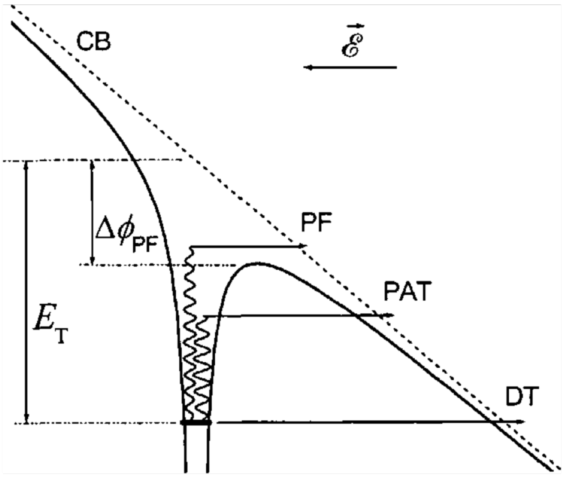

Fig. 2.8 Energy diagram of trap with application of strong electric field. There are 3 possible ways for a trapped charge carrier to escape as indicate as arrows: Poole-Frankel effect (PF), phonon-assisted tunneling (PAT) and direct tunneling (DT). Extracted from ref [82].

$$\Delta\phi_{PF} = B\sqrt{\mathscr{E}}. \tag{2.74}$$

where B is a field-independent pre-factor. The ionization energy E_i then becomes field-dependent:

$$E_i(\mathscr{E}) = E_i(0) - B\sqrt{\mathscr{E}}. \tag{2.75}$$

Therefore, ω_e strongly increases and the application of electric fields:

$$\frac{\omega_e(\mathscr{E})}{\omega_e(0)} = exp(\frac{\Delta\phi_{PF}}{k_B T}). \tag{2.76}$$

In the case of phonon-assisted tunneling, unlike Poole-Frenkel effect, the emission rate enhances exponentially with the square of the electric field [83]:

$$\frac{\omega_e(\mathscr{E})}{\omega_e(0)} = exp(\frac{\mathscr{E}^2}{\mathscr{E}_c^2}), \tag{2.77}$$

where $\mathscr{E}_c$ is a characteristic field strength, given by:

$$\mathscr{E}_c = \sqrt{\frac{3m^*\hbar}{e^2\tau^3}}, \tag{2.78}$$

where m^* is the effective mass of charge carriers, e is the elementary charge of the electron and τ is the tunneling time.

2.5 Conclusion

The background theories are introduced in this chapter in order to better understand bulk PZR and giant or anomalous PZR.

The strain or stress induced changes in resistivity of silicon result in PZR, the expression and experimental value of the longitudinal (π_L) and transverse (π_T) PZR with respect to the $\langle 110\rangle$ crystal direction are given in order to define the value of bulk PZR. Physical origin of bulk PZR in both $n-$type and $p-$type silicon are further discussed, which occurring in charge neutral silicon results from the stress dependence of the effective mass.

For depleted silicon nano-objects that can usually measure giant or anomalous PZR (see Fig. 1.8), an non-linear DC current-voltage characteristic like Mott-Gurney' law is an experimental signature of SCLC. Moreover, impedance spectroscopy in the small-signal limit predicts the presence or absence of traps in SCLC. Impedance spectroscopy yielding an increasing capacitance and decreasing conductance with increasing frequency, is a signature of a trap-free SCLC. While impedance spectroscopy yielding an decreasing capacitance and increasing conductance with increasing frequency, is a signature of a SCLC in the presence of traps. Most importantly, in a trap mediated SCLC impedance spectroscopy can be used to obtain information about the characteristic charge trapping and emission rates of traps. All these information as well as field-assisted emission can be used to analyze the measured giant, anomalous PZR in non-steady-state (see Chapter 4).

Chapter 3

Samples and experimental methods

This chapter will concentrate on the details of the experiments, which includes the material and fabrication of the samples, the set-ups used in this thesis, as well as the details of the experimental techniques. In section 3.1 the sample details are discussed: three different sample types, all made from silicon-on-insulator (SOI) wafers will be described. Two of them are used for the PZR measurements (see Chapters 4 and 6), while the other one is designed as a cantilever and used to measure the stress dependence of the surface Fermi level pinning (see Chapter 5). To apply uniaxial stress on the samples used for the PZR measurements, a 3-point bending apparatus will be presented in section 3.2. In section 3.3 and 3.4, the details of PZR measurements in steady-state using DC voltage, and the small-signal impedance spectroscopy (AC+DC voltages) will be introduced respectively.

3.1 Sample details

The samples used here are all provided by my co-supervisor, Prof. Steve Arscott, who works at the Institute of Electronics, Micro-electronics and Nanotechnology (IEMN), a research institute of the University of Lille, CNRS and École Centrale de Lille (UMR CNRS 8520). The samples shown in Figs. 3.1, 3.2 and 3.4 are specially designed for the 3-point bending apparatus shown in section 3.2, and the silicon cantilever samples shown in Fig. 3.3 are designed for the ultra-high vacuum (UHV) experimental station of the TEMPO beamline at the Soleil synchrotron.

3.1.1 Fully-depleted silicon nanomembranes

The samples introduced here are used to measure the PZR of SCLCs in silicon, the results of which are principally discussed in Chapter 4.

Silicon-on-insulator wafers

Commercial, wafer-bonded [84] silicon-on-insulator (SOI) wafers (*Si-Mat Silicon Materials, Germany*) are used for the fabrication of the samples. The silicon device layer (DL) has a thickness of 2 μm, the buried oxide (BOX) layer has a thickness of 1 μm and the silicon handle wafer (H) has a thickness of 400 μm. The orientation of the device layer, and the handle wafer, is (001). The diameter of the wafers is 3 inches. The silicon DL and H have a nominal resistivity of >1000 Ωcm.

Microfabrication

One 3-inch diameter wafer contains 11 rectangular chips whose dimensions (1.3 *cm* by 2 *cm*) are compatible with the 3-point bending apparatus discussed in section 3.2. The chips are fabricated using the planar photolithographic approach. This involves several standard microfabrication steps such as: deposition, masking, doping, etching, cleaning, and dicing. A set of physical photomasks was designed and fabricated for the microfabrication. The microfabrication steps are shown in the Fig. 3.1 and described as follows:

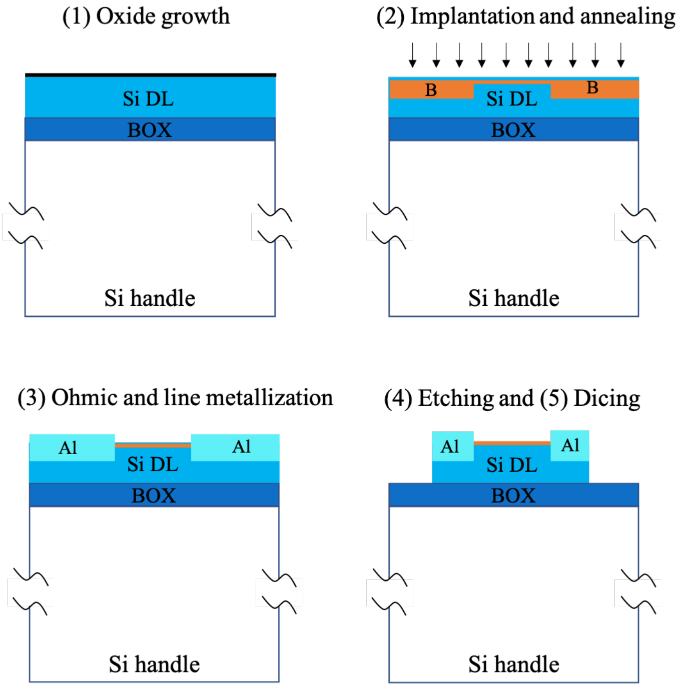

Fig. 3.1 Top-down sample fabrication process.

1. **Implantation oxide growth.** Following a standard RCA clean [85] a 45 *nm* thick silicon dioxide is grown on the DL surface by wet thermal oxidation in a furnace. The

purpose of this oxide is to ensure that the resulting boron implantation dopings are close to the surface to enable the formation of low resistivity ohmic contacts.

2. **Ion implantation (ohmic contact regions and on-chip strain gauge regions) and dopant activation.** The implantation doses and depths of the ohmic contact and on-chip strain gauge regions are calculated using software (SRIM) [86]. The ion implantations are conducted using a commercial machine (*GA 3204, Eaton-Axcelis*). Two ion implantation steps are performed using two different photomasks. The first photoresist mask (2 μm of *S1818 – Dow, USA*) is patterned (*MA-6 Karl Suss Microtec, USA*) and the ohmic contact areas are implanted using boron [87] (1×10^{20} cm^{-3}) to give a highly doped region [88]. The second photoresist mask (2 μm of *S1818*) is patterned and the moderately doped strain gauges are doped using boron (2×10^{18} cm^{-3}) to have a known piezoresistance [17] for the on-chip gauges – orientated in the $\langle 110 \rangle$ direction for a maximum piezoelectric coefficient for p-type material [18]. After each step, care is taken to fully remove the photoresist mask (resist stripper at 70°C, solvent clean, followed by oxygen plasma). Finally, a thermal anneal step (850°C/1 min in argon) is conducted in a rapid thermal processor (*AnnealSys, France*) to activate [89] the implanted species – diffusion will be minimal [90] at this temperature and time. Finally, the 45 nm thick implantation oxide is removed using a commercial buffered oxide etch - 7:1 volume ratio of 40% NH_4F in water to 49% HF in water.

3. **Ohmic and line metallization.** A third photomasking step is used to form a photoresist lift-off mask ($\sim$ 1 μm of *AZ1518 - Microchemicals, Germany*) for the ohmic contact and line metallization (300 *nm* of thermally evaporated aluminium – *MEB 550S Plassys, France*). Following a lift-off procedure, the ohmic contact ($Al - Si$) is formed in a Jipelec-JetFirst rapid thermal processor (*Semco Technolgies, France*) at 450°C/30s under forming gas (N_2/H_2) [91].

4. **Device layer etching**. A fourth and final photomasking step is use to form a photoresist (2 μm *S1818*) mask to be able to etch the 2 μm thick device layer. The goal of this is to define the device and on-chip strain gauge shapes and electrically isolate the devices and strain gauges from one another. The DL is etched down to the BOX using deep dry etching [92] (*Surface Technology Systems, UK*).

5. **Chip dicing, inspection, and initial electrical testing.** In order to complete the fabrication, the sample is diced into chips using an ADT 7100 precision diamond tipped saw (*Advanced Dicing Technologies, USA*). Prior to dicing, a 1 μm thick layer of photoresist (*AZ1518*) is spin coated onto the wafer and annealed at 100°C for 1

minute. Following dicing, the individual chips are cleaned in a resist stripper at 70°C for 30 minutes. The chips were then inspected using optical and scanning electron microscopy (*Ultra-55, Zeiss, Germany*). Initial current-voltage testing (non-linearity of devices, linearity of on-chip gauges, and resistance ladders) was performed using a probe station (*2612 System SourceMeter® (Keithley, USA)* and driven using *LabView®* software). The specific contact resistivity of the p-type ohmic contacts was measured using the ladder networks visible in the inset to Fig. 3.2(b) to be 1.6×10^{-6} Ωcm^2 [93]. During the process, all surface profiling (e.g. photoresist thickness, oxide thickness, etch depth...) was performed using a DektatXT stylus surface profiler (Bruker, Germany).

Chips layout

The chip layout was designed using commercial software (*Layout Editor, Germany*). Each rectangular chip (see Fig. 3.2)(a) measures about 1.3 cm by 2 cm and has a thickness of about 400 μm. The chips contain lowly doped (1.4×10^{13} cm^{-3}), fully depleted (FD) devices (see Fig. 3.2(b)) - each having an active width of 50 μm and a length of 30 μm which have ohmic contacts and lines which run to large area pads (2 mm × 2 mm) – the latter for external contacting. The chips also contain two moderately doped (2×10^{18} cm^{-2}) u-shaped [94], on-chip strain gauges (see Fig. 3.2(b)) composed of two 20 μm by 100 μm silicon parts in series which are also contacted to large pads on the chip edge. These gauges are used to monitor the local stress on the chip during the electromechanical measurements.

3.1.2 Silicon cantilever

The samples introduced here are used to measured the stress dependence of the surface Fermi level pinning, the results of which are principally discussed in Chapter 5. Simple macroscopic silicon cantilevers are made from a commercial (001) oriented silicon-on-insulator (SOI) wafer. The 5 μm thick sample layer is $p-$type doped (boron, $\rho < 0.01$ Ωcm). A 1 μm thick buried oxide (BOX) layer and a 400 μm thick handle are below the device layer. In order to form Ohmic contacts at each end of the cantilever, the device layer oxide is first removed by using a dilute (5 %) hydrofluoric acid solution, following which a 50 nm thick layer of aluminium is thermally evaporated onto the device layer via a shadow mask. During evaporation the surface is exposed to a low energy argon plasma, after which ohmic contacts are formed by annealing (600°C for 1 minute under a forming gas,95% $N_2/5\%$ H_2, atmosphere). A diamond saw is then used to cut 11 mm long, 3 mm wide cantilevers from the SOI where the long axis is parallel to the $\langle 110 \rangle$ crystal direction (see Fig. 3.3), the length

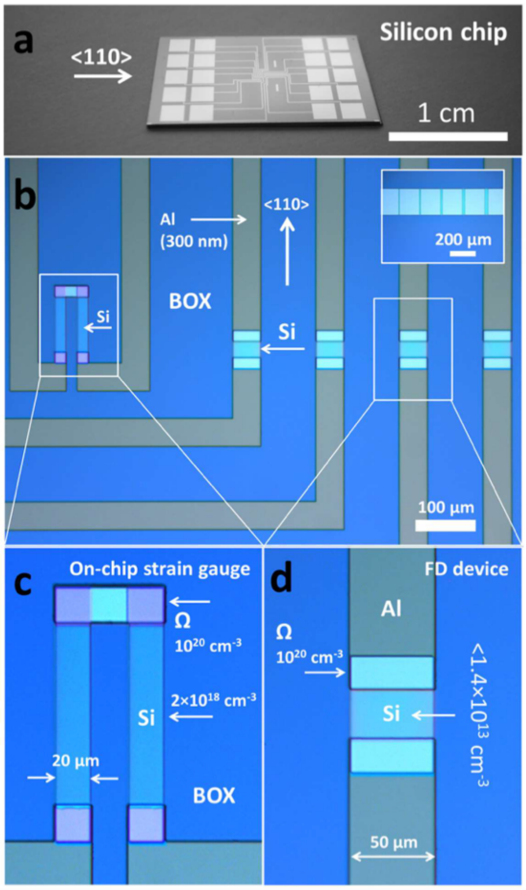

Fig. 3.2 (a) Photograph of the devices measured in Chapter 4. The large contact pads (2 *mm* × 2 *mm*) are visible on the chip which measures 1.3 *cm* by 2 *cm*. (b) On-chip strain gauges and devices. A silicon-based on-chip strain gauge (left) and four fully depleted silicon devices (right) are shown. The white scale bar is 100 *μm* long. The inset to the figure shows a resistance ladder used for the measurement of the specific contact resistivity. (c) The on-chip strain gauges. The silicon portions (20 *μm* × 100 *μm*) are doped $p-$type (Boron) to 2×10^{18} cm^{-3}. (d) The fully depleted silicon devices with thin native oxide layer on the top. The silicon portion (30 *μm* × 50 *μm*) has a resistivity of >1000 Ω*cm* – the background doping is boron which corresponds to a background doping level of $<1.4 \times 10^{13}$ cm^{-3}. The Ohmic contacts are doped (Boron) regions of 1×10^{20} cm^{-3}. The current flows in the devices and in the on-chip strain gauges parallel to the $\langle 110 \rangle$ crystal direction.

and width axes are defined as the x and y directions for the discussion presented in Chapter 5. The cantilevers, which are protected during this procedure with a 1 *μm* thick photoresist (*AZ1518*) layer, are cut so that the ohmic contacts are present at each end of the cantilever as shown in Fig. 3.3, the length of each ohmic contact is about 1.3 *mm*. Thus the silicon active area effective length of cantilever is approximate to 8.4 *mm* as marked in Fig. 3.3. Following dicing the cantilevers were stored with the photoresist in place for two months.

Two weeks prior to the experiments reported in Chapter 5, the photoresist was removed with a stripper (*SVC-14*), rinsed in acetone, isopropyl alcohol and de-ionized water before drying with nitrogen. During this time the device layer formed a native oxide in the ambient atmosphere (25°C, 45% r.h.).

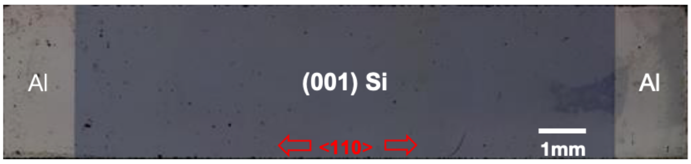

Fig. 3.3 $p-$type silicon cantilevers with ohmic contacts (*Al*) visible at each end used in the experiments reported on in Chapter 5. The (001) oriented silicon active layer is marked as *Si* with boron doping ($\rho < 0.01\ \Omega\ cm$). The long axis of the cantilever is parallel to the $\langle 110 \rangle$ crystal direction as indicated by the red arrows.

3.1.3 Silicon nanomembranes for defect engineering

The samples introduced here are used to measure anomalous PZR in defect engineered silicon, the results of which are principally discussed in Chapter 6. The wafer and fabrication procedure are the same as those for the sample discussed in section 3.1.1. The mask used during photo-lithography is however slightly different. As shown in Fig. 3.4, there are 10 silicon devices with 100 μm $\times$ 100 μm active area (see enlarged schema in Fig. 3.4) in the middle of sample shown as light blue blocks and labeled as D1 to D10. Each device is connected with two highly $p-$type doped ($10^{20}\ cm^{-3}$ Boron) Ohmic contacts. The number marked on the electrodes can help us to select the device we want to measure, for example, the electrodes labeled as 1 correspond to D1, etc.. In addition, since the sample is symmetric, the visible-by-eye *L* symbol on the sample is required to distinguish the orientation of the wafer. The current flows in the active device areas parallel to $\langle 110 \rangle$ crystal direction as for the sample shown in Fig. 3.2. Boron is used to dope the devices at two different doping levels: two among ten devices (marked by red rectangles) are doped to $10^{18}\ cm^{-3}$ and eight among ten devices are non-intentionally doped with resistivities $\rho > 5000\ \Omega cm$.

3.2 Apparatus for applying mechanical stress

In our experiment, mechanical stress is applied to the devices by using a 3-point bending apparatus. The left and right edges of the sample shown in Fig. 3.2(a) (and the top and bottom edges of the sample shown in Fig. 3.4) are held between a rigid clamp and sprung

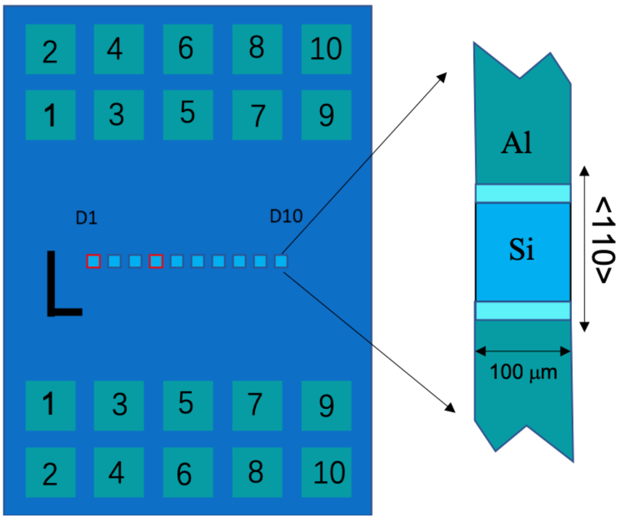

Fig. 3.4 The top-view of samples used in Chapter 6 is shown on the left, and there are ten silicon devices with two doping densities (Boron): the devices with red outlines are doped to 10^{18} cm^{-3} and the rest of the devices are non-intentionally doped with resistivities $\rho > 5000$ Ωcm. The large contact pads ($2\ mm \times 2\ mm$) are visible on the sample and allow us to select devices by the number order. The device is zoomed in on the right. Its surface area is 100 $\mu m \times 100$ μm and it is connected to the Al electrodes which form the Ohmic contacts, and the current flow direction is parallel to the $\langle 110 \rangle$ crystal direction.

electrical contacts (*PRECIDIP*) which make contact with $2\ mm \times 2\ mm$ external electrical contacts like those shown numbered in Fig. 3.4 and seen as silvered squares in Fig. 3.2(a). In the overall 3-point bending apparatus is shown in Fig. 3.5, the actuator pushes against one surface of the sample making it bend. In the case of applied tensile stress the actuator makes contact with the rear face of the sample (i.e. with the handle), and the applied force (F) is partially taken up by the sprung contacts, and partially taken up by the bending of the wafer as shown in Fig. 3.6(a). The thickness, width and length of sample are labeled as t, w and l in this schematic diagram, and in our case $w = 1.3$ cm, $l = 2$ cm and t is the

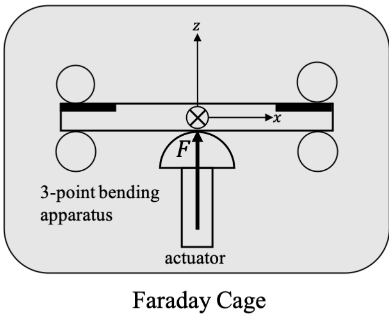

Fig. 3.5 Schematic of the 3-point bending apparatus used in Chapters 4 and 6.

total wafer thickness. Since the sample is perpendicular to z-axis shown in Fig. 3.6(b) and the cantilever edges are free in the y-direction the stress is uniaxial along the x-direction. This stress linearly varies with z and switches from compressive to tensile stress at an inner neutral surface (gray surface in Fig. 3.6(b)). The stress above the neutral surface is tensile, while the stress below it is compressive [95]. The maximum magnitude of uniaxial tensile and compressive stress occurs at the top and bottom surfaces of the sample (see Fig. 3.6(b)). This stress is given by [96]:

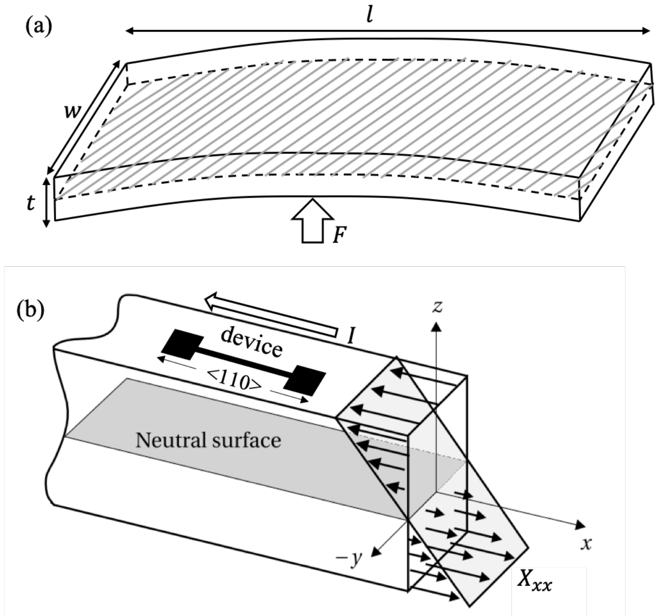

Fig. 3.6 Illustration of the sample bending. (a) A sketch of the sample bending due to the application of a force (F). (b) Illustration of the stress distribution in a sample deformed by the 3-point bending apparatus. The device is present at the top surface of the sample. In this case, a uniaxial tensile stress, X is applied on the device parallel to the $\langle 100 \rangle$ crystal direction as shown.

$$X_{max} = \frac{3Fl}{2wt^2}. \tag{3.1}$$

Since the substrate is much thicker than the device layer, then the stress applied in the this layer is approximately constant and equal to X_{max}. In the case of compressive applied stress the actuator makes contact with the front (i.e. device layer) face of the sample so that the applied force is taken up entirely by the bending of the wafer. In Chapters 4 and 6 X_{max} is approximately 20 MPa which, for the dimensions $l = 2 \times 10^{-2}$ m, $w = 1.3 \times 10^{-2}$ m and $t = 4 \times 10^{-4}$ m, $F = 1.4$ N. It can be shown [97] that the deflection of the centre of the wafer from its rest position is 2.2 μm.

3.3 DC (zero-frequency) piezo-resistance measurement procedure

Via the 3-point bending apparatus, a $\langle 110 \rangle$ direction uniaxial mechanical stress is applied on the sample, and the automatic electrical contact to the devices via the *PRECIDIP* connectors, allows us to measure the PZR using different techniques, the first of which is a simple DC resistance measurement. The complete schematic of the PZR measurement is illustrated in Fig. 3.7. In order to avoid dielectric relaxation induced resistance drift, the stress modulation technique is used here [38, 46]. The 3-point bending apparatus is put inside of an earthed Faraday cage to avoid the influence from external electrical fields. The actuator is manually positioned to be at the threshold of mechanical contact at the geometric centre of the sample via a ceramic sphere which ensures mechanical contact at only one point. Initially therefore, the sample is flat (see sample plotted by solid line in Fig. 3.7), and there is zero stress on the device. The current flowing through the device due to an applied DC bias is measured by a picoammeter (Keithley 485). The measured current, labeled I_{odd}, is automatically saved by the computer.

After a time $\tau/2$, the data acquisition card outputs a voltage signal to drive the actuator into the sample resulting in a bending as shown by the dotted line in Fig. 3.7). At this moment, the response current I_{even} is measured by the picoammeter and then saved by computer. Since the current is proportional to the conductance in Ohm's law according to Eq. (2.5), the $\pi-$coefficient can be expressed as:

$$\pi \approx -\frac{1}{I_0}\frac{\Delta I}{X}, \tag{3.2}$$

where $\Delta I = I_{even} - I_{odd}$ is the stress-induced change in the current and $I_0 = I_{odd}$ is the zero-stress current. Therefore when the actuator completes one single periodic motion in a time τ, one $\pi-$coefficient is obtained. The data acquisition card generates a square wave voltage on the actuator with a frequency of $1/\tau = 0.2\ Hz$ so that the stress applied on the device is modulated in time. Note here, the frequency of actuator is very small compare to the capture rate of traps (see section 4.2), therefore the influences result from actuator will be negligible because these influences will relax rapidly. During a total measurement time T, a number of T/τ of $\pi-$coefficient values are measured as shown in Fig. 1.6(b). The average of these yields the estimate for the $\pi-$coefficient of the device.

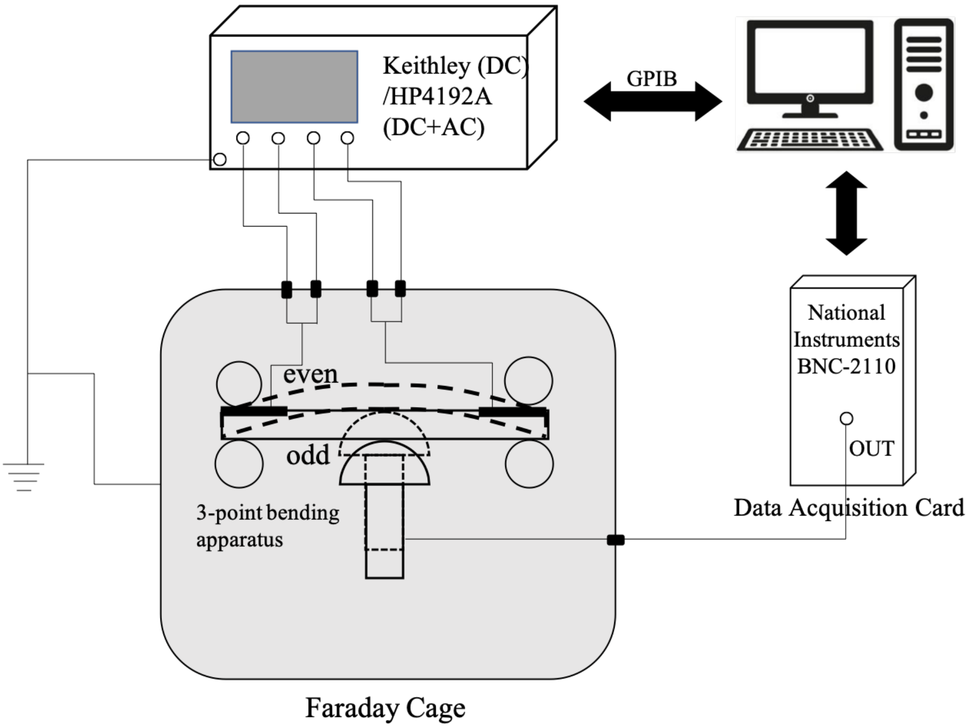

Fig. 3.7 Schematic of the PZR measurement. The sample and the 3-point bending apparatus are contained in a Faraday cage. The circuit between the signal detector (Keithley 485 for DC measurements or the HP4192A for impedance spectroscopy measurements) and the device allows us to measure the resistance of the device, which is then exchanged with a computer using a GPIB interface. In the mean time, an external voltage from the data acquisition card is applied on the actuator to provide the periodic mechanical stress on the device. The computer records the device's resistance or impedance with the modulation of stress in time.

3.4 Impedance spectroscopy and piezo-impedance measurement procedure

If the I-V characteristic of a device is linear, then the slope is proportional to its conductivity as shown in Fig. 3.8(a) and the π-coefficient can be estimated via a DC current measurement as expressed by Eq. (3.2). This is the approach used in all of the current PZR literature although the use of the stress modulation technique is far from universal [17, 21, 28, 29, 38, 41, 43, 46–48, 51, 98, 49, 99, 50].

If the I-V characteristic is non-linear as shown in Fig. 3.8(b), then the slope of the I-V characteristic changes as V_{DC} varies, i.e. the differential conductance of the sample changes with V_{DC}. The slope measured by a DC bias is always with respect to the origin ($V_{DC} = 0\ V$), and is not the real slope for a fixed V_{DC}. Thus the estimated conductance is not the true DC conductance. More importantly, the applied mechanical stress will also vary the slope of the I-V characteristic (see red curve in Fig. 3.8(b)), and it is therefore not possible to use the DC voltage method to estimate the π-coefficient. The wise move is to measure the differential conductance with a relatively small additional AC voltage on top of the fixed DC voltage. The amplitude of the additional AC voltage is much smaller than that of the DC voltage, and the total applied bias is:

$$V_{ds}(t) = V_{DC} + V_{AC} exp(i\omega t), \tag{3.3}$$

where V_{DC} is the DC component of the applied voltage and V_{AC} is the AC component applied at a frequency ω. In all the experiments reported in Chapter 4, $V_{AC} = 1\ V$. The

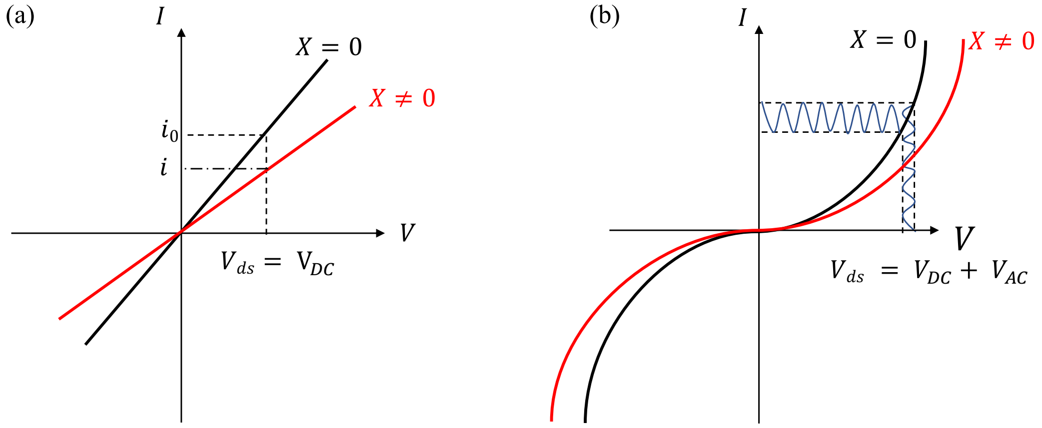

Fig. 3.8 PZR measurement in the case of (a) linear and (b) nonlinear I-V characteristic. The black curve corresponds to the stress free case while the red curve corresponds to the device with stress.

measured output current consequently has DC and AC components as well. Moreover the AC component of the current has an amplitude and phase, the latter of which can be measured relative to the phase of the AC applied bias (assumed for simplicity to be zero). The in-phase component of the current will yield the conductance according to $G = Re(I/V_{ds})$ whereas the out-of-phase component of the current can be assimilated with a capacitance according to $C = 1/\omega Im(I/V_{ds})$. In other words the overall device admittance is $Y = I/V_{ds} = G + j\omega C$. In the case of SCLCs in the presence of traps, G and C themselves are frequency dependent as discussed in Chapter 2.

Applied stress will change the admittance, and the in-phase and out-of-phase components of the current can then be associated with one of two $\pi-$coefficients: the PZR $\pi-$coefficient for the in-phase part,

$$\pi_R = -\frac{1}{G_0}\frac{\Delta G}{X}, \tag{3.4}$$

where G_0 is the effective conductance at non-stress applied and ΔG is the stress-induced change in G, and the piezo-capacitance (PZC) $\pi-$coefficient for the out-of-phase part,

$$\pi_C = -\frac{1}{C_0}\frac{\Delta C}{X}, \tag{3.5}$$

where C_0 is the effective capacitance at non-stress applied and ΔC is the stress-induced change in C. The expression for the overall piezo-response can be given by the piezo-impedance (PZZ) $\pi-$coefficient,

$$\pi_Z = \pi_R \frac{G_0^2}{G_0^2 + \omega^2 C_0^2} + \pi_C \frac{\omega^2 C_0^2}{G_0^2 + \omega^2 C_0^2} + i(\pi_R + \pi_C)\frac{\omega G_0 C_0}{G_0^2 + \omega^2 C_0^2}. \tag{3.6}$$

This expression implies the piezo-impedance depends on frequency ω. For low frequencies where $\omega \ll G_0/C_0$, $G_0^2/(G_0^2 + \omega^2 C_0^2) \sim 1$, $\omega^2 C_0^2/(G_0^2 + \omega^2 C_0^2)$ and $\omega G_0 C_0/(G_0^2 + \omega^2 C_0^2)$ ~ 0. Thus the piezo-resistance dominates piezo-impedance at low frequency regime. For high frequencies with condition of $\omega \gg G_0/C_0$, $G_0^2/(G_0^2 + \omega^2 C_0^2) \sim 0$, $\omega^2 C_0^2/(G_0^2 + \omega^2 C_0^2)$ and $\omega G_0 C_0/(G_0^2 + \omega^2 C_0^2) \sim 1$. Thus piezo-capacitance dominates piezo-impedance at high frequency regime. For intermediate frequencies, the piezo-impedance is expected to transfer to piezo-capacitance from piezo-resistance.

HP4192A impedance analyzer

The HP4192A impedance analyzer presented in Fig. 3.9(a), is used to accurately measure the impedance parameters of a component or circuit. The frequency, oscillation level and DC bias level range of HP4192A are as follows:

- Measuring Frequency: 5 Hz to 13 MHz
- OSC Level: 5 mV to 1.1 V
- DC bias voltage: -35 V to +35 V

The measured impedance parameters are shown in the conductance and capacitance display panel (see Fig. 3.9(a)). To measure the impedance of a device under test (DUT), a four terminal pair configuration is required which consists of 4 connectors: High current (H_{CUR}), High potential (H_{POT}), Low potential (L_{POT}) and Low current (L_{CUR}). The sketch of this four terminal pair configuration is shown in Fig. 3.9(b): the current flows through the DUT between two current terminals and is measured by a vector ammeter. Two potential terminals on both sides of the DUT are for detecting the voltage drop across the DUT by a vector voltmeter. Based on the magnitude and phase measured from the vector ammeter and the vector voltmeter, the impedance of the DUT can be estimated. As shown in the Fig. 3.7, the measured devices are placed in a Faraday cage so that the cables connecting the DUT to the HP4192A can also be regarded as part of the DUT. This affects the accuracy of impedance measurement. The inaccuracy principally results from a phase change and signal loss during propagation along the cable length. Since the cable-length-induced measurement error increases in proportion to the test frequency, the cable length must be taken into account in high frequency measurements. In this case a 16048A fixture is required which consists of four 1-metre-long coaxial cables whose line capacitance and conductance are compensated for automatically by the impedance analyzer once the CABLE LENGTH switch on the front panel is set to the 1 m position. Generally, in the absence of any other correction, the HP4192A will report relatively accurate conductance and capacitance of anything attached to these four cables.

However, the depleted devices measured here are two-terminal devices, so a conversion from four to two contacts is necessary, and is achieved according to the configuration shown in Fig. 3.9(c). The two additional 10 cm coaxial cables also results in parasitic signals that will affect the accuracy of impedance measurement. In order to obtain only the sample's impedance, HP4192A has a ZERO CORRECT function. Zero correction of the excess line impedance is achieved in two steps. First, the mainly reactive component of the excess line impedance is corrected by removing the sample and using the ZERO OPEN function.

Second the mainly resistive component of the excess line impedance is corrected by replacing the sample with a short circuit blade (a 200 *nm* thick gold layer on glass) and using the ZERO SHORT function. During this procedure it is important to keep the geometry of the 10 cm coaxial cables as constant as possible, since to do otherwise may change parasitic line impedances. In subsequent measurements with the ZERO OPEN and ZERO SHORT functions activated, the impedance analyzer will report the impedance of the DUT only.

Since relatively accurate estimations of conductance and capacitance can be measured by the HP4192A impedance analyzer, the PZR and PZC can also be obtained by using the configuration shown in Fig. 3.7 which uses the stress modulation technique according to Eq. (3.4) and (3.5) for a particular frequency. In general, HP4192A impedance analyzer is set to automatically average ten times measured impedance parameters with and without stress applied, and then transfer these results to the computer to estimate the piezo-response. In our experiment, this whole process is set to repeat twenty times, which means the final reliable results, G_0, C_0, π_R, π_C and π_Z are obtained after two hundred measurements which are then averaged. According to Eq. (3.6), these quantities may all be functions of frequency, and for this reason measurements are made over a frequency range from 100 Hz up to 10 MHz. This procedure is called impedance spectroscopy.

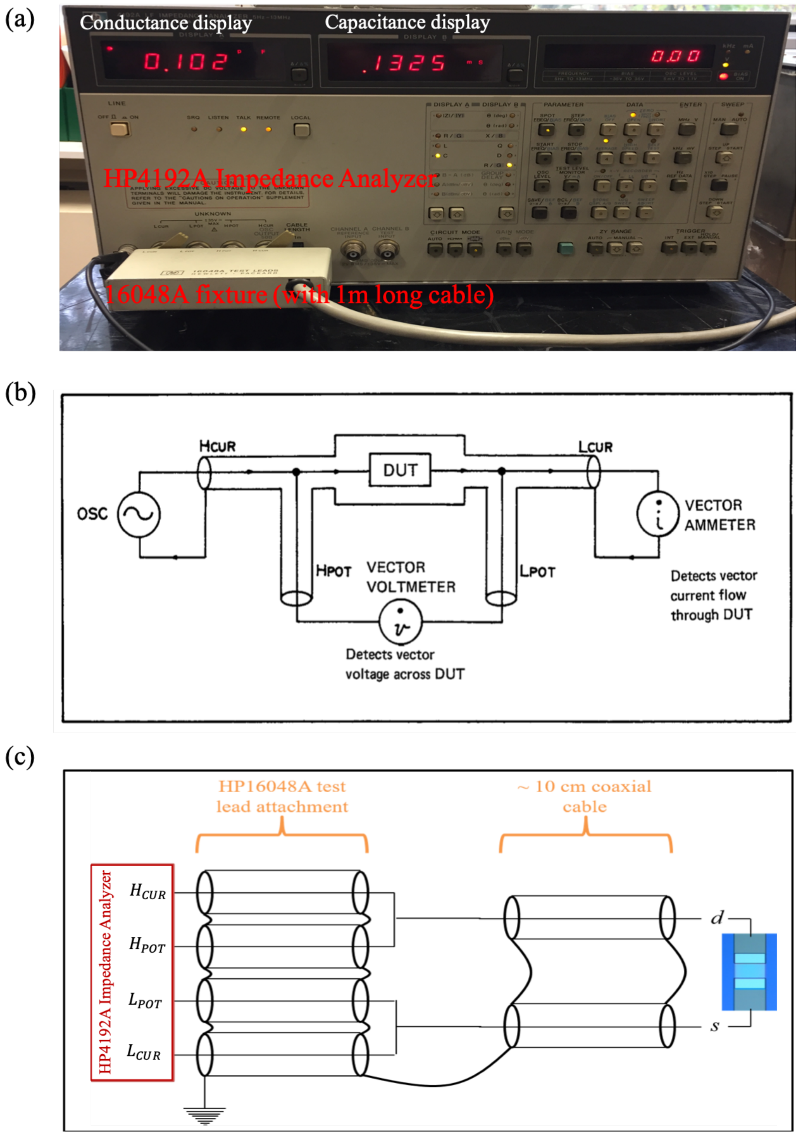

Fig. 3.9 A sketch of the HP4192A impedance analyzer measurement principle. (a) The photo of HP4192A impedance analyzer with a four terminal fixture 16048A. The principle of this four terminal pair measurement is drawn in (b) [Cited from HP4192A Guide Manual], the estimation of impedance is made according to a two-terminal vector ammeter measurement and a two-terminal vector voltmeter measurement. The measured impedance can be read directly from the front panel display. (c) Schematic diagram of the four-to-two terminal contact conversion used to obtain the impedance of the device between source (s) and drain (d) using a HP4192A impedance analyzer with four output terminals, High current (H_{CUR}), High potential (H_{POT}), Low potential (L_{POT}) and Low current (L_{CUR}). The impedance of the four 1 m long coaxial cables making up the HP16048A test lead attachment is automatically compensated for, while the correction for the impedance of the added 10 cm coaxial cables is made using the analyzer's ZERO CORRECT function.

Chapter 4

Observation of a giant, anomalous piezo-response in space charge limited silicon

In this chapter measurements of the piezo-response of the two-terminal devices described in Chapter 3 are reported. The devices are fabricated from the device layer of a so-called fully-depleted silicon-on-insulator (FDSOI) wafer in which the background doping corresponds to a surface depletion layer width $W \approx 10\ \mu m$ while the device layer thickness is $d = 2\ \mu m$. The devices are therefore depleted and transport occurs in the space charge limit. Evidence for this will be shown by the non-linear current-voltage characteristic.

The non-linearity of the characteristic was in fact the first motivation for the impedance spectroscopy measurements since a true measurement of π_R cannot be achieved using standard DC methods in this case. It was expected therefore that a V_{DC} dependent π_R (corresponding to different values of the differential conductance) would be seen, but in fact the use of impedance spectroscopy proved to yield far greater treasures than this.

This chapter shows, thanks to impedance spectroscopy, the existence of giant and anomalous PZR under non-steady-state conditions (in devices whose steady-state PZR is just the usual bulk effect), but the existence of a novel piezo-capacitance effect.

The power of the impedance spectroscopy method is used to prove that these unusual phenomena results from stress-induced variations of charge trapping dynamics at unidentified fast electronic traps. This conclusion is supported by a study of the DC voltage dependence of the effects. Finally the symmetry of the giant PZR and PZC in stress indicates tentatively that the fast traps responsible for both phenomena are those due to interface defects i.e. intrinsic $Pb-$like defects at the Si/SiO_2 interface.

4.1 DC I-V characteristics of an FD-SOI device: evidence for space charge limited currents (SCLC)

A side view schematic of the device is shown in Fig. 4.1(a). The top black layer is a several *nm* native silicon oxide due to exposure in the air. The current flows between 2 metallic Ohmic contacts, the source and drain (labeled *s* and *d* in the Fig. 4.1(a)). The measured I-V characteristic under steady DC voltage is not Ohmic, but is rather non-linear as shown by the blue dots in Fig. 4.1(b). The simulated I-V curves according to Ohm's law and Mott-Gurney's law (see Eq. (2.57)) are presented as red and green curves respectively. The agreement between the non-linear I-V characteristic and Mott-Gurney's law indicates the FD-SOI devices are in the space charge limited regime for the reasons discussed in section 2.3. However, the non-linear I-V characteristic is not perfectly quadratic (see the difference between blue dots and green curve), and this could be due to a voltage dependence of the trap emission rates according to Poole-Frenkel like effects as discussed in section 2.4 [81, 100]. Further details along these lines will be discussed in Chapter 6 for the defect engineered samples.

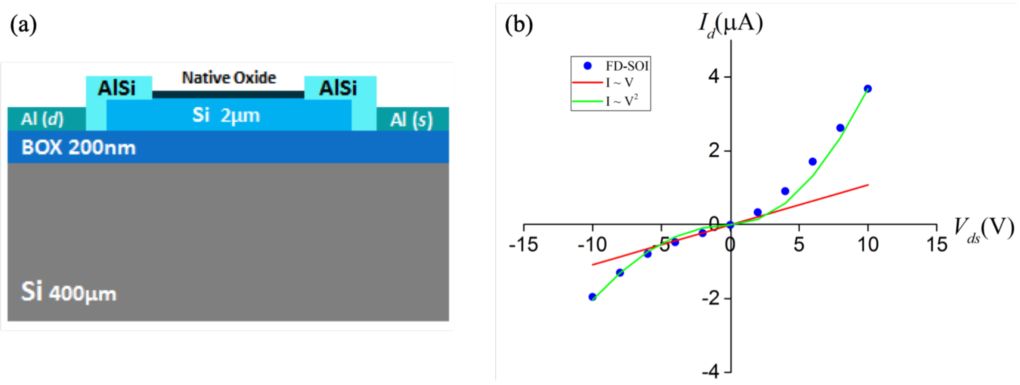

Fig. 4.1 (a) Side view schematic of the FD silicon device, the current between two electrodes parallels to $\langle 110 \rangle$ crystal direction. While the device is contacted via low resistance Ohmic contacts, the current-voltage characteristics are non-linear, (b), which implies the depleted device is in space charge limited (SCL). The simulated I-V characteristic according to Ohm's law and Mott-Gurney's law are presented as red and green curves respectively.

4.2 Impedance spectroscopy at zero stress: evidence for trap-mediated SCLC

Using the experimental configuration shown in Fig. 3.7 with the HP4192A impedance analyzer as the detector, the impedance spectrum is obtained. In this section, we only concentrate on the measured conductance and capacitance as a function of frequency at zero stress. Note here that the maximum DC bias V_{DC} in the experiment is 10 V, and the additional AC bias V_{AC} is fixed at 1 V.

The frequency dependent conductance G and capacitance C under different V_{DC} (labeled by color) are shown in Fig. 4.2(a) and (b) respectively. Clearly, G increases, while C decreases as the frequency increases; both are relative flat at low frequencies. V_{DC} is also able to vary G and C, especially for low and medium frequencies. The strong voltage dependence of G observed at low frequencies in Fig. 4.2(a) is interpreted as being due to the voltage dependence of ω_e via a so-called phonon-assisted tunneling effect which will be discussed further in section 4.5.

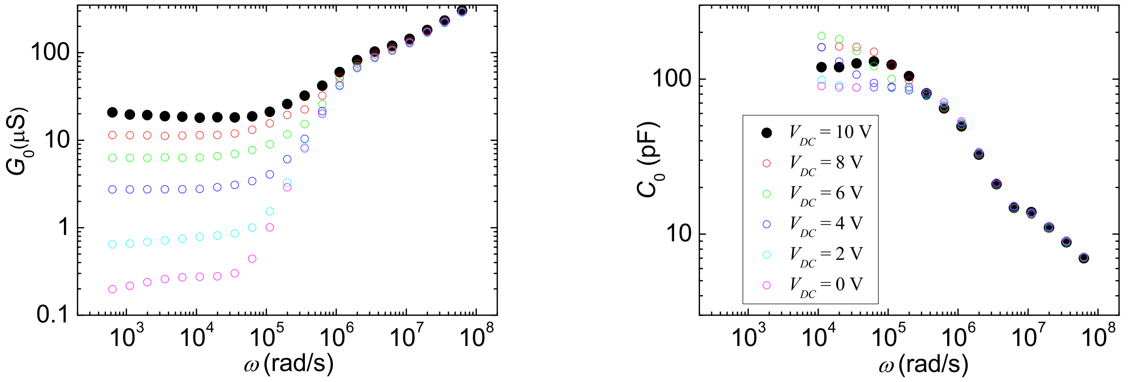

(a) Conductance as a function of frequency.

(b) Capacitance as a function of frequency.

Fig. 4.2 Zero-stress measurements of G_0 (top) and C_0 (bottom) as a function of ω and V_{DC}. At low frequencies capacitance measurements are difficult and the data is not shown.

From the non-linear I-V characteristic of FD-SOI device (see Fig. 4.1), we already knew that device is in the SCLC regime. The frequency dependent conductance and capacitance of a space charge limited semiconductor are shown in the Fig. 2.6 and 2.7 for the trap free and with trapping cases respectively. Obviously, the frequency dependence of G and C shown here imply that the devices are space charge limited and that traps are present in the active area. Therefore Kassing's model (see section 2.3) will be used to model the impedance as well as the piezo-response (see section 4.4). To make the demonstration as simple as possible, Kassing's model will be applied mainly to data obtained when $V_{DC} = 10\ V$ in the remainder of this chapter. In this section, we only focus on the simulation of zero-stress impedance as a function of frequency.

As discussed in section 2.3, Kassing's model considers only a single type of trap and charge carrier case. However, in reality, the device contains a continuous distribution of traps as indicated by the asymmetric, broad hump centered at about 180 K in the photo-induced current transient spectroscopy (PICTS) signal shown in Fig. 1 of Appendix A. Broad PICTS signals are usually indicative of a continuum of traps whose spectrum is spread by disorder at the silicon/oxide interface [101]. These traps may have different properties, such as relative densities, and capture and emission rates. To fully describe frequency variation of G and C by using Kassing's model, a compromise solution consisting of the inclusion of a finite number of different trap types is considered. Here 6 traps represented by colored curves (orange, red, green, purple, brown and cyan) in Fig. 4.3(a) and (b) are introduced. The overall value of G_0 and C_0 are obtained by the sum of Kassing's equivalent circuit of each trap in parallel combination as indicated in the inset of Fig. 4.3(b).

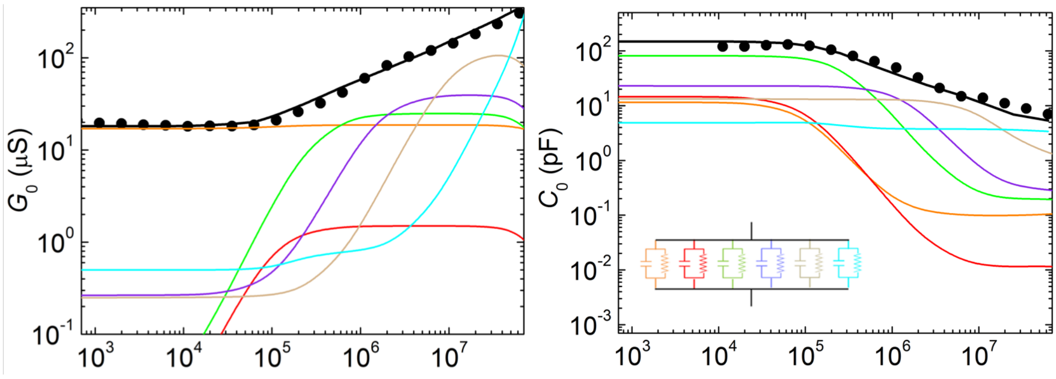

(a) Simulated conductance.

(b) Simulated capacitance.

Fig. 4.3 Simultaneous modelling of zero-stress data (black dots) obtained as a function of frequency for $V_{DC} = 10\ V$. Six individual trap types represented by the coloured curves (orange, red, green, purple, brown and cyan) are used to simulate a quasi-continuous trap distribution. The individual results are added in parallel (see inset in (b)) to obtain the overall response (black curves). Fit parameters can be found in Tables 4.1

The individual values of the conductance and capacitance for each trap type are calculated using Kassing's model with the parameters shown in Table 4.1:

As the density of the different trap types are not same, a pre-factor is used to weight each individual curve, G_0 and C_0 (the trap weight in Table 4.1), which indicates relative densities of each of the six traps (see the column labelled Relative weight (%) in Table 4.1). Apart

Table 4.1 The fitting parameters used with Kassing's model [74] to calculate G_0 in Fig. 3.7(a), and C_0 in Fig. 3.7(b).

Trap number	**Line color in Fig. 3.7**	ω_c (rad/s)	ω_e (rad/s)	**Trap weight**	**Relative weight** (%)
1	orange	800	10^4	0.19	2.1
2	red	10^5	100	0.03	0.3
3	green	3×10^5	100	0.5	5.5
4	purple	1.5×10^6	5000	0.8	8.9
5	brown	10^7	10^4	2.5	22.7
6	cyan	10^8	10^5	5	55.4

from these trap specific parameters (like Trap weight, ω_c and ω_e) shown in Table 4.1, there are several parameters with a single value for all six traps:

- Source-to-drain transit time: $T = 2\times10^{-8}\ s$
- Geometric conductance: $G_g = 1\times10^{-4}\ S$
- Geometric capacitance: $C_g = 6.5\times10^{-13}\ F$

The geometric capacitance and conductance can be observed at very high frequency ($\omega \gg \omega_c$) according to the discussion in section 2.3, and the values of G_g and C_g used here are chosen to be approximately compatible with the high frequency data shown in Fig. 4.3. A reasonable first guess for T can be made using the hole mobility, $\mu_p \approx 0.03\ m^2/s$, the distance between contacts, $d = 30\ \mu m$, and an electric field $\mathscr{E} = V_{DC}/d = 1/3\times10^{-5} \approx 3\times10^5\ V/m$. Then $T = d/(\mu_p\mathscr{E}) = 3\times10^{-8}\ s$.

The overall values of G_0 and C_0 are estimated by adding the individual weighted Kassing curves (see the coloured lines in Fig. 4.3) for the conductance and capacitance values in parallel as indicated (inset) in Fig. 4.3(b). In Table 4.1, it is interesting to note that in all cases except one (trap type number 1), the traps are fast ($\omega_e \ll \omega_c$), with the remaining case, depicted in orange in Fig. 4.3, being slow i.e. $\omega_c < \omega_e$. The choice of parameter values must simultaneously fit both G_0 and C_0 data, so the excellent agreement between the calculated values (black curves in Figs. 4.3(a) and (b)) and the data (filled, black circles) is highly satisfactory. In summary, the non-linear I-V characteristic and frequency dependence of conductance and capacitance indicate that the FD-device is in the SCLC regime in the presence of fast traps.

4.3 Frequency dependence of the piezo-impedance at fixed, tensile stress

In this section, the effect of an external tensile, uniaxial mechanical stress of approximately 25 MPa applied parallel to the $\langle 110\rangle$ crystal direction is studied. The PZR and PZC measured using the HP4192A impedance analyzer will be represented and discussed.

PZR and PZC are estimated according to Eq. (3.4) and Eq. (3.5) and shown in Fig. 4.4 under variable DC voltage as a function of the frequency of the small AC voltage component. PZR and PZC are not constants with variable frequency, but changing as a function of frequency. Apart from normal $p-$type bulk PZR, the giant, anomalous PZR has been measured as well. In the limit $\omega \to 0$, i.e. when the measurement frequency is significantly smaller than the capture rates of each of the traps shown in the Table 4.1, the measured π_R is approximately equivalent to the bulk value $+70 \times 10^{-11}$ Pa^{-1} [17] shown as the red dashed line in Fig. 4.4(a). Although there is a slight variation with V_{DC}, it is never more than a factor of two different from the accepted bulk value. This is consistent with previous DC PZR measurements on this type of sample [38]. In contrast, a strong dependence of the PZR is observed in a defect engineered sample over a larger DC voltage range as discussed in Chapter 6.

As the frequency is increased, there is an obvious variation of PZR with V_{DC} at medium frequencies (frequency around 1×10^5 rad/s), followed by a drop and a sign change. At higher frequencies the PZR has an anomalous sign (negative) and a giant magnitude, peaking at $\pi_R \approx -1100 \times 10^{-11}$ Pa^{-1}, more than an order of magnitude larger than the bulk effect, around $\omega \approx 1 \times 10^7$ rad/s. The capture rate ω_c for each trap in the Table 4.1 are marked as dotted lines in Fig. 4.4(a) to help us to compare it with applied frequency. A novel PZC with large magnitude and negative sign is also reported here. A voltage dependence is also seen especially in the the low frequencies, but a systematic trend with V_{DC} is hard to identify. As the frequency is increased, the PZC increases in magnitude to approximately π_C $\approx -900 \times 10^{-11}$ Pa^{-1} at $V_{DC} = 10$ V before changing sign at the highest frequencies.

4.4 Theoretical description of the frequency dependence of the piezo-impedance

To better understand the frequency dependence of the PZR and the PZC an extension of Kassing's model to include stress is required, and this is the achieved by assuming a stress dependence of ω_e and ω_c. The justification for this assumption is as follows.

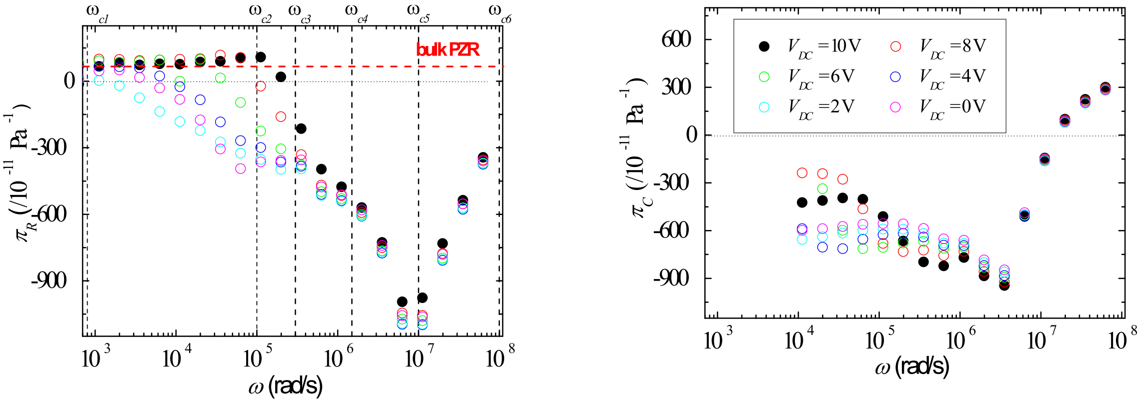

(a) Piezo-resistance (PZR) as a function of frequency.

(b) Piezo-capacitance (PZC) as a function of frequency.

Fig. 4.4 (a) PZR and (b) PZC as a function of ω for several values of V_{DC} (labeled in (b)) obtained for an applied tensile stress of 25 MPa parallel to the $\langle 110 \rangle$ crystal direction. The sign and magnitude of these coefficients is to be compared with π-bulk (red, dashed line in (a)).

The principal effect of mechanical stress in solids is to shift electronic energy levels [16]; the stress-induced effective mass change giving rise to bulk PZR of $p-$type silicon discussed in section 2.2 is due, for example, to shifts in the heavy- and light-hole valence band energies [17, 51]. Consider for simplicity only the case of hole capture and emission (see expression in Eq. (2.66) and 2.67) in the simplified version of the SRH model used by Kassing [74, 79]. The equilibrium trapped hole density p_{t0} and the hole concentration obtained when Fermi level is equal to the trap energy ($E_F = E_T$) p_1 can be expressed as [72, 79]:

$$p_{t0} = N_t exp(-\frac{E_F - E_T}{k_B T}) \tag{4.1}$$

and

$$p_1 = N_v exp(-\frac{E_t - E_V}{k_B T}) \tag{4.2}$$

where N_t and N_v are the density of traps and the effective density of states in the valence band respectively. If E_T depends on stress, then so to does p_{t0} and p_1. Most importantly, ω_c *and* ω_e *may therefore be related to stress*. We discuss the piezo-response here in two limits:

1. In the steady-state ($\omega \ll \omega_c$)

2. In non-steady-state ($\omega \geq \omega_c$)

The PZR π-coefficient measured using steady DC techniques (black dots) compared with that obtained at the lowest frequencies ($\omega \approx 1000\ rad/s$) with impedance spectroscopy (red dots) are shown in Fig. 4.5. V_{DC} varies between 0 and 10 V. The good agreement between the two approaches not only increases confidence in the impedance spectroscopy piezo-response measurements but reinforces the notion that at low frequencies the FD-devices are indeed in the steady-state limit. Moreover, in this limit the bulk PZR is measured. Another interesting point is a clear voltage dependence of the PZR, as can be seen from Fig. 4.5. This however is relatively weak compared to that in the defect engineered samples discussed in Chapter 6.

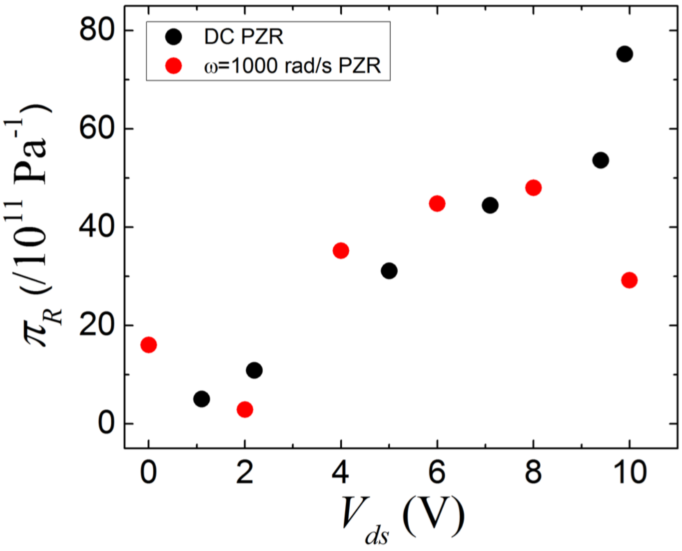

Fig. 4.5 The PZR π-coefficient measured using DC techniques (black dots) compared with that obtained at lowest frequencies ($\omega \approx 1000\ rad/s$) with impedance spectroscopy (red dots).

4.4.1 Steady-state piezo-response in the space charge limit

The conductance in steady-state is approximately given by Eq. (2.71) which is reproduced here for convenience:

$$G(0) \approx \frac{\omega_e}{\omega_c} G_g = \theta G_g. \tag{4.3}$$

The steady-state PZR measured at low frequencies may therefore arise from either stress-induced changes to G_g or to the ratio ω_e/ω_c. The geometric conductance is proportional to the mobility and should therefore have a stress dependence equivalent to the usual bulk PZR.

The fact that the steady-state PZR is close to the bulk value therefore implies that the ratio ω_e/ω_c appearing in Eq. (4.3) is independent of stress i.e. that

$$\pi_R = \frac{d(\theta G_g)}{dX}\frac{1}{\theta G_g} = \frac{1}{\omega_e}\frac{d\omega_e}{dX} - \frac{1}{\omega_c}\frac{d\omega_c}{dX} + \pi_{bulk} \tag{4.4}$$

where the value of π_{bulk} is the longitudinal PZR shown in Table 2.2 measured by Smith for $p-$type bulk silicon, and

$$\frac{1}{\omega_e}\frac{d\omega_e}{dX} = \frac{1}{\omega_c}\frac{d\omega_c}{dX}. \tag{4.5}$$

Using the zero-stress values of ω_e and ω_c obtained from measurements of G_0 and C_0 and given in Table 4.1, Eq. (4.5) can be used to establish the relative values of $d\omega_c/dX$ and $d\omega_e/dX$ to be used in the stress-dependent version of Kassing's model.

To understand physically why the ratio ω_e/ω_c is independent of stress, consider the simplified SRH expressions given in Eqs. (2.64) and (2.65). It can be shown [74] that for $N_T \gg p_{t0}$, and for $\omega_e \ll \omega_c$ (i.e. for fast traps)

$$\frac{\omega_e}{\omega_c} \approx \frac{p_0}{p_{t0}}. \tag{4.6}$$

Using the equilibrium statistics, Eq. (4.1) and $p_0 = N_V exp(-(E_F - E_V)/k_B T)$, we then have

$$\frac{\omega_e}{\omega_c} \approx \frac{1}{1 + \frac{N_T}{N_V} exp(\frac{E_T - E_V}{k_B T})}. \tag{4.7}$$

For deep traps $(E_T - E_V) \gg k_B T$, and for N_T not too small compared to N_V then

$$\frac{\omega_e}{\omega_c} \propto exp[-(E_T - E_V)/k_B T]. \tag{4.8}$$

By combining Eq. (4.8) and Eq. (4.5), the following relation can be obtained:

$$\frac{dE_V}{dX} = \frac{dE_T}{dX}. \tag{4.9}$$

This result indicates that if the stress-induced shifts in the valence band edge and the trap energies are equal, then the steady-state PZR will not have a component due to stress-induced changes in the trapping and emission rates. Rather it will be given by the usual bulk PZR as observed here.

4.4.2 Non-steady-state piezo-response in the space charge limit

In the high frequency range, $\omega \gg \omega_c$, where injected holes remain in the valence band during the voltage period and the device behaves as if traps were absent. Any stress-induced changes to ω_c and ω_e are therefore irrelevant in this limit, and a relatively small PZR comparable to the bulk $p-$type value is expected. The measurement apparatus used here is not able to reach this frequency regime, although a significant drop in the PZR is observed at the highest frequencies in Fig. 4.5(a).

In the intermediate range, $\omega \approx \omega_c$, only partial relaxation of the non-equilibrium injected charge from the bands to the traps occurs, and any stress-induced change to ω_c and ω_e may result in large relative changes to the fraction of this charge which remains in the band during a voltage cycle. In addition to the giant, anomalous PZR, an observed rapid variation of the PZC is also due to stress-induced changes to the charge capture dynamics at fast traps (see discussion in the next section). Thus, apart from the stress-induced change in the carrier mobilities, there is an additional change in the non-equilibrium charge carrier densities present in the bands. This is a purely *non-steady-state phenomena* and is fundamentally different from stress-induced changes to the equilibrium carrier density resulting from the volume density changes discussed in Chapter 2.

4.4.3 Piezo-resistance (PZR) and piezo-capacitance (PZC) simulation

According to the discussion above, the PZR and PZC are able to be simulated by using Kassing's model. The selected traps for the PZR and PZC simulation via the Kassing's model should be identical to those used in the simulation of G_0 and C_0 (see parameters in Table 4.1). In order to make the simulation as simple as possible, two assumptions need to be claimed here:

1. Since the applied stress is small ($\sim 25\ MPa$) there is no creation of new traps, such that the relative trap densities (i.e. the weight appearing in Table 4.1) are independent of stress.

2. A linear variation with stress of ω_c, ω_e and T will be used here. The relative variation of T is assumed to be equal to that of the carrier mobility due to $T = d/v = \frac{1}{\mu_p}\frac{d}{E}$, where d is the distance between the two electrodes and μ_p is the hole mobility. $dT/dX = -\frac{1}{\mu_p^2}\frac{d\mu_p}{dX}\frac{d}{E} = -\pi_{bulk}\frac{1}{\mu_p}\frac{d}{E}$. All these parameters are known, thus for $V_{DC} = 10\ V$, $dT/dX = -1.2 \times 10^{-18}\ s/Pa$. This variation will be common to all traps since it is a band property. In contrast, the variations of ω_c and ω_e with stress are individual for each trap.

In addition, several important points should be mentioned here as well:

- The strains resulting from the applied stress are less than 10^{-4} (i.e. far smaller than the measured relative conductance and capacitance changes which are of the order of 10^{-2} to 10^{-1}). Stress-induced geometry changes to G_g and C_g may therefore be considered to be negligibly small.
- The traps used here are exactly same as those used in Table 4.1 and presented by the same color compare to Fig. 4.3.
- The PZR and PZC at $V_{DC} = 10\ V$ is modeled in detail.
- The stress-dependence of ω_c and ω_e for each trap type is chosen in order that ω_e/ω_c be stress-independent according to the constraint given by Eq. (4.5), and the results are given in Table 4.2.

Considering the expression for the PZR $\pi-$coefficient in Eq. (2.4), for the six traps used in the model we have:

$$\begin{aligned}\pi_R &= \frac{1}{G_{TOT}}\frac{dG_{TOT}}{dX} \\ &= \frac{1}{G_1+G_2+G_3+G_4+G_5+G_6}\left(\frac{dG_1}{dX}+\frac{dG_2}{dX}+\frac{dG_3}{dX}+\frac{dG_4}{dX}+\frac{dG_5}{dX}+\frac{dG_6}{dX}\right)\end{aligned} \tag{4.10}$$

where G_1 to G_6 are the estimated conductances based on Kassing's model as discussed in section 4.3. The overall PZR $\pi-$coefficient is obtained by Eq. (4.10) according to Kassing's model, and is presented by the black curve in Fig. 4.6(a). Each of the coloured curves (orange, red, green, purple, brown and cyan) corresponds to the six PZR components estimated from $\frac{1}{\sum_{i=1}^{6} G_i}\frac{dG_j}{dX}$ for $j \in \{1,...,6\}$. The PZR simulation is well matched to the data measured at $V_{DC} = 10\ V$, and the parameters we used to simulate these curves are shown in Table 4.2. The six traps used here are exactly the same as those used in Table 4.1 to simulate G_0 and C_0.

The PZC is another phenomenon revealed by impedance spectroscopy which is not accessible using DC methods. Unlike the steady-state PZR, the steady-state PZC is large, with $\pi_C \approx -600 \times 10^{-11}\ Pa^{-1}$ at $V_{DC} = 10\ V$. At higher frequencies it reaches approximately $\pi_C \approx -900 \times 10^{-11}\ Pa^{-1}$ before changing sign at the highest frequencies. In Kassing's model once the frequency dependence of G_0, C_0 and π_R are simulated there are no longer any free parameters available to determine the PZC; it must be consistent with the parameter values shown in Tables 4.1 and 4.2 used to model the PZR. The capacitance is given by a ratio $\Delta Q/\Delta V$, where ΔQ is the incremental change in the charge stored in the FD device occuring

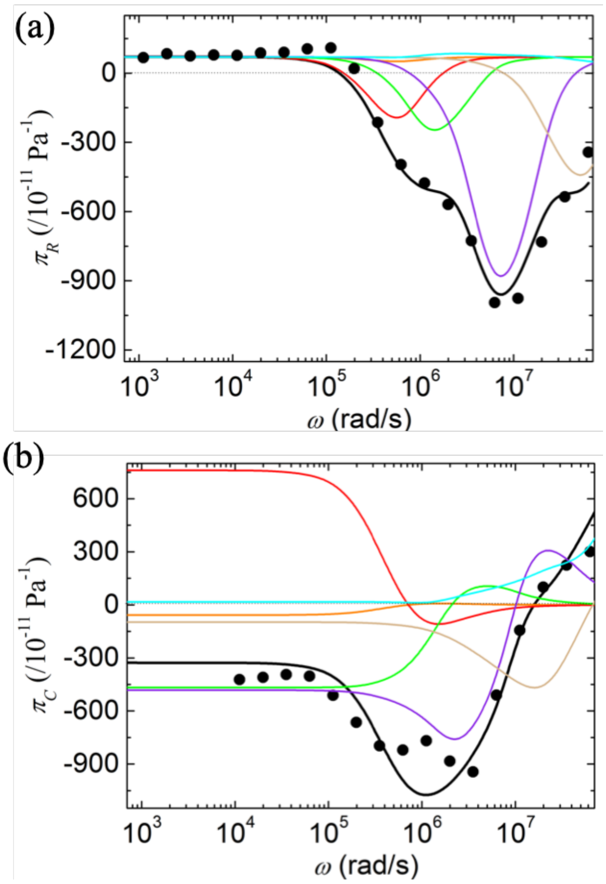

Fig. 4.6 Simultaneous modelling of piezo-response data (black dots) obtained as a function of frequency for $V_{DC} = 10\ V$. The piezo-response of the six individual trap types used to model G_0 and C_0 in Fig. 4.3 are represented by the coloured curves (orange, red, green, purple, brown and cyan). The overall piezo-response is shown as black curves.

Table 4.2 The stress-dependence of the fitting parameters used with Kassing's model [74] to calculate the ω-dependence of the PZR and the PZC for $V_{DC} = 10\ V$ in Fig. 4.6(a)and Fig. 4.6(b) respectively. The values in the last two columns are consistent with the values of ω_e and ω_c given in Table 4.1 and the constraint given by Eq. (4.5).

Trap number	**Line color in 4.6**	$d\omega_c/dX$ $(rad/s/Pa)$	$d\omega_e/dX$ $(rad/s/Pa)$
1	orange	-10^{-5}	-1.25×10^{-4}
2	red	-7.74×10^{-3}	-7.74×10^{-6}
3	green	-2.25×10^{-3}	-8.5×10^{-7}
4	purple	-4.75×10^{-2}	-1.61×10^{-4}
5	brown	-0.12	-1.2×10^{-4}
6	cyan	-1	10^{-3}

due to an incremental change in the potential difference from source to drain, ΔV. Total PZC curves shown in Fig. 4.6(b) for $V_{DC} = 10\ V$ can however be done with an arbitrary sign associated with each curve in order to account for the electron- or hole-like nature of the traps as follows.

Since the applied stress modifies the density of trapped charge according to the trapping dynamics arguments given above, this results in a change in the capacitance. The sign of the trapped charge will therefore determine the sign of the capacitance change with stress. If the trap is an electron trap, a stress induced reduction in the capture rate (see Table 4.2) will reduce the average density of trapped electrons resulting in a net positive change in the total trapped charge (and therefore an increase in the capacitance). According to the definition of π_C in Eq. (3.5) this will yield a negative PZC coefficient. The opposite will be true of hole traps. Thus the individual PZC curves calculated using the parameters in Tables 4.1 and 4.2 must be multiplied either by a factor of -1 for hole traps or +1 for electron traps. In Fig. 4.6(b) the red (trap type number 2) and cyan (trap type number 6) curves have been multiplied by -1 and therefore nominally correspond to hole traps. The other four traps are therefore considered to be electron traps. If the fast traps involved here are the intrinsic Pb_0 interface defects (as the symmetry of the piezo-response discussed in Section 4.6 suggests) this would be consistent with the amphoteric nature of such traps [102, 103]. The resulting PZC sum yields an overall calculated π_C at $V_{DC} = 10\ V$ that is well matched to the experimental curve as shown in Fig. 4.6(b). The ability to *simultaneously* match all four experimental curves (G_0, C_0, PZR and PZC) in Fig. 4.3 and Fig. 4.6 with a single set of parameter values is strong evidence that the giant, anomalous PZR and the novel PZC are both due to modifications of the capture and emission dynamics of fast traps in the space charge limit.

In addition, by using measured G_0, C_0, PZR and PZC data in Eq. (3.6), the amplitude and phase of π_Z can be presented as shown in Fig. 4.7 for $V_{DC} = 10\ V$. At low and high frequency π_Z is dominated by the PZR. It is imaginary at the highest frequencies, real at the peak piezo-response, and real at low frequencies (see gray boxes and labels). This result again emphasizes that in steady-state, the overall piezo-response is just the bulk PZR due to stress-induced charge carrier mobility changes. At intermediate frequencies however, π_Z is dominated by the PZC and switches from an imaginary to a real response with increasing frequency. This result is specific only to the devices studied here. With appropriate parameter values in Eq. (3.6), a FD-SOI device in which π_Z is dominated either by the PZC or by the PZR at some a desired frequency is conceivable. For the future potential application of strain sensor, the value of π_Z is very important, because it counts for the sensitivity of sensor. Therefore, it is necessary to understand how π_R and π_C play role in in π_Z.

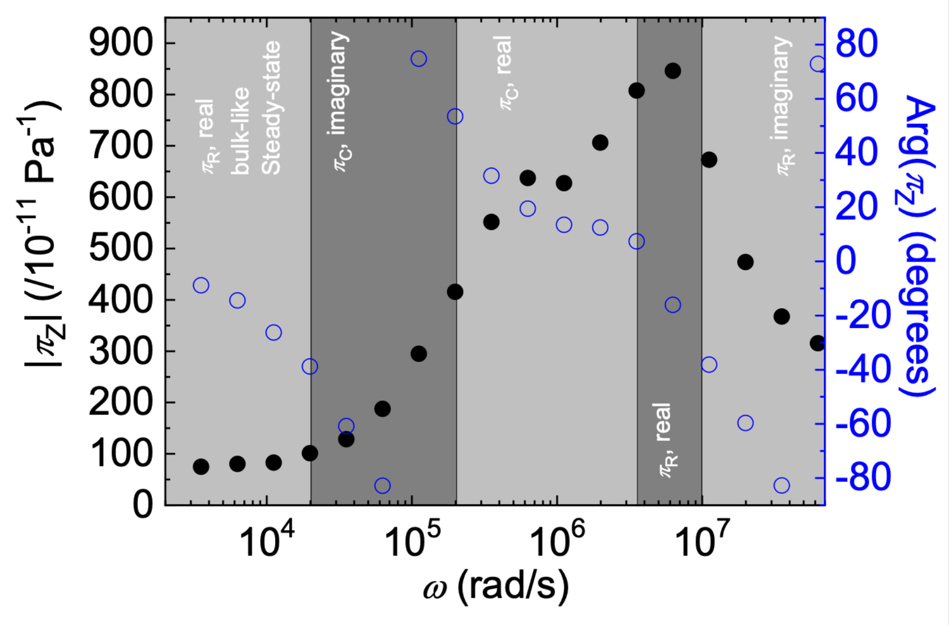

Fig. 4.7 The amplitude (black) and phase (blue) of π_Z at $V_{DC} = 10\ V$ calculated using Eq. (3.6) from the data presented earlier. π_Z can be real or imaginary, and may be dominated by either the PZR or the PZC depending on ω (see labels in gray boxes). In steady-state the overall piezo-response is close to the usual, bulk PZR given by π_{bulk}.

The interpretation of the giant, anomalous piezo-response as being due to stress-induced modifications of the fast trapping dynamics in the SCLC regime is further reinforced by the observation of a strong, systematic voltage dependence of the PZR below $\approx 6 \times 10^5\ rad/s$ as seen in Fig. 4.4(a), as well as the symmetry of the piezo-response in stress. These points will be discussed in the next two sections.

4.5 Voltage dependence of the piezo-impedance at fixed tensile stress

In Fig. 4.4(a) (colored circles), it's easy to observe a remarkable systematic variation in the PZR as a function of bias around $\omega = 6 \times 10^5\ rad/s$, while this variation becomes weaker at high frequency regime. As is well-known, trap emission rates can be related to applied electrical field, for example due to the Poole-Frenkel effect or via phonon assisted tunneling from the trap [83] (see section 2.4). In the latter case as the electrical field increases, the emission rate, ω_e, increases exponentially with the square of the electric-field strength according to Eq. (2.77):

$$\frac{\omega_e(\mathscr{E})}{\omega_e(0)} = exp(\frac{\mathscr{E}^2}{\mathscr{E}_c^2}), \tag{4.11}$$

where $\mathscr{E}_c$ is characteristic field strength, given by:

$$\mathscr{E}_c = \sqrt{\frac{3m^*\hbar}{e^2\tau^3}}, \tag{4.12}$$

Eq. (2.77) can be written as:

$$ln(\beta) = ln(\frac{\omega_e(\mathscr{E})}{\omega_e(0)}) = \frac{\mathscr{E}^2}{\mathscr{E}_c^2}. \tag{4.13}$$

As $\mathscr{E}_c$ is independent of electrical field, therefore $\mathscr{E}^2$ is linearly dependent on $ln(\beta)$. It should be noted here that the pre-factor of emission rate, β, is the relative change of emission rate induced by electrical field, and is identical for all six traps. In addition, if β is independent of stress, then

$$\frac{d\omega_e(\mathscr{E})}{dX} = \frac{d\beta\omega_e(0)}{dX} = \frac{\beta d\omega_e(0)}{dX}. \tag{4.14}$$

Since voltage is expected to principally affect the emission rates, the low frequency PZR rather than the PZC is the relevant quantity to study because in the limit $\omega \to 0$, according to Eq. (2.71) and Eq. (2.72), $G_0 \to \omega_e G_g/\omega_c$ whereas the capacitance, $C_0 \to C_g/(\omega_c T)$, is independent of ω_e. This also explains the obvious V_{DC} dependent conductance shown in Fig. (4.2)(a). The pre-factor β for each value of V_{DC} is chosen to best match the voltage dependence of the lowest frequency PZR peak (dashed lines) as shown for four V_{DC} values in Fig. 4.8(a) since it is this peak which is most sensitive to V_{DC}. The resulting overall PZR is shown as solid lines. The colours correspond to those of the data (circles) shown in Fig. 4.4. This simple procedure is able to capture not only the voltage dependence of the lowest frequency PZR peak, but also the relative insensitivity of the higher frequency PZR to changes in V_{DC}, despite the fact that the emission rates of the higher capture rate traps have also been multiplied by β. As can be seen from the values of ω_c and ω_e in Table 4.1, the reason for this is that the trap with the lowest capture rate (orange lines in Fig. 4.6) transitions from being a fast trap ($\omega_e < \omega_c$) at $V_{DC} = 0\ V$ to a slow trap ($\omega_e > \omega_c$) at higher absolute voltages. All the other traps, despite a voltage dependent variation in their emission rates, remain fast traps over the experimentally tested range of V_{DC}. Thus it becomes clear that slow traps do not significantly contribute to the giant, anomalous piezoresponse (i.e.

the amplitude of the orange peak is small in 4.6(a) at $V_{DC} = 10\ V$). It is rather the stress dependence of the trapping dynamics at fast traps which determine the giant, anomalous piezo-response.

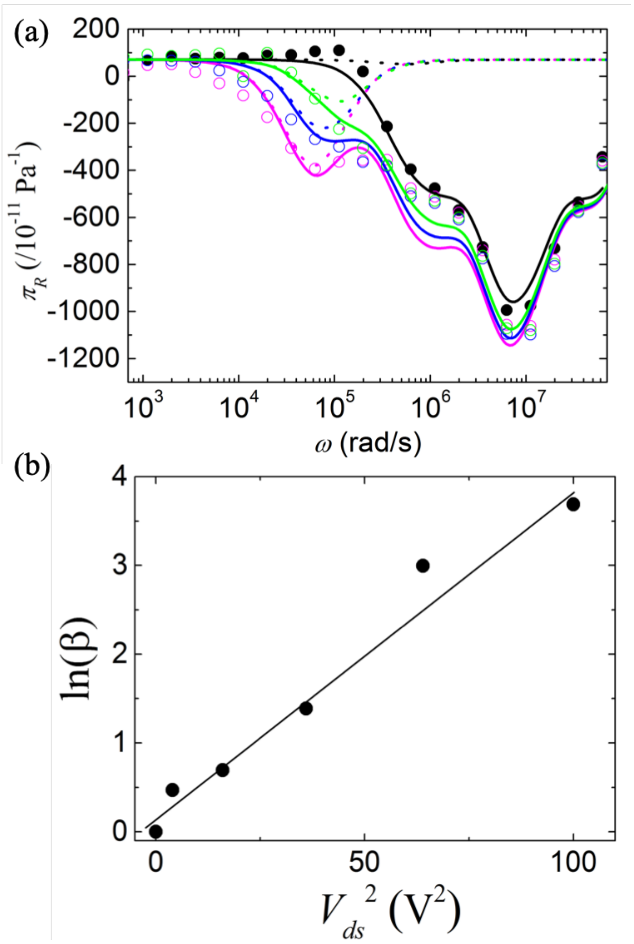

Fig. 4.8 (a) V_{DC} dependence of the PZR with the data (circles) shown according to the colour scheme of Fig. 4.4(a). An applied voltage increases all trap emission rates by a voltage dependent pre-factor β. This preferentially increases the PZR of the slow trap (orange curves in 4.6(a)) at low measurement frequencies. The individual PZR peak of this trap is shown (dotted lines) along with the overall calculated PZR (solid lines). The values of β are chosen so as to best match the low frequency PZR, and the resulting dependence of $ln(\beta)$ on V_{DC}^2 shown in (b) suggests that the voltage dependence of the emission rates results from phonon-assisted tunneling from the trap.

Returning to the voltage dependence of the pre-factor β used to describe the electric field dependence of ω_e, the linear variation of $log(\beta)$ (shown in Fig. 4.8(b)) favours an interpretation in which the increase in trap emission rates with increasing applied voltages is a result of phonon-assisted tunneling from the trap [83].

Table 4.3 Voltage dependent pre-factors, β, used to account for the increase in all trap emission rates with increasing applied voltage.

$V_{DC}(V)$	β	$ln(\beta)$
-10	40	3.67
-8	20	2.99
-6	4	1.39
-4	2	0.69
-2	1.6	0.47
0	1	0

4.6 The symmetry property of relative conductance change in stress

Fig. 4.9 shows the relative stress-induced changes in G and C at two measurement frequencies, $\omega = 1.5 \times 10^4\ rad/s$ (open circles) and $\omega = 1.5 \times 10^7\ rad/s$ (filled circles) for $V_{DC} = 10\ V$. Negative values of X correspond to compression, while positive values of X correspond to tension. The slope of these curves is proportional to π_R and π_C according to Eq. (3.4) and Eq. (3.5). At low frequency, $-\Delta G/G_0$ is approximately linear (i.e. odd) in stress, meaning that the PZR $\pi-$coefficient has same sign for tensile and compressive stress as would be expected for the steady-state, bulk $p-$type silicon PZR [17]. The stress symmetry of the PZC at low frequency is not clear, partly because capacitance measurements are difficult at such frequencies. Unlike the PZR however, it is not clearly odd. The high frequency PZR and PZC are both even (but asymmetric) in stress. This symmetry has been reported elsewhere, including in gate leakage currents [104] and in flash EEPROMs [105]. For example, the stress-induced changes in the leakage current of a $p-$type silicon metal-oxide-semiconductor capacitor is even with respect to a $\langle 110 \rangle$ crystal direction stress (see black line in Fig. 4.10(a)). This was attributed to a large number of interfacial $Pb-$like defects that are created after electric damage, and that are responsible for trap-assisted tunneling currents across the oxide layer. The structure of the Pb_0-centre is shown in Fig. 4.10(b), on a (001) silicon surface. The symmetry of the response seen in Fig. 4.9 therefore provides tentative evidence that these defects are the electro-mechanically active fast traps responsible for the non-steady-state GPZR. As the surface of the sample is disordered, the Si/SiO_2 interface is not atomically flat, so the dangling bonds may point ($Pb-$like defects) at different direction, they are not identical, each of them is slightly different, this explains why we have to use multiple traps to simulated the impedance spectroscopy results. Note that, these symmetry arguments are based on transport measurements only, and that a direct spectroscopic measurement of the stress symmetry of Si/SiO_2 interface defects has not been made. This is addressed in the following chapter.

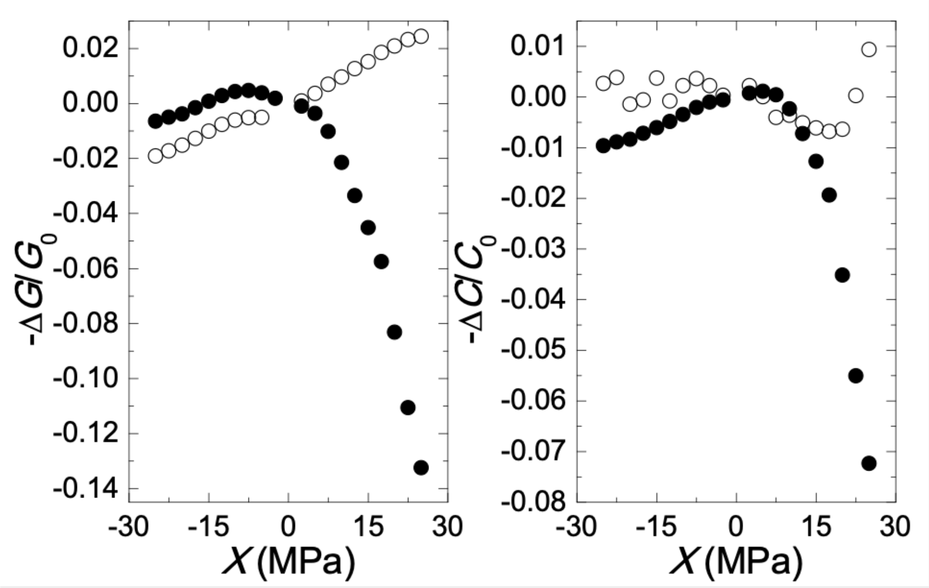

Fig. 4.9 Stress symmetry of the PZR and the PZC at $\omega = 1.5 \times 10^4$ rad/s (open circles) and at $\omega = 1.5 \times 10^7$ rad/s (filled circles) for $V_{DC} = 10\ V$. An odd symmetry is consistent with the usual bulk PZR, while an even symmetry can be attributed to the electro-mechanical response of intrinsic Pb_0-centres at the silicon/oxide interface.

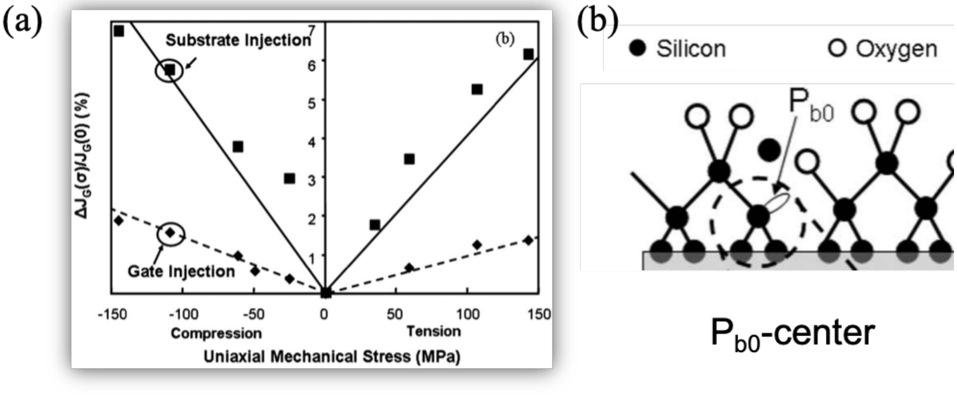

Fig. 4.10 (a)The stress-induced changes in the leakage current of a $p-$type silicon metal-oxide-semiconductor capacitor is even in the $\langle 110 \rangle$ crystal direction stress. (b) The Pb_0-centre on the (001) silicon surface with a $\langle 111 \rangle$ crystal direction dangling bond. Extracted from Ref. [104].

4.7 Small signal frequency spectroscopy of heavily doped *p*-type silicon device

The piezo-response of heavily $p-$type doped silicon device ($p = 10^{18}\ cm^{-3}$) is shown here in order to compare it with that of silicon devices in the SCLC regime. The geometry is identical to the SCLC devices shown in Fig. 3.2 and Fig. 4.1 except that the thickness of the device layer is 300 *nm* in this case, much thinner than SCLC device. In addition, according to Eq. (1.4), the depletion layer width is estimated to be about 30 *nm*, ten times thinner than thickness, so that $W \ll d$. Therefore, bulk-like π_R is expected to be observed here.

Fig. 4.11(a) shows the frequency dependence of the zero-stress conductance while Fig. 4.11(b) shows the frequency dependence of the PZR, both for $V_{DC} = 0\ V$. Black data points in Fig. 4.11 correspond to devices measured soon after fabrication. The red data points shown in the Fig. 4.11 present results measured on the same devices after a time interval of one year during which the samples were stored in air. Note that in this sample in the measured frequency range the capacitance-related quadrature component of the admittance is negligibly small compared to the real, conductance-related component. Moreover, the device shows no significant voltage dependence of either the conductance or the PZR, and for this reason C_0 and π_C are not shown here. The device is in the Ohmic regime as indicated by the linear I-V characteristic (see inset of Fig. 4.11(b)), and thus the equilibrium charge carriers dominate transport. Even though surface states exist their density is negligible compared to that of equilibrium charge carriers in the band. G shows almost no dependence on the frequency as would be expected for a purely resistive device (see Eq. (2.1)). Note well the scale of the conductance axis compared to the frequency-dependence of the conductance in the SCLC devices. This frequency independence is coupled with an essentially frequency-independent PZR where the measured π-coefficient is close to the usual bulk value, except at the highest frequencies where it drops to zero and becomes slightly negative. The reason for this variation is not clear, but it is never-the-less small compared to the variation in the PZR with frequency of the SCLC devices that are sensitive to fast trapping dynamics. In heavily doped, Ohmic device therefore, the conductance and PZR over most of the measured frequency range are the same as those obtained from a DC measurement of the bulk PZR effect.

Another important point that can be seen from Fig. 4.11 is that the contacts of device are not the reason for giant, anomalous piezo-response in the SCLC devices. This is because the fabrication procedure for the Ohmic contacts is identical for the heavily doped devices and the SCLC devices. The absence of unusual PZR in the heavily doped devices shows that the

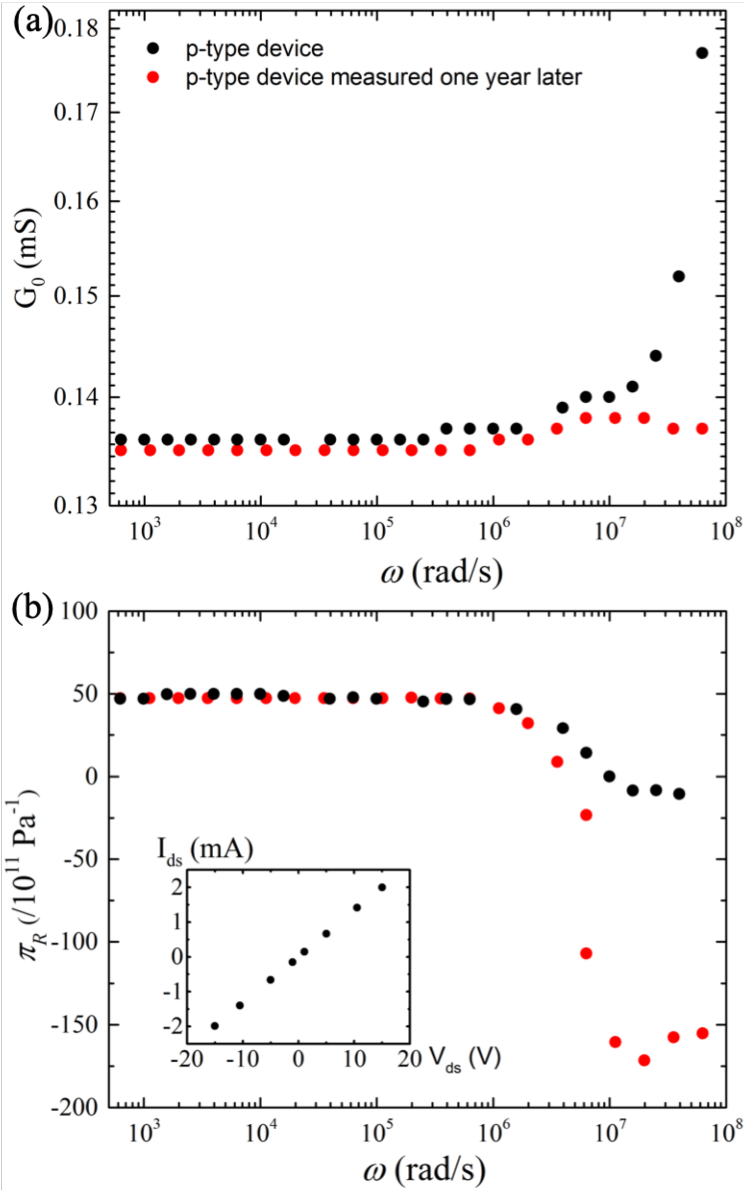

Fig. 4.11 (a) Frequency-dependent conductance and (b) piezoresistance of heavily doped $p-$type silicon device. The results measured immediately just after sample fabricated is represented by black data points. This doped sample is in the Ohmic regime due to linear I-V characteristic using DC measurement techniques as shown inset of (b).

piezo-response of the SCLC devices is due to a phenomenon occurring in the silicon and not at the contacts.

4.8 Conclusion

In this chapter, the steady-state piezo-response of the SCLC in natively-oxidized non-intentionally-doped, $p-$type silicon is found to be just the usual bulk PZR using impedance spectroscopy techniques. At frequencies much lower than the characteristic trapping rates, impedance spectroscopy reveals the steady-state transport properties of the SCLC. In this limit the PZR is just that of bulk silicon as described in section 2.2. This confirms the large number of reports of bulk-like in nano-silicon, depleted or not, even in the presence of charge traps whose trapping and emission rates are stress dependent. Arguments based on a combination of the classic Shockley-Read-Hall model and Kassing's model show that this can be the case if the stress dependence of the trap energy and the (valence) band energy are similar.

Impedance spectroscopy are however shown to give access to the non-steady-state piezo-response where stress-induced variation in trapping and emission rates *do* results in giant, anomalous PZR. In addition, impedance spectroscopy yield a quadrature response that corresponds to a giant PZC. At measurement frequencies $\omega \approx \omega_c$, the PZR consists of not only the stress-induced change in the charge carrier mobilities i.e. the bulk effect, but also a significantly larger stress-induced change in the concentration of *non-equilibrium* holes injected from the Ohmic contacts. This is fundamentally different from stress-induced changes to the equilibrium charge concentrations which are negligible compared even to the mobility changes. The PZC is in some respects complementary to the PZR in that it depends on stress-induced changes to the trapped hole concentrations. The symmetry of the giant, anomalous PZR and the PZC suggest that intrinsic Pb_0 silicon/oxide interface defects are the likely candidates for the electro-mechanically active fast traps.

Chapter 5

The stress dependence of the pinned surface Fermi level at an Si/oxide interface

In Chapter 4 a model of stress-induced changes in the capture and emission rates of fast electronic traps was proposed. Experimental evidence, and in particular the even symmetry of the piezo-response under tensile and compressive mechanical stresses, suggests that the fast traps responsible for the observations are deep, intrinsic interface defects i.e. Pb_0-like defects at the (001) silicon/oxide interface. These are the same types of deep centres that are responsible for the pinning of the Fermi level at the silicon/oxide interface close to an energy E_T. To further explore the proposition that Pb_0 centres are at the origin of the giant, anomalous piezo-response, an X-ray photo-emission spectroscopy (XPS) experiment on the surface of stressed, silicon cantilevers is undertaken in this chapter. The experiment is presented in section 5.1. In section 5.2, two cantilevers whose top surfaces are stressed either in tension or in compression are described. Meanwhile, in section 5.3, the stress-induced surface Fermi level shifts and the means to measure them using X-ray photo-electron spectroscopy (XPS) mapping are introduced. In section 5.4, Raman maps and XPS maps are combined together in order to determine the stress dependence of the pinned surface Fermi energy. Interestingly an even symmetry of the pinned surface Fermi level in stress is obtained. The directly measured shifts in energy are compared with values obtained elsewhere via indirect transport measurements [104–107]. A simplified estimate of the local potential at a Pb_0 dangling bond also shows an even symmetry in stress, indicating that the observations are consistent with an interpretation based on the stress dependence of E_T for these traps.

5.1 Experimental strategy and sample holder design

The Pb_0 interface defect is postulated in Chapter 4 to be responsible for the giant, anomalous piezo-response in non-steady-state. Moreover, Pb_0-like silicon dangling bonds at (001)-oriented Si/SiO_2 interfaces are the majority interface states [108, 109] and can therefore also be responsible for surface Fermi level pinning near the middle of band gap [110–112]. It should then be possible, via an XPS measurement, to directly measure stress-induced changes to the surface Fermi level that may be related to the stress dependence of E_T of the Pb_0-centres. The silicon cantilever used here are already presented in section 3.1 and the experimental details will be discussed in this section.

5.1.1 Experimental strategy

Stress-induced surface Fermi level shift measurement

XPS is an ultra sensitive surface technique which permits the detection of the silicon surface Fermi level position relative to its value at a contact held at some reference potential. It does this by measuring the energy shift in the silicon core level states using high resolution XPS [113]. The experimental schematic for XPS is shown in Fig. 5.1(a) for a $p-$type silicon sample. A beam of monochromatic X-ray photons is emitted from an X-ray source of photon energy $h\nu$, and incident on a silicon surface at an angle α. These photons are able to ionize the silicon atoms resulting in the escape of electrons from a bound state to a free state. For the silicon surface electrons have to overcome the work function, ϕ_s, to escape. This is defined as the minimum energy required for an electron to jump from the Fermi level to the vacuum level. The kinetic energy of emitted electrons, E_k is:

$$E_k = h\nu - E_B - \phi_s, \tag{5.1}$$

where E_B is the binding energy of the core electron (defined as the energy required to free electrons from their atomic orbits). The energy diagram of a $p-$type silicon is shown in Fig. 5.1(b). In Eq. (5.1), ϕ_s can be extracted by measuring the Fermi level on a metallic reference gold sample. In this way, the Fermi level of the sample and analyzer are aligned as shown in Fig. 5.1(b). The kinetic energy of photo-emitted electrons measured by the detector shown in Fig. 5.1(a) through the analyzer (E_{ka}) is related to the work function of analyzer ϕ_a. In this case, it is no longer necessary to know exactly the work function of the sample, and Eq. 5.1 can be written:

$$E_{ka} = h\nu - E_B - \phi_a. \tag{5.2}$$

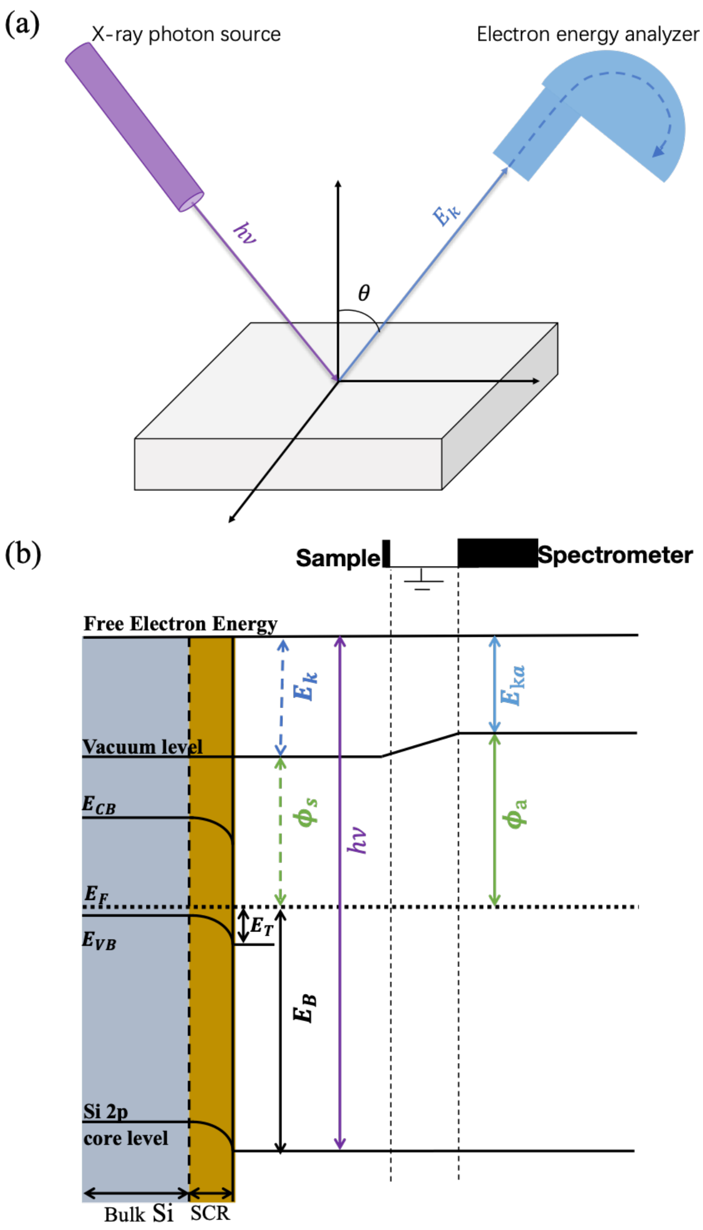

Fig. 5.1 (a) Schematic of the basic XPS measurement geometry. An X-ray beam (purple solid arrow) of photon energy $h\nu$ is incident on the surface of the sample and photo-excited electrons (blue solid arrow) with sufficient energy to overcome the work function are emitted into vacuum with a kinetic energy E_k. The kinetic energy spectrum is measured with a hemispherical analyzer. (b) Schematic representation of the silicon energy levels when the sample and the analyzer are connected and grounded in order to align the Fermi levels.

Electronic energy band bending occurs at the silicon surface due to the compensation of surface charge by opposite charges in the bulk silicon (see gray area in the Fig. 5.1(b)). This band bending results in a so-called space charge layer (SCL) or depletion layer shown in yellow in Fig. 5.1(b) [36]. The surface state energies E_T refer to the energy between the Fermi level E_F and the valance band minimum E_{VBM}. The *Si* 2p core levels also bend in the SCL and the energy between the core levels and the E_{VBM} is constant [114].

In Eq. (5.2), the X-ray photon energy $h\nu$, the photo-electron kinetic energy E_{ka} and the analyzer work function ϕ_a are known parameters, and it is then easy to estimate the core electron binding energy E_B from a measurement of the photo-electron kinetic energy. The XPS spectrum is then presented as the distribution of electrons as a function of either the kinetic energy (E_{ka}) or the binding energy (E_B). The peak in the XPS spectrum corresponds to the energy level where electrons are most likely to appear, i.e., the energy of atomic orbits. Generally speaking, the thickness of the sample probed by XPS is less than ten *nm* and is related to the inelastic mean free path (IMFP) of photo-exited electrons. The IMFP, defined as λ, describes the average distance that an excited electron can move before it undergoes an inelastic loss. The probability for an excited electron to move a distance d in the medium without inelastic loss is:

$$P(d) = exp(-\frac{d}{\lambda}). \tag{5.3}$$

The IMFP depends phenomenologically on the kinetic energy as shown in the following equation [115] and in Fig. 5.2:

$$\lambda = \frac{143}{{E_k}^2} + 0.054\sqrt{E_k}. \tag{5.4}$$

For the approximate electron kinetic energies measured in this work ($\approx$ 100 *eV*, see section below) $\lambda \approx 0.6$ *nm*. Thus XPS really detects the surface of the silicon sample at depths much smaller then the SCL width, which for these samples is estimated to be of the order of 30 *nm*.

If E_T shifts with stress as the discussion in Chapter 4 indicates, then according to Fig. 5.3 this shift can be detected as a shift in the *Si* 2p core level peaks with stress. This is the principle motivation for this work. Explicitly:

$$\frac{dE_B}{dX} = \frac{dE_T}{dX} = -\frac{dE_k}{dX}, \tag{5.5}$$

since the photon energy in Eq. (5.2) is constant.

The samples studied here via XPS are statically deflected (fixed-free) cantilevers whose surface stress varies as a function of position. By scanning the X-ray beam over the surface it is therefore possible to obtain the core level peak position for different stress values in a single static object.

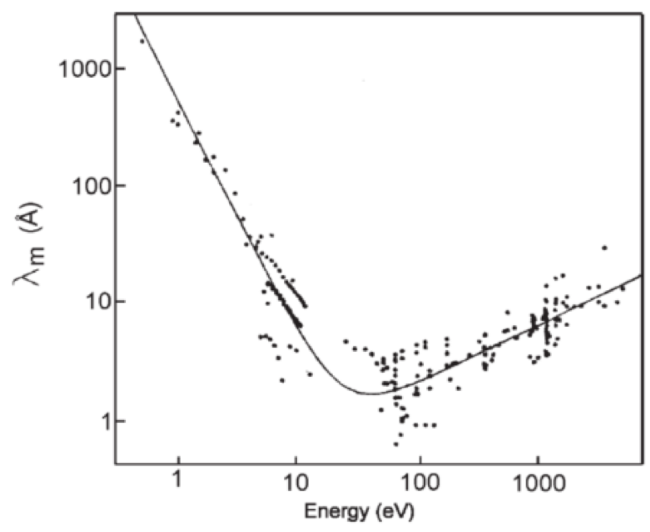

Fig. 5.2 The inelastic mean free path (IMFP), λ, as a function of kinetic energy for various solid elements. Extracted from Ref. [115].

5.1.2 Sample holder design

The sample holders were specifically developed for the TEMPO beam line at Soleil synchrotron and are completely UHV compatible. They are designed so that the long, rectangle sample seen in Fig. 3.3 can be solidly clamped at one end (to be known as the fixed end as shown in Fig. 5.4(a)). The other end is free to move (the free end as labeled in Fig. 5.4(a)) and a static deflection, Δz, is applied to the free end using an adjustable screw. As seen in Fig. 5.4(b), if Δz is positive the top surface (in red) is compressively stressed whereas Δz is negative the top surface is tensile stressed (see Fig. 5.4(c)). By virtue of the orientation in which the cantilevers were cut, these are uniaxial stresses applied parallel to the $\langle 110\rangle$ crystal direction.

The stress along the top surface of the cantilever is maximum at the fixed end and zero at the free end. It varies linearly along the $y-$axis defined in Fig. 5.4(a) according to the cantilever formula [97],

$$X = \frac{F}{Z}(l-y), \tag{5.6}$$

for a free end deflection of

$$\Delta z = \frac{Fy^2(3l-y)}{6EI}. \tag{5.7}$$

The physical meaning of parameters in above equations are shown in Table. 5.1. At the

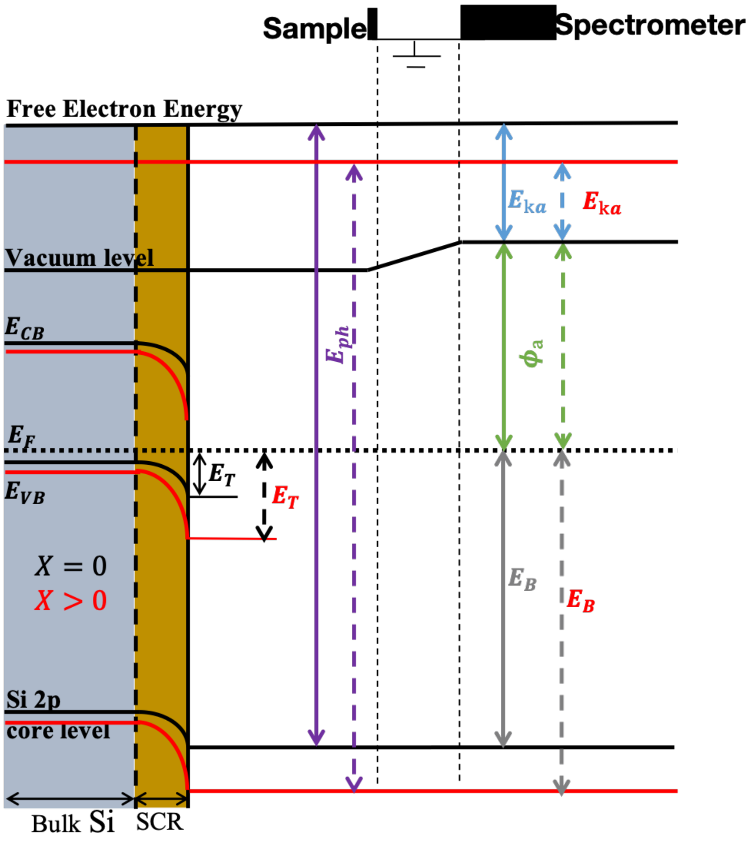

Fig. 5.3 Energy level diagram for the surface of p-type silicon showing the electronic structure in the bulk and in the space charge layer (SCL) with tensile (red) and without (black) stress.

Table 5.1 The parameters in the fixed-free cantilever model [97].

Parameter	Physical meaning	Unit
X	Stress at specific point	N/m^2 (Pa)
F	Force loaded at the end of cantilever	N
Z	Section modulus of the cross-section of cantilever = $\frac{I}{t/2}$	m^3
I	Moment of inertia of cross section	m^4
t	Thickness of cantilever	m
l	Length of cantilever	m
b	Width of cantilever	m
y	Position of cantilever in y-direction	m
Δz	Deflection of cantilever	m
E	Modulus of elasticity	N/m^2

free end when $y = l$, cantilever deflection is maximized and

$$\Delta z_{max} = \frac{Fl^3}{3EI}, \tag{5.8}$$

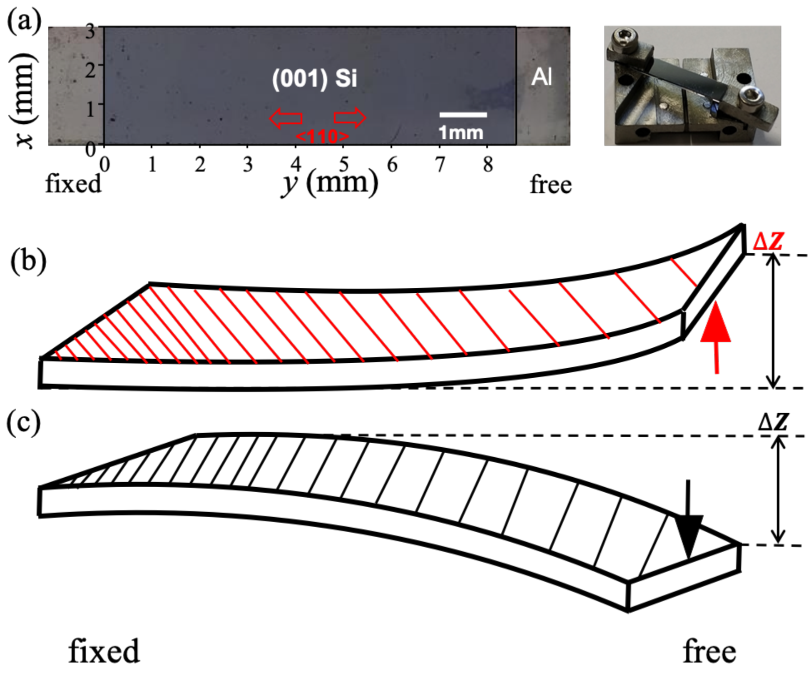

Fig. 5.4 (a) $p-$type silicon cantilevers with ohmic contacts visible at each end that make contact with the earthed sample holder shown right. The $x-$ and $y-$axes are marked in *mm* in order to locate pixel positions in the subsequent Raman and XPS maps. Using a mechanical screw to apply a force as shown in (b) and (c), the free end of the cantilever is deflected by Δz. (b) An upwards deflection yields a uniaxial, compressive stress parallel to the $\langle 110 \rangle$ crystal direction on the top surface, with a maximum at the free end. (c) A downwards deflection yields an equivalent tensile stress.

so that by substitution into Eq. (5.6), the stress distribution on the top cantilever surface is:

$$X = \frac{3Et\Delta z_{max}}{2l^2}(l-y). \tag{5.9}$$

5.1.3 Experimental set-up

Stress measurement using a micro-Raman spectrometer

The real stress as a function of position (x, y) on the cantilever surface can be estimated using micro-Raman spectroscopy [116, 117]. Raman spectroscopy is a powerful optical technique to observe inelastic photon scattering by elementary vibrational excitations (phonons) in the sample. As depicted in Fig. 5.5, after a monochromatic laser photo-excites the sample a scattering process occurs and energy is transferred between incident photon $(h\nu)$ and the atoms. As a result a scattered photon with energy of $h\nu_s$ is emitted and

$$h\nu_s = h\nu \pm h\Omega. \tag{5.10}$$

In the scattering process most photons are just elastically scattered without any energy loss to the atoms. This is known as Rayleigh scattering and corresponds to Eq. (5.10) with $h\Omega = 0$. What we care more about is inelastic scattering due to photon absorption or creation while being scattered by phonons. In this case $h\Omega \neq 0$ and the incident photon frequency is shifted. This is the well-known Raman shift which is related to the mechanical properties of the sample. If the final vibrational state of atom is higher after scattering, then the photon frequency is lowered and the sign of $h\Omega$ in Eq. (5.10) is negative. This is referred to as a Stokes shift. In contrast, if the final vibrational state of atom is lower after scattering, then the photon frequency is increased and the sign of $h\Omega$ is positive. This is referred to as an anti-Stokes shift. Using Raman spectroscopy, we are able to obtain a spectrum of the allowed Raman-active phonon modes of the sample.

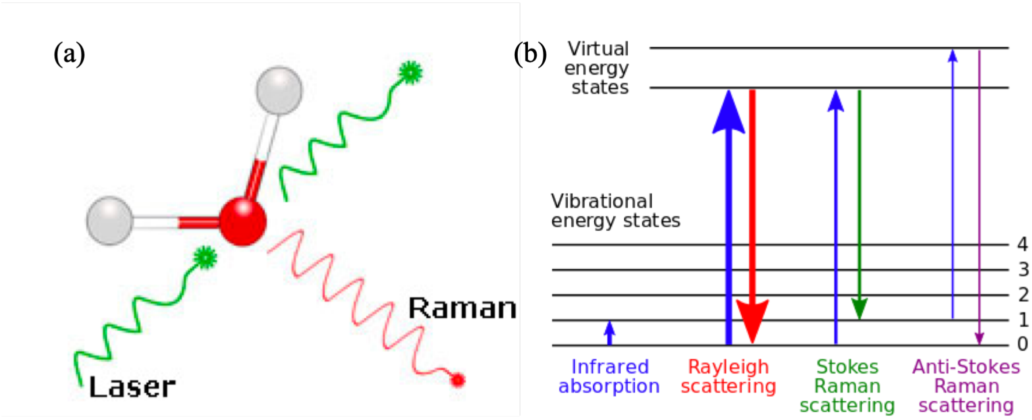

Fig. 5.5 (a) Raman and Rayleigh scattering after incident light via a atom, extracted from *www.horiba.com*. (b) Energy level diagram of different scatterings, extracted from *wikipedia.org*.

In the presence of a external mechanical stress lattice parameters change and so too does the phonon frequency [116, 117]. Each of the stress-shifted phonons has its own vibrational frequency, ν_ε which is linearly lifted in stress from its zero-stress frequency, ν_0. Therefore, a shift $\Delta\Omega = \nu_\varepsilon - \nu_0$ can be used to optically measure stress applied on the cantilever according to:

$$\Delta\Omega = -kX, \tag{5.11}$$

where k a proportionality factor and X is the uniaxial stress. Consequently, it's possible to combine the stress-induced surface band bending shift and stress distribution by measuring XPS and Raman spectroscopy map, respectively. In silicon for a uniaxial stress along the $\langle 110 \rangle$ crystal direction $k = 2 \times 10^{-9}$ [118, 119].

The Raman spectrometer used here is model of LabRAM HR Evolution manufactured by Horiba as shown in Fig. 5.6. This Raman spectrometer has blue and red laser sources with wavelength of 486 nm and 633 nm, respectively. We chose the laser source according to the different light penetration. Since the surface stress is interested in our case, obviously, the blue laser source, which has shorter penetration depth, is preferred in this experiment. The controllable and movable sample observation stage allows us to scan the surface of cantilever with constant step in the $x-$ and $y-$directions. Moreover, during the measurement, the laser beam emitted from objective will be automatically focused on the surface of cantilever by an auto-focus technique and the objective's varying position in the $z-$direction is recorded. This is in fact the relative deflection of the cantilever, Δz, due to stress. This helps to verify the surface stress estimation result from the Raman spectroscopy measurement by comparing it with the cantilever formula (see Eq. (5.9)) with a known deflection.

Fig. 5.6 Picture of the Raman spectrometer, a LabRAM HR Evolution produced by Horiba. Extracted from www.horiba.com.

Fig. 5.7 shows an example Raman spectrum of silicon on an unstressed cantilever. The characteristic longitudinal optical (LO) phonon Raman peak of silicon is 521 cm^{-1}. A stress applied on the cantilever will shift this LO phonon peak. Using a Raman map, a spectrum associated with each scanned pixel on the cantilever surface is used to obtain the stress relative to the pixels at the free end where the stress is zero (see Eq. (5.9) with $(l-y)=0$).

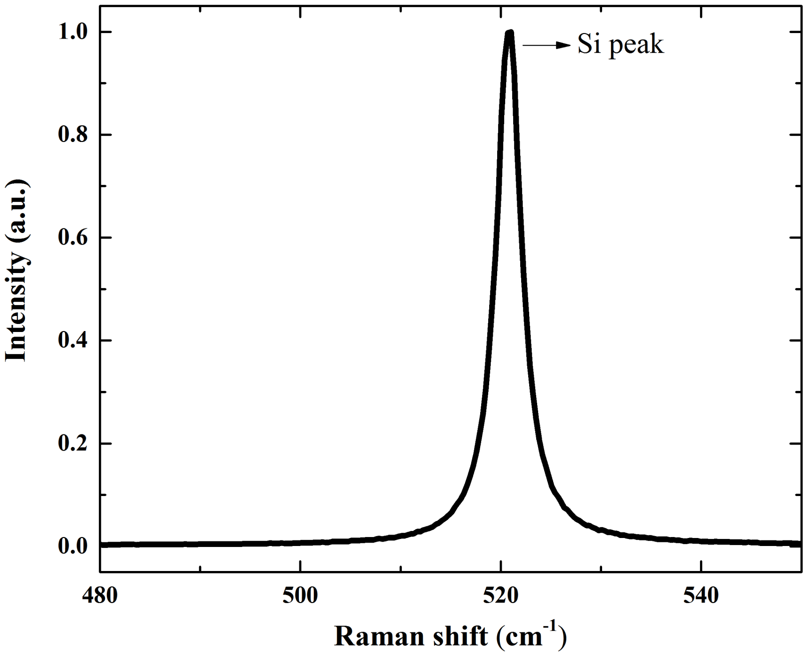

Fig. 5.7 An example Raman spectrum of silicon cantilever with zero-stress, the characteristic LO phonon Raman peak of silicon is 521 cm^{-1}.

5.2 Using Raman microscopy to map stress on statically deflected silicon cantilevers

5.2.1 Surface stress detection by Raman spectroscopy

Fig. 5.8 shows the Raman spectra of two points, one of which is located at the free end (black curve) and the other of which is located at the fixed end (red curve) of the tensile stressed cantilever. At the free end, the Raman peak is positioned at 521 cm^{-1}, and this is equivalent to the zero-stress LO phonon silicon Raman peak, proving that the stress is zero at the free end. For the Raman spectrum at the fixed end the peak is shifted by -0.46 cm^{-1} indicatng according to Eq. (5.11) a tensile stress of 230 MPa is applied at the fixed end.

To estimate the stress distribution, the surface of statically deflected cantilevers are scanned by Raman spectroscopy with a step of 0.2 mm in both the $x-$ and $y-$directions. The stress distribution is estimated by measuring stress-induced shift in the Si LO phonon Raman peak taking the Raman peak at the free end as the reference. Fig. 5.9 shows two stress maps, one for upward and one for downward deflected cantilevers respectively. The colour in the

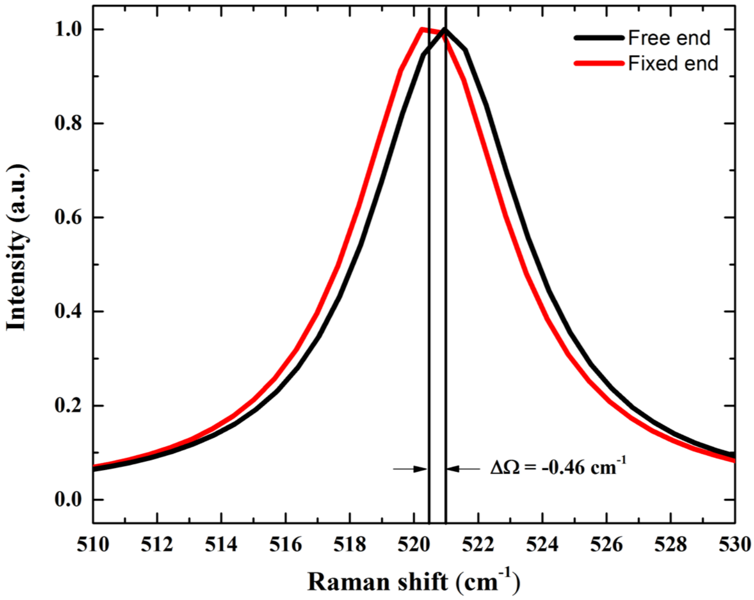

Fig. 5.8 The Raman frequency measured at the fixed (red curve) and free (black curve) ends of a tensile stressed cantilever. The stress-induced shift between the peaks is approximately -0.46 cm^{-1}, corresponding to a tensile stress at the fixed end of the cantilever of about 230 MPa [118, 119].

map presents the value of stress and the unit in the colour bar is MPa. Both compressive and tensile stress distributions (see Fig. 5.9(a) and (b)) indicate that stress varies approximately linearly in the $y-$direction decreasing in magnitude from the fixed end to the free end as expected for a fixed-free cantilever (see Eq. (5.9). Note that the dimensions of the maps are smaller than the actual cantilever size (11 $mm \times 3$ mm) especially in the tensile map. This is because only the silicon active layer counts, and it is not necessary to measure the Raman peak in the Ohmic contact regimes. In the XPS experiment that will be discussed in section 5.3, the useful scanning area is smaller than the cantilever due to unidentified contaminants on the edges of the surface. In order to facilitate compareson of the Raman and XPS maps, only the parts of the Raman maps that were successfully mapped with XPS are shown.

The maximum compressive stress is 90 MPa which is lower in magnitude than that of tensile stress, 240 MPa, because the mounting procedure in compression is more delicate than that in tension. Obviously, the stress distribution shown in Fig. 5.9 is not that of an ideal fixed-free cantilever. For example, in the case of the tensile cantilever the maximum stress appears at the bottom left corner of the fixed end, while the minimum stress appears at top right corner of the free end. This is because the clamped point at the fixed end introduces a

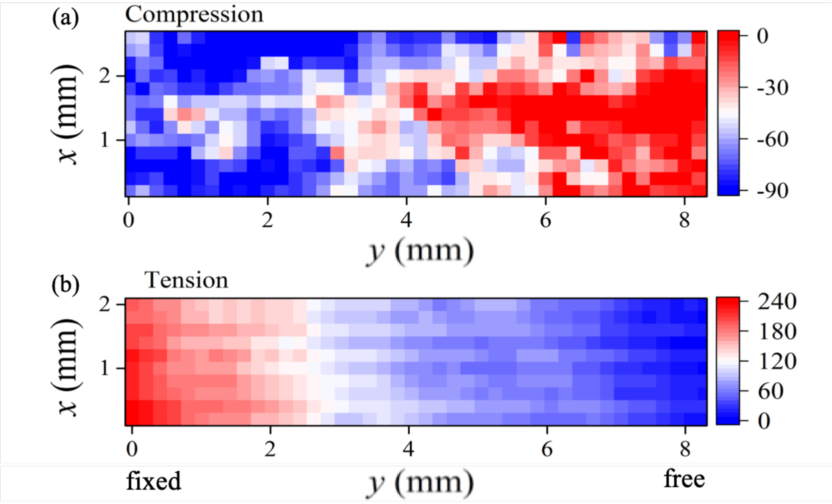

Fig. 5.9 Maps of the uniaxial mechanical stress applied parallel to the $y-$direction ($\langle 110 \rangle$ crystal direction) obtained using Raman spectroscopy for a cantilever whose top surface is under compression (a) and tension (b). The $x-$ and $y-$coordinates of the maps correspond to those given in the image of the cantilever in Fig. 5.4(a). Colour bars correspond to the measured stress in MPa.

torsion on the cantilever. This demonstrates nicely why the stress should be measured using Raman spectroscopy rather than relying on the cantilever formula Eq. (5.9).

5.2.2 Stress verification

Even though, the stress estimation obtained by beam formula of cantilever is not a perfect method compare to the Raman spectroscopy, it is still worth using it as a verification of the stress distribution. The average deflection at the free end, Δz_{max}, is -117 μm and 214 μm in compression and tension respectively. Using an offset in the $y-$direction to account for the contacts Eq. (5.9) is re-written:

$$X = \frac{3Et\Delta z_{max}}{2l^2}(l - y_{offset} - y) \tag{5.12}$$

where $y_{offset} = 1.3$ mm is the length of the Ohmic contacts, E = 169 GPa is the modulus of elasticity [120], $t \approx 400$ μm is the thickness of cantilever and $l = 11$ mm is the length of cantilever. The estimation of stress on the surface of cantilever according to Eq. (5.12) is shown in Fig. 5.10, with the red and black lines corresponding to the compressive and tensile stresses respectively. The red and black dots present stresses averaged along the $x-$coordinate in Fig. 5.9. The stresses obtained by the two different methods are well matched to each other, a convincing confirmation of the results measured by Raman spectroscopy.

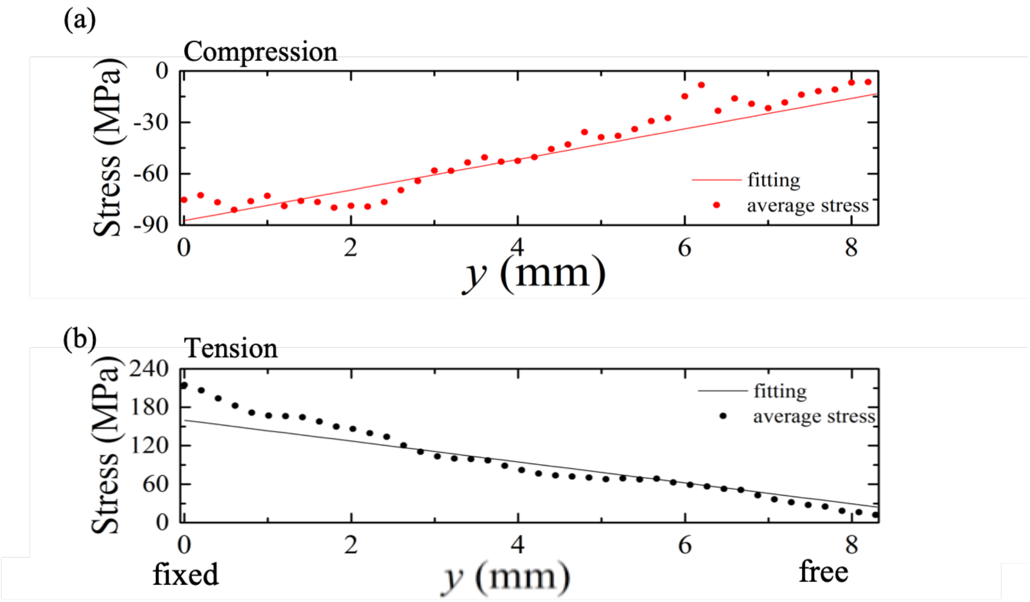

Fig. 5.10 The line profiles (dots) found by averaging over the measured stress at each x value for a given y value of the stress maps shown in Fig. 5.9. They agree well with the values found by using the beam formula and the measured amplitude of the free end deflection (solid lines).

5.3 X-ray photo-emission mapping on statically deflected silicon cantilevers

X-ray photo-emission spectrometer

The X-ray photo-emission spectroscopy experiments where performed at TEMPO beam line of the SOLEIL Synchrotron radiation source with the project number 20170112. A photograph of the whole system is shown as Fig. 5.11. The pre-stressed cantilever is put in the transfer chamber and then sent to the UHV analysis chamber. An X-ray photon beam ($h\nu = 200\ eV$) is incident on the sample surface, and a Scienta SES 2002 electron energy analyzer operated in the swept and fixed modes with a 100 eV pass energy is used to measure the kinetic energy spectrum of electrons photo-emitted from the sample. Without any further modification to the cantilever deflection Δz, these two cantilevers were taken to this beam line and measured by XPS. The scanned area and number of scanning pixels on the cantilever are identical to the Raman spectroscopy experiment, so that, the measured stress-induced surface Fermi level shifts can be matched to the stress as much as possible.

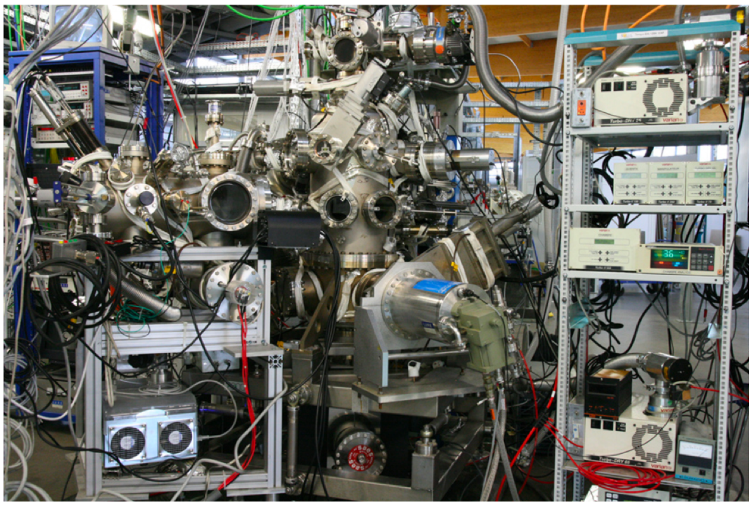

Fig. 5.11 X-ray photo-emission spectrometer at the TEMPO beam line in the Soleil Synchrotron. Extracted from https: www.synchrotron-soleil.fr.

5.3.1 Swept scan mode — surface oxidation distribution

It should be noted, that XPS peaks are observed to shift not only along the $y-$direction of the cantilever due to stress but also across the $x-$direction of cantilever. Analysis shows that this latter peak shift is due to a variation in the oxide thickness across the width of cantilever.

A typical XPS spectrum in kinetic energy is taken near the middle of the tensile stressed cantilever and shown in Fig. 5.12 (red dots with black line) as an example. This spectrum includes the silicon Si 2p core level peaks arising from silicon incorporated in the oxide, and the oxidation state is labeled as 1^+, 2^+, 3^+ and 4^+ for Si atoms bonded to 1, 2, 3 or 4 oxygen atoms respectively. As well as the silicon of the crystal itself which is indicated by Si^0 2p 3/2 and Si 2p 2nd plane labeled B and I respectively in Fig. 5.12. The kinetic energy ranges from 94.5 eV to 102.5 eV with a 20 meV step, a so-called swept scan. In swept scans, we have complete information about silicon and its various possible ionic states in the disordered oxide. Each state yields a doublet with a spin-orbit splitting of about 0.6 eV, and the intensity ratio is 1:2 between 1/2 and 3/2 spin-orbit split states forming each doublet. The spectra are fitted using Voigt functions, i.e. the convolution of a Gaussian by a Lorentzian. The choice of the surface components is inspired by previous XPS works on the oxidized silicon surface [121, 122]. The intensity, area, kinetic energy shift and Gaussian broadening of the Voigt functions are summarized in Table 5.2.

Generally speaking, the bond energy between $Si-O$ is lower than that of $Si-Si$ [123], and therefore the existence of oxidation states will be reflected in the XPS spectrum, i.e. the shifted Si 2p core level. This explains why the silicon oxide states' peak could be observed by photo-emission spectra. More importantly, these bonds influence the $Si-Si$ bond as well

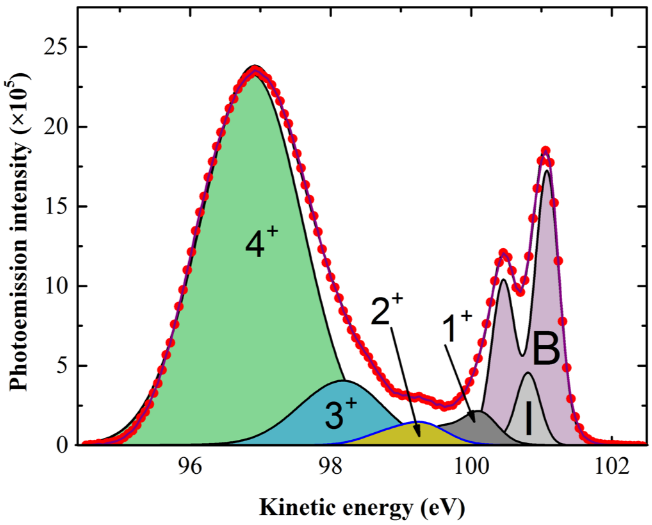

Fig. 5.12 Swept scan XPS *Si* 2p core level spectrum ($h\nu = 200\ eV$) of the middle pixel on the tensile stressed cantilever surface. The experimental data curve (red dots) is fitted with sums of Voigt components (black solid lines). The fitting components are represented as colored lines, each of them consisting of a Voigt doublet. The fitting parameters are reported in Table 5.2.

Table 5.2 XPS fitting parameters used in the 5.12 in the swept scan mode.

core level	**Lable**	**Intensity** $\times 10^5$	**Relative** E_k **shift** (eV)	**Width** (eV)
Si 2p 3/2	B	17.5	0	0.44
Si 2p 2nd plane	I	4	-0.23	0.37
Si^+ 3/2	1^+	2.5	-0.9	0.57
Si^{2+} 3/2	2^+	1.6	-1.88	0.9
Si^{3+} 3/2	3^+	5.6	-2.9	1.1
Si^{4+} 3/2	4^+	16.2	-4.1	1.66

including bulk *Si* 2p core level, the so-called "chemical shift" of the oxidation states. This "chemical shift" is surface oxide thickness dependent [124], i.e. the differences between silicon oxidation states 2p core level and bulk silicon 2p core level increase with increasing oxide thickness. The thicker the silicon oxide layer, the more silicon/oxygen bonds exist, implying greater influence on the *Si* 2p peak position [122, 125]. Therefore, the silicon oxide layer thickness becomes extremely important in the analysis of the stress-induced band bending shift because its value affects the peak positions too. In this section, we will discuss the influence of oxidation on *Si* 2p 3/2 core level peak intensity and position, and how to correct for the effect of the oxide thickness. Luckily, it is possible to estimate the oxide thickness from the relative integrated intensities of the bulk and oxide components obtained by a fitting process (see Table. 5.2) according to [126, 127]:

$$d_{ox} = \lambda sin\theta ln[\frac{I_{SiO_2}}{I_{Si}}A + 1] \tag{5.13}$$

where $A = (D_s y_s \lambda_s)/(D_f y_f \lambda_f)$. Here $\theta = 90°$ is the take-off angle related to the experimental geometry, D_s and D_f are the densities of silicon atoms in the crystal and surface oxide layer respectively, y_s and y_f are the atomic photo-ionization cross sections, and $\lambda_s = 0.56$ *n*m and $\lambda_f = 0.54$ *nm* are the electron escape depths for this photon wavelength [115, 127]. Using the values in Table 5.2 corresponding to the spectrum shown in Fig. 5.12, this yields an approximate oxide thickness of 1.15 *nm*. By repeating this procedure for each spectrum measured by scanning the cantilever in front of the beam, a map of the SiO_2 thickness is obtained as shown in Fig. 5.13(a). The oxidation thickness distributes between 1 *nm* and 1.4 *nm*, presented as color (see color bar). Intriguingly, the silicon oxide is systematically thinner along the central axis of the cantilever than along its two edges. This is attributed to the fact that during the two-month storage time mentioned above, the protective photoresist only allows for oxidation of the silicon to occur via oxygen diffusion from the sawn edges of the cantilever. The effective oxygen exposure time is therefore longest towards the edges of the cantilever, resulting in an oxide layer that tends to be thicker there than along the middle of the cantilever. The absolute kinetic energy difference between Si^{4+} 2p core level and bulk *Si* 2p core level versus oxide thickness in $x-$direction is plotted in Fig. 5.9(b) (red dots). In $x-$direction, the cantilever has less influence from stress due to the homogeneous stress distribution (see maps in Fig. 5.9), however the influence from the oxide thickness in this direction is stronger. The value of the energy shift of Si^{4+} approximates that without stress reported by Th. Eickhoff [124], (see empty circles of *Si* 2p in Fig. 5.9(b)) and the slope respects to oxide thickness is about 500 meV/nm [125]. Therefore, in addition to stress, the inhomogeneous oxide thickness can also shift the observed bulk *Si* 2p core level. Obviously, in order to estimate the surface band bending energy shift induced by stress, it is important to separate the oxidation effect from it. The pixels with the same $y-$coordinate in the middle of cantilever ($y \approx 4mm$) are selected and analyzed. These pixels affected by approximately identical stress but with variable oxidation thickness, shown as black curve in Fig. 5.14(a). However, the intensity of bulk *Si* 2p core level tends oppositely which is presented as blue curve in Fig. 5.14(a). In other words, the intensity decreases as oxide thickness increases (see Fig. 5.14(b)). Therefore, it is then possible to avoid oxidation-induced "chemical shift" by choosing the pixels with the same oxide thickness, i.e. the same intensity of *Si* 2p core

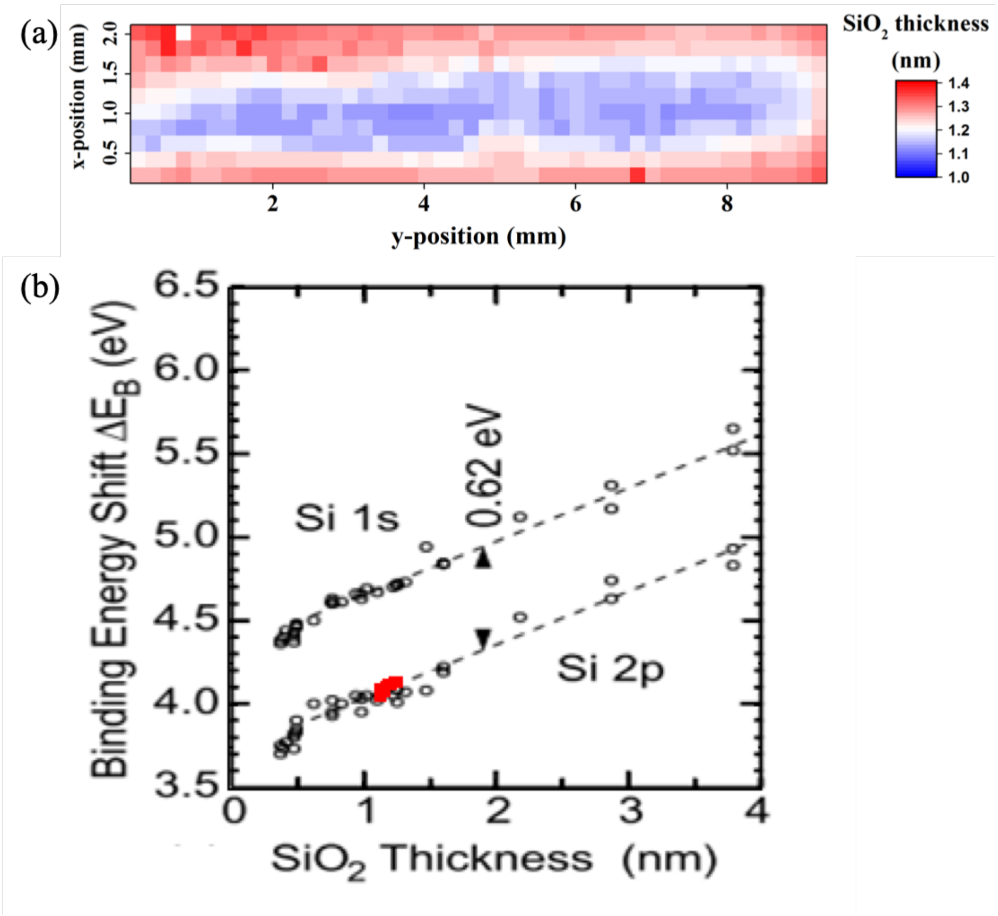

Fig. 5.13 (a) The calculated surface silicon oxide thickness distribution of the tensile stressed sample demonstrates that the oxide layer is thicker near the edges of the sample. (b) Energy shift of Si^{4+} versus oxide thickness from $x-$direction of cantilever under tensile stress (red dots) and reported by *Th. Eickhoff* (empty circles of *Si* 2p) respectively [124].

level. In order to avoid as much as possible the influence of the oxide related peaks, we focus on the bulk *Si* 2p 3/2 core level peak position for the study of stress-induced core level shifts since this peak is furthest from the oxide related peaks.

5.3.2 Fixed scan mode — surface Fermi level shift

In the last section, the influence of surface oxidation was discussed and a solution to avoid the oxide-induced shift in bulk *Si* 2p 3/2 core levels was also given. In this section, the stress-induced shift in the surface Fermi level will be discussed. Instead of a swept scan mode, the fixed mode will be used here because it is faster. The spectral window can be fixed but a narrower electron kinetic energy range will be recorded. Here a kinetic energy range from 99.2 *eV* to 102.3 *eV* with a 10.4 *meV* step was used since it contains information mostly

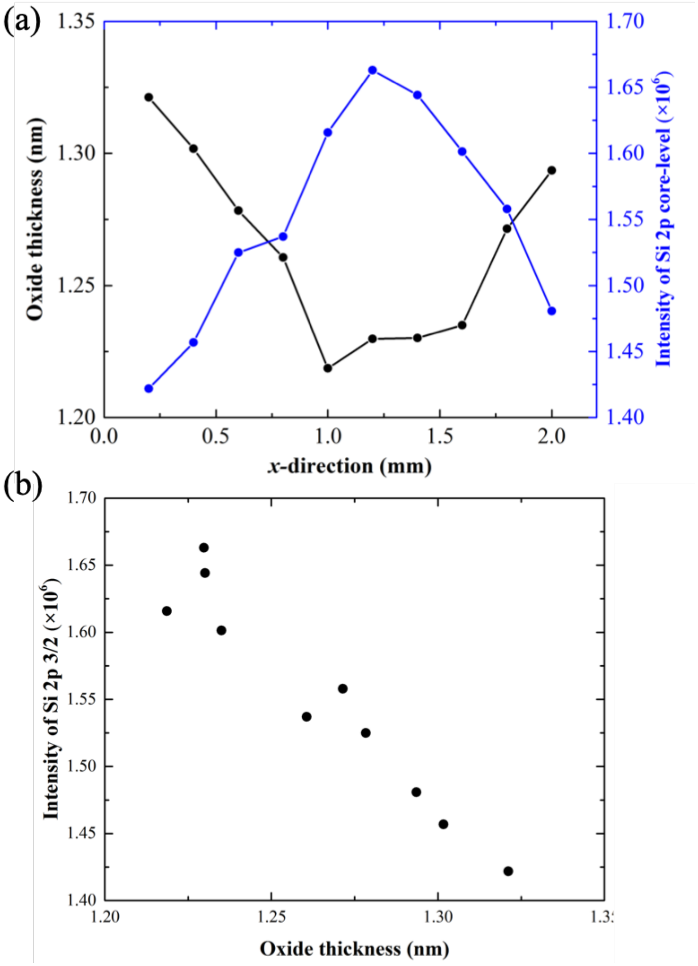

Fig. 5.14 (a)The oxide thickness (black curve) and the intensity of bulk *Si* 2p core level (blue curve) versus x-direction position on the cantilever respectively. (b) Intensity of bulk *Si* 2p core level is linear to the oxide thickness indicates that the thicker oxide layer corresponds to lower intensity, *vice versa*.

about the bulk silicon 2p core levels and a partially of the oxide states ($Si+$). Measurement of maps with a spatial resolution equivalent to those performed with Raman spectroscopy using a swept scan requires approximately 16 to 20 hours for each sample, while the fixed scan only takes about 6 to 8 hours. In order to save time to do as many experiments as possible in 3 beam-time days, we did one initial swept scan and another 3 fixed scans of the two available samples. This saved 30 to 36 hours allow us to finish our experiments in time. In the fixed scan, the spectrum is fitted by three sets of Voigt curves, two doublets corresponding to the spin-orbit split *Si* 2p core level doublets for the bulk silicon and the 2nd plane of silicon atoms respectively, and a singlet corresponding to a *Si* 2p oxide peak [121]. The doublet splittings are fixed at about 0.6 eV and the intensity ratio of each doublet is 1:2. The combination of these constrained components fits the measured spectrum well as presented in Fig. 5.15. The fitting parameters are reported in Table 5.3. The oxidation state is labeled as $Si+$, the label B and I indicate Si^0 2p and Si 2p 2nd plane respectively as for the swept scan.

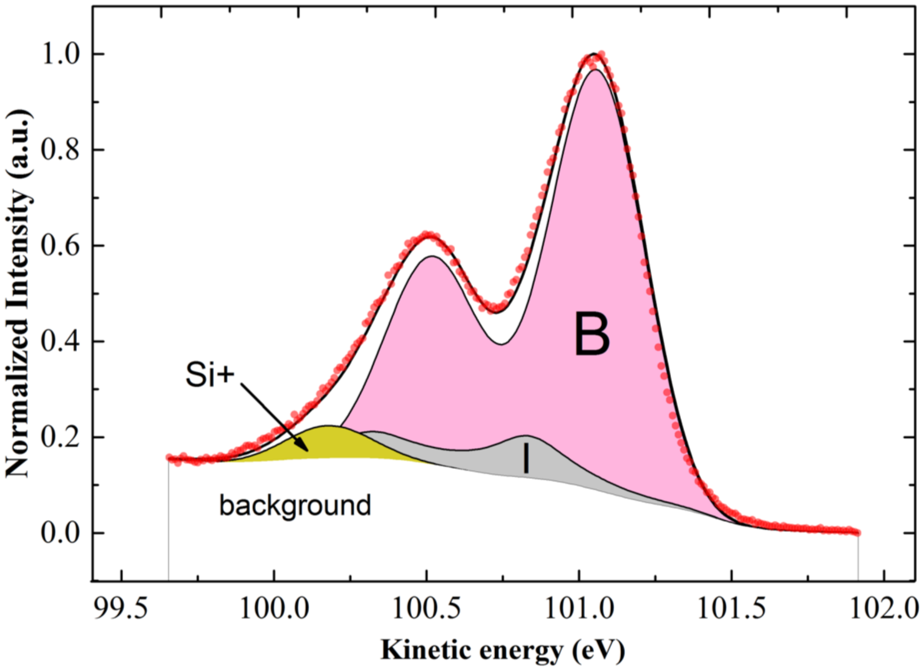

Fig. 5.15 Fixed scan XPS Si 2p spectrum ($h\nu = 200\ eV$) of the middle pixel on the compressively stressed cantilever surface. The experimental curves (red dots) are fitted with sums of Voigt components (black solid lines). The fitting components are represented as black lines, each of them consists of a Voigt doublet. The fitting parameters are reported in Table 5.3.

Table 5.3 XPS fitting parameters used in Fig. 5.15 in the fixed scan mode.

core level	**Label**	**Intensity** $\times 10^5$	**Relative** E_k **shift** (eV)	**Width** (eV)
Si^0 2p 3/2	B	22.1	0	0.4
Si 2p 2nd plane	I	1.2	-0.25	0.35
Si^+ 3/2	$Si+$	2.08	-0.99	0.38

According to the discussion in the section above, to avoid the influence of oxide thickness, only the pixels with the same bulk Si 2p core level intensity are taken into account. Repeating this fitting process for each detected pixel the intensity of the bulk Si 2p 3/2 core levels are obtained and shown in Fig. 5.16(a) and (c) as maps in compression and tension respectively. Both of these maps indicate that higher intensity is detected in the middle of the map, while lower intensity is detected around the edges, consistent with the inhomogeneous surface oxide thickness distribution (see Fig. 5.13(a)). The correction for the variable oxide thickness is achieved by extracting (for each value of the $x-$coordinate) only pixels whose intensity is the same along the y-direction, at least to within an arbitrarily imposed 2 % variation around some mean value. It's then possible, to estimate the unique stress induced changes in *Si* 2p core levels. The selected pixels are shown in Fig. 5.16(b) and (d), and the similar intensities manifest themselves as constant colours along each line in the $y-$direction.

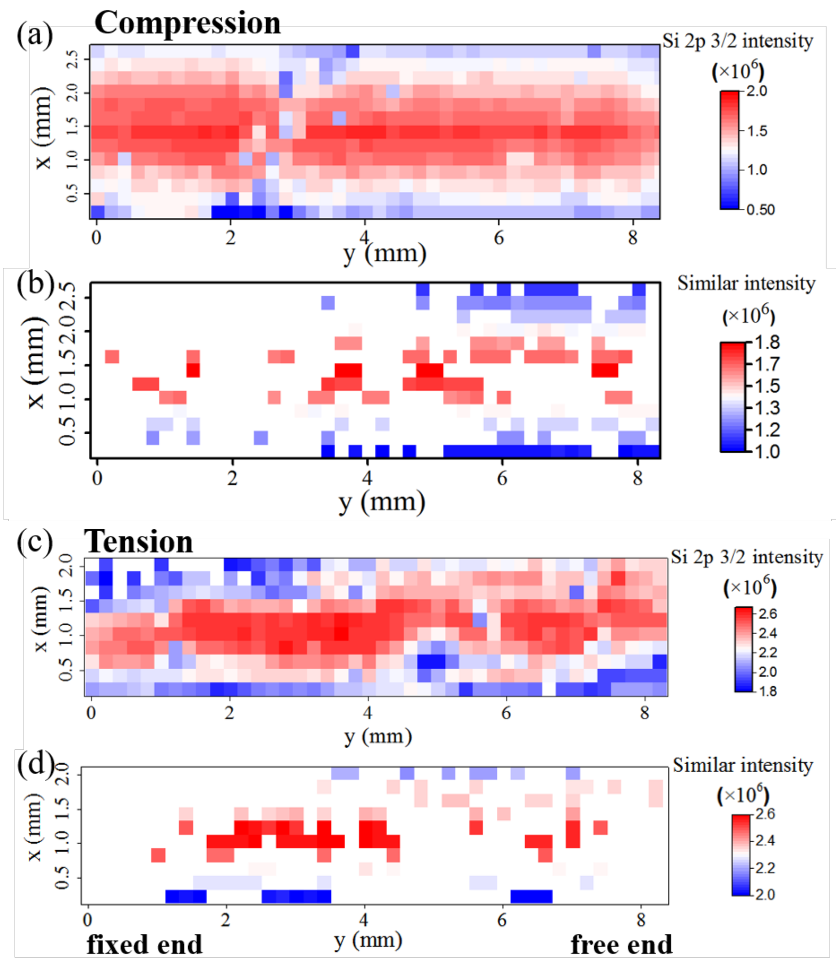

Fig. 5.16 The intensity of bulk *Si* 2p core level map of (a) compressive and (c) tensile stressed cantilever. (b) and (d) present the pixels selected according to their similar bulk *Si* 2p 3/2 core level intensity in each $y-$coordinate of compressive and tensile stressed cantilever respectively.

Since they have similar intensities, the pixels shown in Figs. 5.16(b) and (d) have the same oxidation "chemical shift" effect, and therefore any relative shift of bulk *Si* 2p 3/2 core levels for these pixels is due purely to external mechanical stress. As stress is approximately zero at the free end according to the stress estimated by Raman spectroscopy (see Fig. 5.9), the bulk *Si* 2p 3/2 core level peak position at the free end of the cantilever is regarded as the reference, and the difference between that and the peak position of other pixels is the relative shift of the bulk *Si* 2p 3/2 core level due to stress. Fig. 5.17 (a) and (b) are maps of stress-induced relative shifts of the pixels in the compressive and tensile stressed cases respectively. These pixels' $x-$ and $y-$coordinates are identical to those shown in Fig. 5.16(b) and (d). The maximum shift is 16 *meV* and 25 *meV* under compressive and tensile stress respectively. From the colour of both maps, regardless of whether the stress is compressive or tensile the shift tends to be in the same direction. The colour is more red on the left hand side of the maps where the compressive and tensile stress magnitudes are largest. This is the first suggestion that the *Si* 2p 3/2 core level positions exhibit an even response in applied stress. In order to observe the stress-induced shifts directly, and to illustrate the ability to resolve XPS peaks with *meV* accuracy, three example spectra are chosen (corresponding to

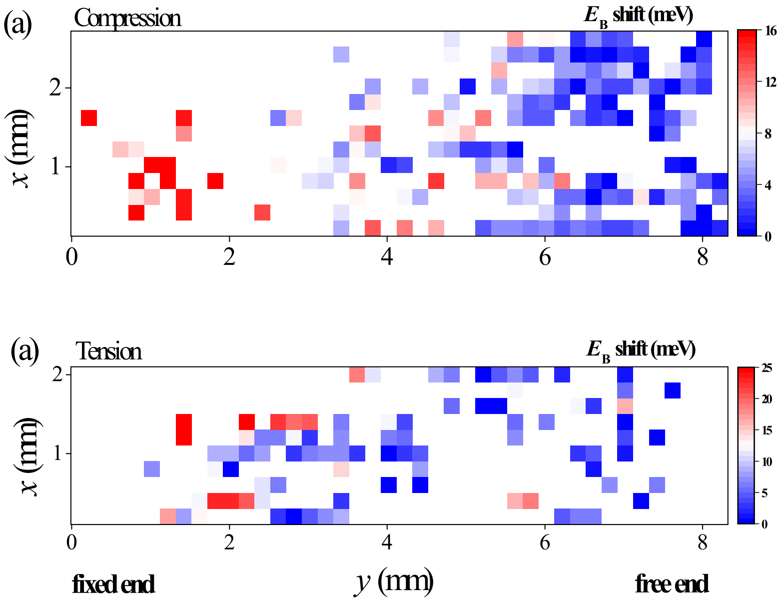

Fig. 5.17 Maps of the *Si* 2p 3/2 core level peak shifts relative to that obtained at the free end of the cantilever under (a) compressive stress and (b) tensile stress. The active (coloured) pixels shown in the maps are selected because they have, to within 2 %, the same intensities and therefore oxide thickness. The $x-$ and $y-$coordinates of the pixels shown in the maps correspond to the coordinates in Fig. 5.16(b) and (d).

the pixels shown in Fig. 5.18(a)) for the cantilever whose top surface is under tensile stress. These spectra are normalized in order to more easily observe the peak position shifts in Fig. 5.18(b). The colors of the lines and data points in Fig. 5.18(b) correspond to the equivalently colored pixels in Fig. 5.18(a) whose x-coordinate is identical.

Since the sensitivity of each pixel in the electron detector is not absolutely equal, the observed spectrum must be affected by this factor. From the inset of Fig. 5.18(b), the zoomed black rectangle area of the bulk *Si* 2p core level in Fig. 5.18(b), the spectra are not perfectly smooth due to this variation. Despite this a leftward shift from the red spectrum (with no stress) to the black spectrum (with maximum stress) is still clearly visible. The gray column is 20 *meV* large, which is approximately the scale of stress induced energy shifts. The energy between two raw data points in the spectrum is 10.4 *meV* and the stress is then able to shift energy of approximate three pixels. The fitting procedure allows us to precisely estimate the *Si* 2p 3/2 core level position of bulk silicon and its different oxidation states. The shape and width of these components are fixed, with the only free parameters being the intensity and peak position. From the fitting result, the 95% confidence interval of each parameter can be obtained; the standard error of bulk *Si* 2p 3/2 core level peak position can be consequently calculated by using 95% confidence interval which is about 3 *meV*. The same is also true for compression, three XPS spectra have been selected in Fig.

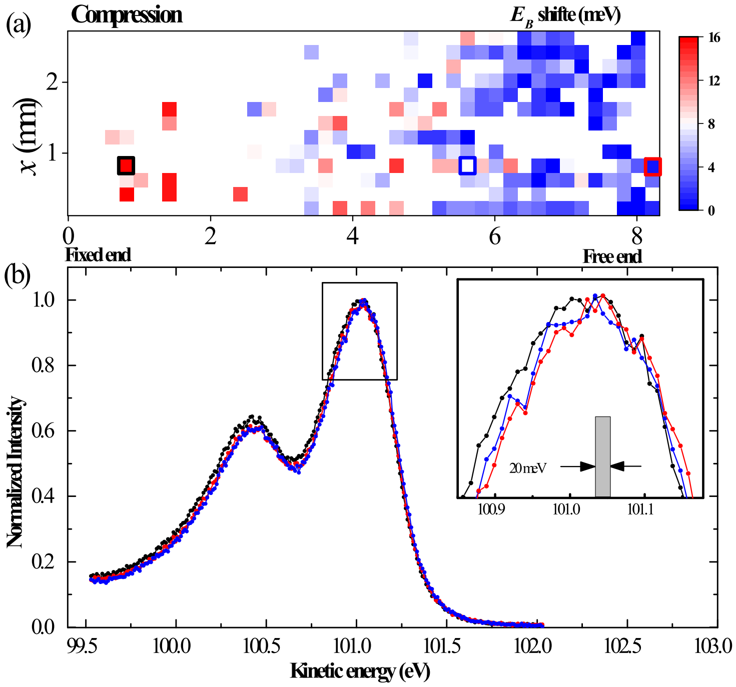

Fig. 5.18 (a) The *Si* 2p 3/2 core level peak shift of the tensile stressed cantilever: three selected pixels are presented by coloured rectangles and their XPS spectra are shown in (b).

5.19(a) for the cantilever whose top surface is under compressive stress. The peak position of kinetic energy under compressive stress is also leftward shift from red spectrum (with no stress) to the black spectrum (with maximum stress) as shown in Fig. 5.19(b). These two

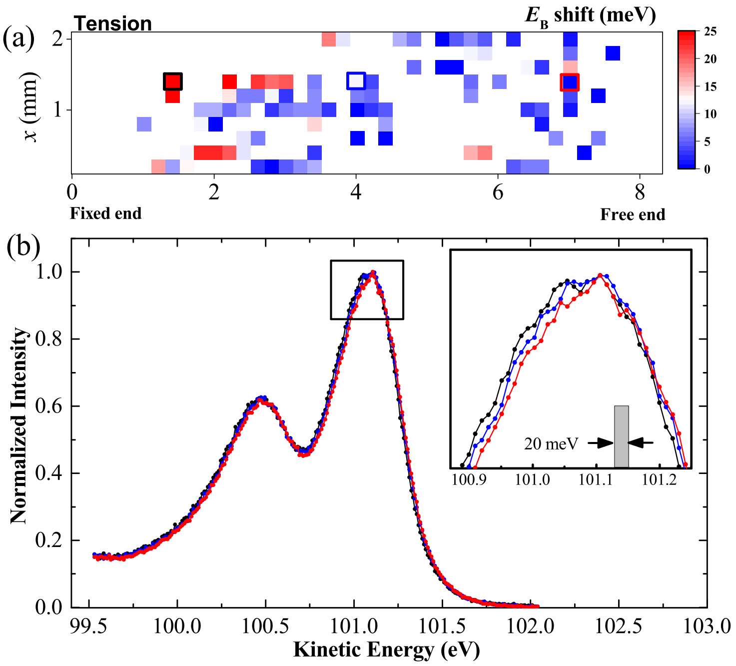

Fig. 5.19 (a) The *Si* 2p 3/2 core level peak shift of compressive stressed cantilever: three selected pixels are presented by coloured rectangles and their XPS spectra are shown in (b).

maps (see Fig. 5.17) are separated into areas containing approximately the same number of pixels (fifteen), denoted by the gray rectangles in Figs. 5.20(a) and (b). The pixels in the red, green and black rectangles on the compressively stressed surface are selected to demonstrate how the data is subsequently plotted in Fig. 4.20(a). The data histograms from these three rectangles are as shown, color coded, in Fig. 5.20(c). The stress-induced shift in the center-of-mass of these histograms is clearly visible, moving from lower shifts in the black rectangle (free end) to higher shifts in the red rectangle (fixed end). In each rectangle, the mean and standard error of the shifts are calculated and marked in Fig. 5.20(c) with a black line and gray box respectively. From the fixed to the free end they are 14.6 ± 1.1 *meV*, 6.5 ± 0.7 *meV* and 1.5 ± 0.4 *meV* respectively. These values, which are relatively robust to changes in the rectangle sizes (i.e. the number of points chosen in each rectangle) establish the mean *Si* 2p 3/2 core level shift as a function of the mean y-position of the pixels in each rectangle.

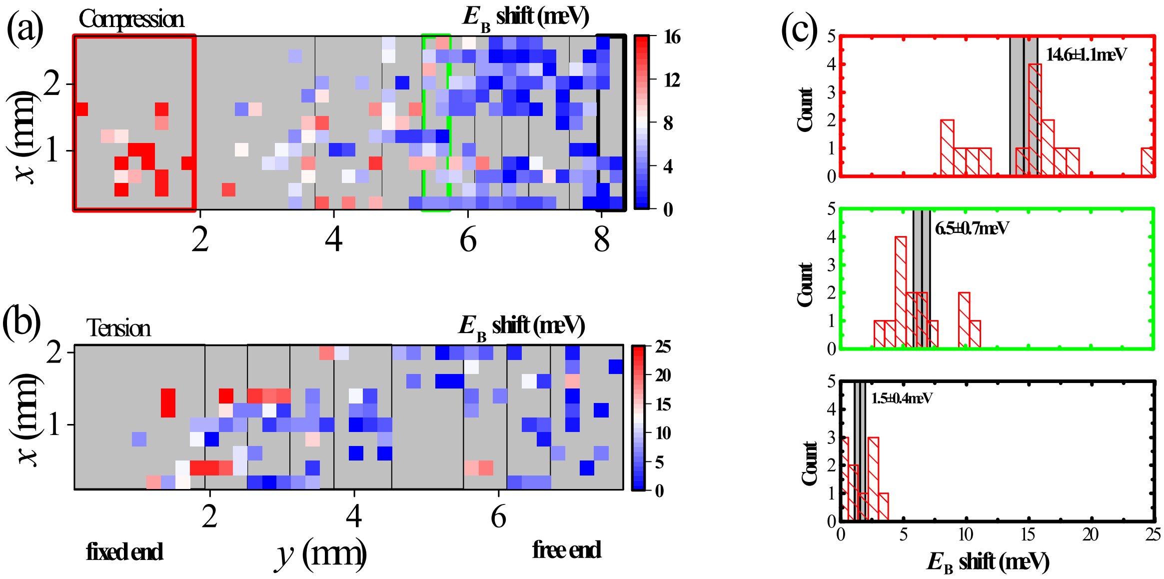

Fig. 5.20 Maps of stress-induced relative *Si* 2p core level peak shifts of the pixels with similar bulk *Si* 2p core level intensities under (a) compressive and (b) tensile stress. The pixels are separated into groups of a fixed number and presented in gray boxes. (c) The histogram plots of the relative *Si* 2p 3/2 core level peak shift of the pixels shown in the colored rectangles of (a). The mean and standard error values of these data, represented as a black line and a gray box respectively, will be combined with the micro-Raman spectroscopy data to obtain the *Si* 2p 3/2 core level peak shift as a function of applied stress.

5.4 Tension and compression: symmetry of Fermi level shifts in applied stress

According to Eq. (5.5) and the graphical arguments given in Fig. 5.3, the stress induced *Si* 2p 3/2 core level shifts that have been discussed so far are the binding energy shifts dE_B/dX, and can therefore be assimilated with a shift in the energy of the surface, dE_T/dX. By using the E_T shift of the pixels and their corresponding Raman shift (see Fig. 5.9) it is possible to plot the stress-induced E_T shift versus the applied stress as shown in Fig. 5.21. The red and black dots indicate the stress dependence of E_T in compressive and tensile stress respectively, and the error bars of both stress and E_T shift are estimated from the pixels in the gray rectangles as shown in Fig. 5.20(a). Two fit lines are shown here according to these results, implying that in compression E_T increases by 0.16 meV/MPa while for tensile stresses it increases by 0.11 meV/MPa.

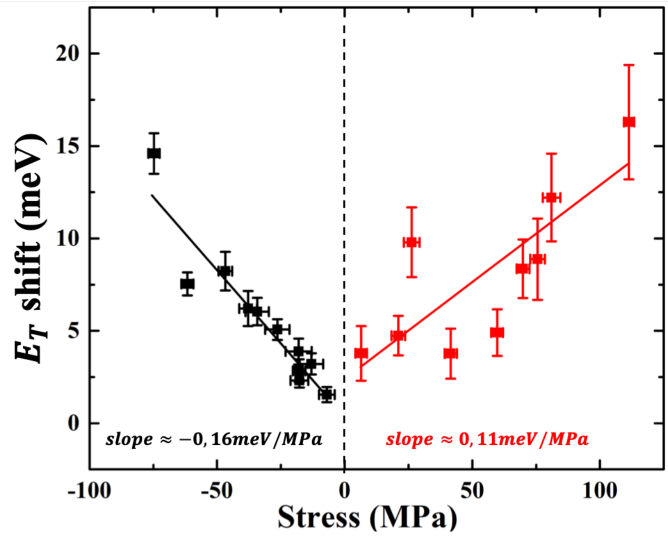

Fig. 5.21 The E_T shift exhibits an even response in stress.

The even symmetry of the E_T shift is unusual compared to stress-induced variations in bulk electronic levels which are odd in stress (see section 2.2) [128], but it is consistent with interface leakage currents measurements [104, 105] and more recently to theoretical estimations of stress-induced energy shifts on other silicon surfaces [106]. The exact origin of this even symmetry is not established, but the symmetry of the intrinsic Pb_0 Si/SiO_2 was previously speculated to be responsible [104, 105]. This interpretation is comforted by the fact that stress-induced shifts in E_T of Si/SiO_2 interface traps obtained by indirect transport measurements on MOS capacitors are of similar magnitude [107] to the shifts obtained here.

To explore this idea further, Fig. 5.22(a) shows the two possible Pb_0 interface defect structures on a (001) silicon surface. In the left structure, referred to as the parallel geometry, the red dangling bond points in the $\langle 111 \rangle$ crystal direction and therefore has a spatial component parallel to the $\langle 110 \rangle$ crystal direction along which stress is applied. In the right hand side of Fig. 5.22(a), referred to as the perpendicular geometry, the red, dangling bond points in the $\langle \bar{1}11 \rangle$ crystal direction and therefore has a spatial component perpendicular to the $\langle 110\ \rangle$ crystal direction. In both cases the stress can be visualized as a force applied uniformly along the thick, black edges of the unit cell parallel to the light blue plane. The arrows in the left panel of Fig. 5.22(a) represent the applied force that yields in a uni-axial tensile stress. In the following, a simple relative estimation of the Coulomb potential at the end of the dangling bond due to the electronic charge present in the back bonds (shown in blue and green) will be made as a function of the applied stress. The motivation for this [105] is the notion that this energy will determine E_a for Pb_0 interface traps. Using the compliance tensor for silicon [56], the effect of applied stress on the bond angles, and hence

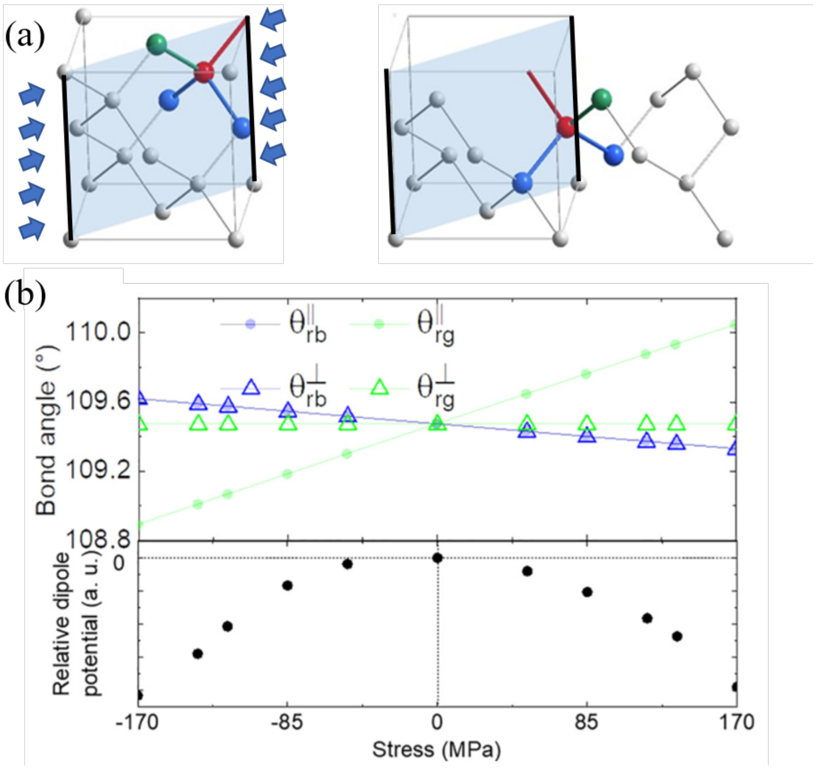

Fig. 5.22 (a) The two possible orientations of the Pb_0 defect at the (001) surface. Stress is applied in the $\langle 110\ \rangle$ direction, and the case of compression is indicated by the blue arrows. The blue $\langle 1\bar{1}0 \rangle$ plane serves as a guide to the eye. (b) The stress induced changes in bond angles versus strain, the blue curves correspond to the changes in bond angle between the red dangling bond and the blue back bonds; the green curves correspond to that between the red dangling bond and the green bond. The bottom panel shows the estimated Coulomb potential energy of an electron in the red dangling bond with respect to stress.

on the relative changes in distance between the ends of the bonds can be estimated. This can then be used to estimate the stress-induced changes to the total Coulomb potential at the dangling bond. The calculated changes in the back bond angles are shown in the top panel of Fig. 5.22(b). For a tensile stress the bond angle between the red dangling bond and green back bond in the parallel geometry, $\theta^{||}_{\mathrm{rg}}$, increases (see filled, green circles in Fig. 5.22(b)), while for the perpendicular geometry, $\theta^{\perp}_{\mathrm{rg}}$ slightly decreases due to Poisson's effect (see filled, green triangles in Fig. 4.22(b)). A compressive stress results in the opposite behavior. The bond angle between the red dangling bond and the blue back bonds in the parallel geometry, $\theta^{||}_{\mathrm{rb}}$, decreases under tensile stress due to Poisson's effect (see filled, blue circles in Fig. 5.22(b)), while in the perpendicular geometry, $\theta^{\perp}_{\mathrm{rb}}$, decreases (see filled, blue triangles in Fig. 5.22(b)). Again, the opposite is true for a compressive stress. A simple geometric calculation, assuming constant bond lengths, then yields a relative estimate of the Coulomb potential as a function of applied stress, and this is found to be even in stress, despite the fact that the bond angles themselves are odd in stress. This is possible because the stress-induced changes to $\theta_{\mathrm{rg}}^{\|}$ are partially compensated by opposite changes in $\theta_{\mathrm{rb}}^{\|}$ and $\theta_{\mathrm{rb}}^{\perp}$. While this is not proof that the symmetry of the Pb_0 centres is the sole origin of the even response in the stress-dependence of E_T, it is a proof of principle that two odd angular contributions can result in an overall even response.

5.5 Conclusion

In this Chapter, the Raman and XPS scanning experiments on silicon cantilevers have been presented, which are under tensile and compressive stresses respectively. The comparison of Raman and XPS maps provides a spectroscopic measurement of the stress-dependence of the surface Fermi level pinning at an oxidized (001) silicon surface. For uniaxial compression along the $\langle 110 \rangle$ crystal direction the pinning increases by $0.16\ meV/MPa$, while for tensile stress an increase of $0.11\ meV/MPa$ is measured. These quantities have previously only been inferred indirectly from transport measurements. A simplified analysis of the symmetry of the stress response tentatively suggests that the Fermi level is pinned by Pb_0 interface states, and also convinces that the Pb_0 defect is likely responsible for the giant, anomalous piezo-response measured in oxidized nano-silicon in the space charge limit as reported on in Chapter 4.

Chapter 6

“Anomalous” steady-state piezoresistance in defect engineered silicon

In Chapters 4 and 5, evidence for the central role of native Pb_0 interfacial defects in the giant, anomalous PZR and the novel PZC in the non-steady-state space charge limit was given. However, according to PICTS measurement (see appendix A), the trap distribution is continuous and broad in the band gap, and therefore it is not possible to simulate the impedance and piezo-response based on Kassing’s model using a single set of defect parameters, for example, only one value of ω_c and ω_e. In this chapter measurements on the devices containing only a single type of defect are reported. It was initially hoped therefore that impedance spectroscopy on such a defect engineered sample would more closely resemble Kassing’s one trap type model [74].

In the first section, the production of Si divacancy defects using silicon ion self-implantation will be discussed. For the resulting defect engineered device, a non-linear DC I-V characteristic will be presented in the section 6.3, and it will be separated into three regimes according to the current slope. Evidence for a switch from negative to positive (i.e. anomalous) PZR as a function of V_{ds} will be provided, and it will be argued that the sign change is in fact due to a $V_{ds}-$induced change in the majority charge carrier type. The impedance spectroscopy of G_0, C_0, π_R and π_C is shown in section 6.5, and relative to the samples before defect engineering, the implantation of Si divacancy defects will be seen to decrease G_0 while increasing C_0 as well as reducing the measured trap capture and emission rates. Unfortunately, it has proved difficulted to simultaneously model impedance and piezo-response based on Kassing’s model using a single set of defect parameters. However, the divacancy defect implantation indeed increases the reproducibility of the electrical behaviour of SCLC devices. Finally, section 6.6 will summarize the conclusions of this work.

6.1 Divacancy production by self-implantation of 10 *MeV* *Si*+ ions

The samples used here are shown in Fig. 3.4, and are made from a (001) oriented FD-SOI wafer with a device layer thickness of $d = 2\ \mu m$, and are non-intentionally $p-$type (Boron) doped with a resistivity $\rho > 5000\ \Omega cm$. According to Eq. (1.4), the Boron density in the fully ionized limit yields an approximate **surface depletion layer width of the order of 10 μm**, much larger than d i.e. the active layer is fully-depleted. In this case transport should occur in the space charge limit.

Volume divacancy defects are produced in the device layer by self-implantation of $Si+$ ions. The implantation was done by our collaborators at the University of Melbourne using the 14UD pelletron at the Australian National University. The pelletron accelerates a $Si+$ ions to a kinetic energy of 10 MeV, and these ions displaces silicon atoms in the sample from their lattice sites [129] forming divacancies as shown in Fig. 6.1. The two missing silicon atoms will influence the bonding of the lattice and result in an "extended bond" (see the dotted line in Fig. 6.1). These defects are stable at room temperature [130] and are electronically active, acting as charge traps [131]. Monte Carlo simulations of the $Si+$ ion scattering process for a fluence of $10^{12}\ Si+/cm^2$ shows that they reach a depth of 4.5 μm from the top of the SOI wafer as shown in Fig. 6.2. This means that most ions (and also divacancy defects) will be presence in the silicon substrate (handle). This profile was chosen so that the divacancy density be relatively constant over the device layer (DL) thickness (2 μm). The calculated areal density of divacancy defects is approximately $4.5 \times 10^{12}\ cm^{-2}$, much larger than typical interface defect densities ($1 \times 10^{12}\ cm^{-2}$). Therefore, the implanted divacancy defects dominate the interface defects.

After implantation, photo-induced current transient spectroscopy (PICTS) (see Appendix A) presents a single defect signal with a peak position at around 220 K for $V_{ds} = 6\ V$ as shown in Fig. 6.3. This indicates a defect state with $E_C - E_T = 0.44\ eV$ which is close to the value expected for the singly ionized divacancy defect [133].

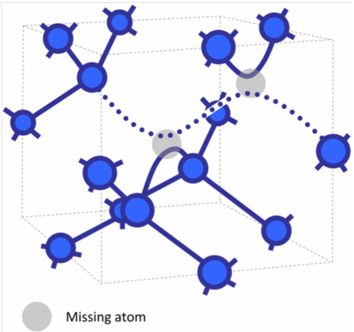

Fig. 6.1 Silicon divacancy defect diagram, the blue point corresponds to silicon atom and gray point corresponds to missing silicon atom. Extracted from Ref. [132].

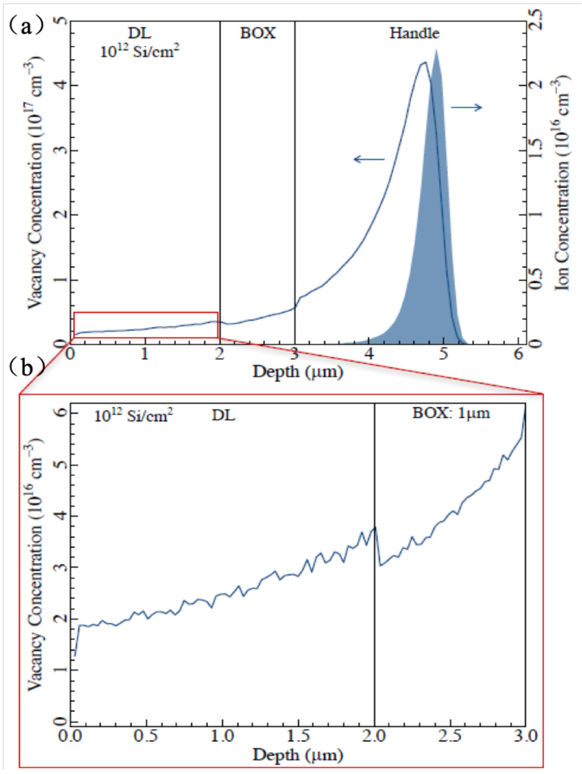

Fig. 6.2 Divacancy and $Si+$ ion concentration as a function of depth of sample. The maximum concentration of them occurs in the silicon handle. Whereas, divacancy concentration is quite identical in the device layer (DL).

6.2 Transfer characteristics: hysteresis effects and conduction type

After implantation, a DC voltage V_{ds} is applied between the source and drain of the device. At the same time, a potential is applied to the handle of the sample so that is can be used to

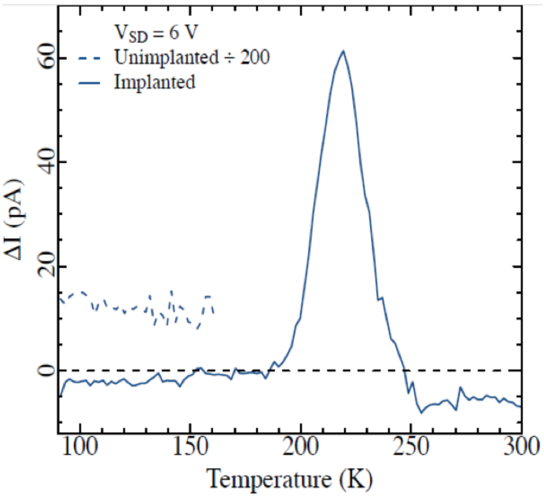

Fig. 6.3 PICTS spectrum of unimplanted (dotted curve) and implanted (solid line) SCLC device for $V_{ds} = 6\ V$.

gate the source-drain channel. In effect the BOX of the SOI is used as a gate dielectric and in the following the gate bias will be labeled V_{gs}. V_{gs} modifies the free carrier concentration in the device layer thereby modifying the drain current I_d. At low V_{ds}, I_d is linear as a function of V_{ds} and V_{gs}, and according to the general transistor model [36], for an $n-$type channel:

$$I_d = \frac{W}{L}\mu_n C_G(V_{gs} - V_T)V_{ds}, \tag{6.1}$$

while for $p-$type channel:

$$I_d = \frac{W}{L}\mu_p C_G(V_T - V_{gs})V_{ds}. \tag{6.2}$$

L and W are the length and width of the channel, μ_n and μ_p are the mobilities of electrons and holes respectively, C_G is geometric capacitance of the BOX and V_T is the threshold voltage as a function of majority charges n_0 and C_G.

In the experiment V_{ds} is fixed to 1 V and V_{gs} is swept forward and backward between -30 V and +30 V with a step of 3 V. The time constant between two V_{gs} data points is the so-called delay time. The transfer characteristic, i.e. the V_{gs} dependence of I_d, is shown for several delay times (1 s, 4 s, 8 s and 12 s) in Fig. 6.4. An obvious hysteresis effect is shown in the transfer characteristic of the device, which is usually caused by charge exchange processes between the Si/SiO_2 system and the channel. There are several types of charge source leading to the hysteresis [134]:

- Interface states.

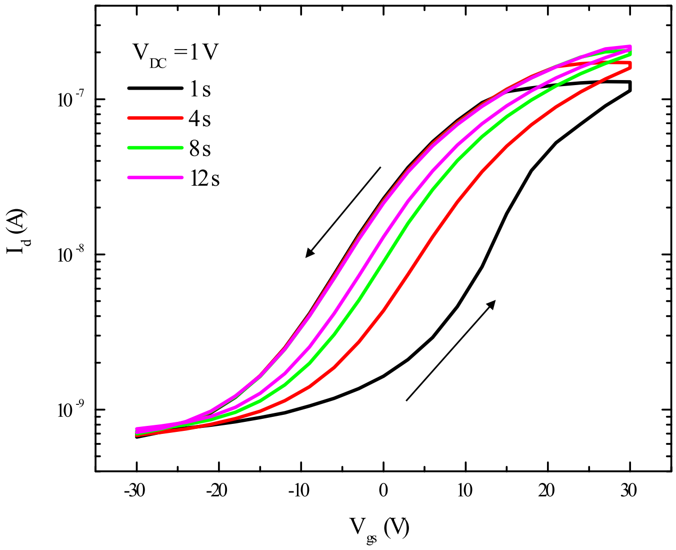

Fig. 6.4 The V_{gs} dependence of I_d is shown for several delay times when $V_{ds} = 1V$, the hysteresis effect is observed. The arrows indicate the sweep direction. In addition, since the slope of current is positive, the conduction through device layer is $n-$type according to Eq. (6.1).

- Fixed charge in the oxide layer which does not communicate directly with the *Si* device layer.
- Trapped charge in the oxide layer that can be injected into *Si* device layer.
- Ions in the oxide layer.

Apart from these charges, the implanted *Si* divacancy volume defects may also cause the hysteresis effect, and it is the mainly for this reason that the hysteresis is present here. Since V_T is related to n_0 and also C_G, the forward and backward sweep of V_{gs} would change n_0 and C_G due to charge exchange process with the traps [135–137], that will shift V_T of FET and further induce hysteresis effect as shown in the Fig. 6.4, if the sweep rate is fast enough compare to the rate of release of charge. In this case, the device will never reach the thermal equilibrium before the sweep finish [138]. If the sweep rate decreases, i.e. the delay time increases, then it is easier for the device to reach equilibrium, and the size of the hysteresis effect is smaller. As we can see from Fig. 6.4, the transfer characteristic has been measured for several delay times: 1 s, 4 s, 8 s and 12 s, and the size of the hysteresis decreases as delay time increases. These obvious and sizeable hysteresis effects convinces us that a large number of defects exist in the device.

More importantly, from Fig. 6.4, I_d in the positive V_{gs} regime is higher than I_d in the negative V_{gs} regime, i.e. the slope of I_d is positive which, according to Eq. (6.1), means that the majority charge carriers are electrons **i.e. the conduction through device layer is therefore n-type after implantation when $V_{ds} = 1\ V$, although the original device was unintentionally $p-$type doped.** By increasing V_{ds} from 1 V to 30 V in 5 V steps, the slope of I_d changes from positive to negative as shown in Fig. 6.5 (for values of V_{ds} above 30 V the leakage current from the handle to the device layer appears for large gate voltages). Interestingly, the slope of I_d is clearly negative above $V_{ds} = 15\ V$, and therefore according to Eq. (6.2) the majority carriers are holes i.e. V_{ds} induces a type change in the majority carrier. This can be explained by considering hole injection from the $p++$ contacts as will be discussed below.

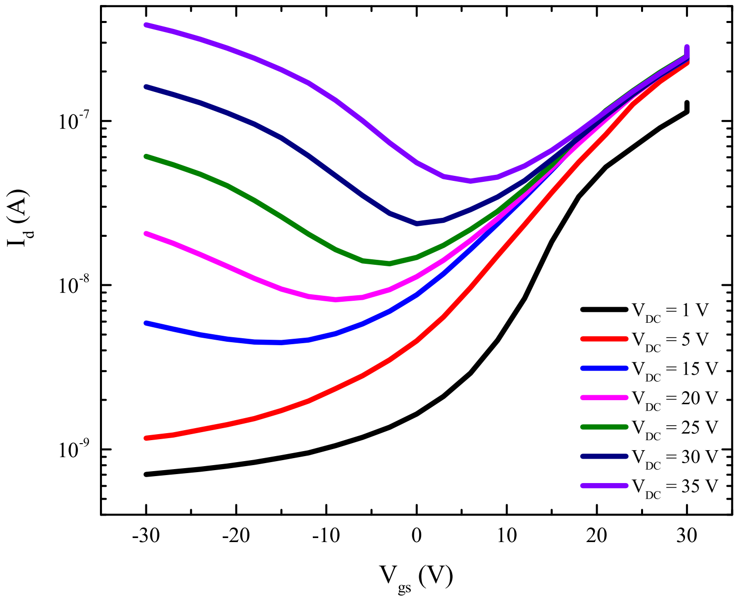

Fig. 6.5 The V_{gs} dependence of I_d is shown for several V_{ds} from 1 V to 30 V. The slope of I_d depends on V_{ds}, for $V_{ds} < 15\ V$, the slope of I_d is positive in V_{gs}, the conduction through device is $n-$type; for $V_{ds} \geqslant 15\ V$, the slope of I_d is negative in V_{gs}, the conduction through device is $p-$type.

6.3 Zero-stress current-voltage characteristics

The measured I-V characteristic of implanted devices will be presented and discussed here. From the slope of the I-V characteristic three regimes are established: the Ohmic regime at low bias, the SCLC regime at intermediate bias, and the plasma regime at high bias. Before showing the measurement results the details of each of these regimes will be discussed.

Ohmic regime

In this regime the current through the device is carried by equilibrium free charge carriers in the energy band, in this case electrons in the condunction band. The current is then:

$$I_{Ohmic} = tq\mu_n n V_{ds}, \tag{6.3}$$

where t is the thickness of device layer and n is the electron concentration.

SCLC regime

As V_{ds} increases external carriers begin to be injected into the device, and in the devices considered here holes are injected because the Ohmic contacts are $p++$ doped. In the SCLC limit the concentration of injected holes is significantly larger than the concentration of equilibrium electrons and, in the trap-free case, the current is proportional to V_{ds}^2 according to Mott-Gurney's law (see section 2.2). The current is given by [78]:

$$I_{SCLC} = \frac{9}{8}\varepsilon_0\varepsilon_r\mu_p\frac{V_{ds}^2}{L^3}t \tag{6.4}$$

where L is the length of the device between the two contacts. For a single type of trap whose energy lies E_T below the conduction band edge, not all the injected holes flow through the device from one contact to the other. Rather, a fraction of them are trapped, and the proportion of free holes to the total injected hole concentration may be written [139]:

$$\theta = \frac{p_0}{p_0 + p_{t0}}, \tag{6.5}$$

where p_0 is the free hole concentration and p_{t0} is trapped hole concentration. The trap emission and capture rates (ω_e and ω_c) are related to θ as discussed in section 2.3 [74, 72, 73]:

$$\theta \approx \frac{p_0}{p_{t0}} \approx \frac{\omega_e}{\omega_c}. \tag{6.6}$$

The space-charge-limited current is then written [80]:

$$I_{SCLC,\theta} = \theta\frac{9}{8}\varepsilon_0\varepsilon_r\mu_p\frac{V_{ds}^2}{L^3}t. \tag{6.7}$$

As discussed in section 2.4, ω_e changes with V_{ds} due to either phonon-assisted tunneling from the trap or the Poole-Frenkel effect [83]. Therefore, θ depends on V_{ds}. When V_{ds} reaches a sufficiently large value, the injected holes can flow through the device without any effective trapping because $\theta \approx 1$. The current will then be a trap-free SCLC [72].

Plasma regime

In the very high V_{ds} regime both electrons and holes are expected to be injected into the device from two contacts. This is the so-called plasma limit. The current is then proportional to V_{ds}^3 and given by [140, 141]:

$$I_{Plasma} = \frac{125}{18}\mu_n\mu_p\varepsilon_0\varepsilon_r\tau\frac{V_{ds}^3}{L^4}t, \tag{6.8}$$

where τ is the recombination time.

The I-V characteristic of the implanted device is measured from gate voltage sweeping experiments, i.e. in each gate sweeping process for a fixed V_{ds}, the current I_d is recorded when $V_{gs} = 0\ V$ and this current corresponds to the applied V_{ds}. As increasing V_{ds}, the I-V characteristic can be obtained and shown in Fig. 6.6(a) (see black dots). Obviously the I-V curve is not linear as the slope is dependent on the V_{ds}. The three regimes mentioned above are labeled as black (Ohmic), blue (SCLC) and red (plasma) rectangles in the figure.

The low-voltage Ohmic regime is represented in black and corresponds to $V_{ds} \leq 15\ V$ in Fig. 6.6(a). I_d has an approximately linear dependence on voltage (black line). Conduction through the device layer is $n-$type according to the gating experiment in Fig. 6.4. Assuming an electron mobility $\mu_n = 1400\ cm^2/Vs$, the accepted value for lightly doped $n-$type silicon [142], and using the known dimensions of the device (device layer thickness, t = 2 μm and device length, L = 100 μm) it is possible to estimate n = $1.8 \times 10^{10}\ cm^{-3}$ from Eq. (6.3). This value is self-consistent with the value assumed for the mobility [142] and yields the black line shown in Fig. 6.6(a). PICTS measurements show that the divacancy volume defects are implanted at energy $E_T = 0.44\ eV$ from the conduction band with concentration of about $2 \times 10^{16}\ cm^{-3}$. If the Fermi energy is pinned at E_T the estimated equilibrium electron concentration is by is about $6.3 \times 10^{11}\ cm^{-3}$, slightly larger than the value obtained from the I-V characteristic. This means that the Fermi level in fact lies between E_T and the intrinsic Fermi level E_i.

In the intermediate voltage regime ($15\ V < V_{ds} < 45\ V$) shown as the blue region in Fig. 6.6(a), the slope of the I-V characteristic is no longer linear, but is much steeper. This is an indication that the device is in the SCLC regime. The V_{gs} dependence of I_d in Fig. 6.5 indicates that the conduction is now p-type. Since the equilibrium electron density is very small (almost intrinsic), a possible interpetation is that the injected hole concentration (from the $p++$ contacts) is much larger. Therefore a unipolar hole SCLC is considered where

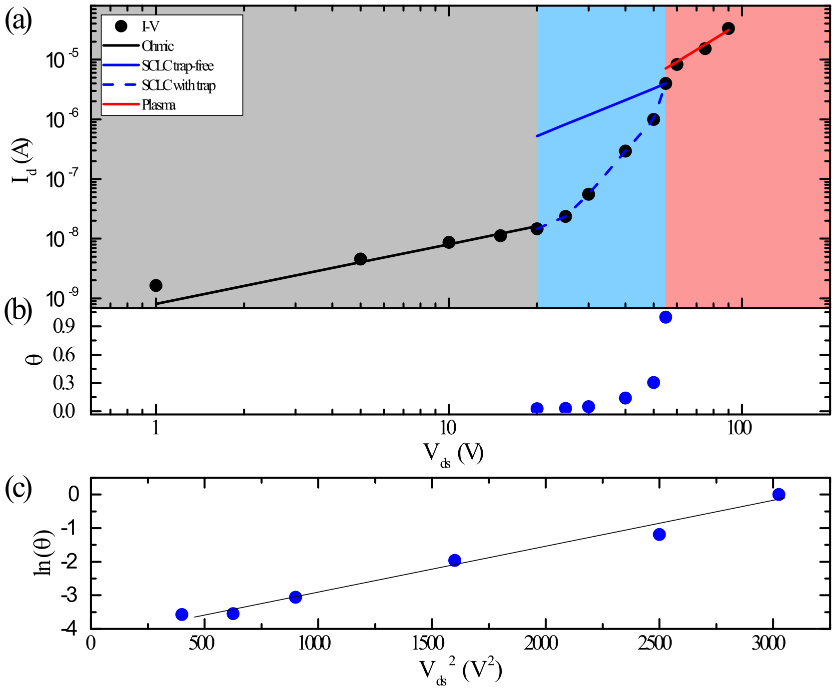

Fig. 6.6 (a) The current-voltage characteristic (black dots) of the defect engineered sample displaying three clear regimes: the ohmic regime (black region) where the current varies linearly in voltage, the unipolar SCLC regime (blue region) where a modified square law is expected, and the bipolar SCLC (or plasma) regime (red region) where a cube law is expected. (b) The trap filling factor, θ, calculated by matching the modified square law with the experimental data in the blue region. (c) Variation in $ln(\theta)$ with V_{ds}^2. The linear variation indicates that the voltage dependence of θ arises from phonon-assisted tunneling emission from the traps [83]

I_d is expected to be proportional to V_{ds}^2 as shown by Eq. (6.4). However, for a reasonable hole mobility, $\mu_p = 565\ cm^2/Vs$ Eq. (6.4) predicts a much larger current than that which is measured (the predicted line is shown labeled $I \sim V^2$ in Fig. 6.6). Moreover the measured current clearly does not follow a V_{ds}^2 law. This is interpetated as being result of the uniform divacancy defect density in the device layer that introduces a further voltage dependence of I_d due to the voltage dependence of θ appearing in Eq. (6.7). Since the $I \sim V^2$ curve crosses the data at $V_{ds} = 55\ V$, it will be assumed that this is the voltage at which $\theta = 1$. The values of θ for other voltages in the SCLC range are then chosen so that the curve given by Eq. (6.7) matches the data in the unipolar SCLC regime (see blue, dotted curve in Fig. 6.6(a)). These values are shown in Fig. 6.6(b). When plotted on a logarithmic scale versus V_{ds}^2 one obtains an approximately linear result as shown in Fig. 6.6(c). Based on the expression for θ in Eq. (6.6), $ln(\theta) = ln(\omega_e) - ln(\omega_c)$, as ω_c does not depend on voltage $ln(\omega_e)$ is therefore linearly dependent on V_{ds}^2. This is as excepted for phonon-assisted tunneling emission from traps [83].

In the high voltage regime ($V_{ds} > 45\ V$), the slope of the current is proportional to V_{ds}^3 as would be expected for the bipolar space charge limited current (or plasma) case [140]. The current is given as Eq. (6.8) and using the electron and hole mobilities (μ_n and μ_p) obtained from the Ohmic and the unipolar SCLC regimes, the fitted current is plotted in Fig. 6.6(a) with an estimated recombination time $\tau = 0.25\ ns$.

6.4 DC (zero-frequency) piezo-resistance at constant stress: voltage dependence

In this section the DC PZR of implanted devices will be discussed and the results are shown in Fig. 6.7. When $V_{gs} = 0\ V$ a negative DC PZR is observed in the Ohmic regime with a maximum magnitude $\pi_R \approx -20 \times 10^{-11} Pa^{-1}$ for $V_{ds} = 1\ V$. The PZR keeps decreasing in magnitude as V_{ds} increases and then change sign and eventually reaches a maximum of $\pi_R \approx +110 \times 10^{-11} Pa^{-1}$ in the unipolar SCLC regime. At high V_{ds} in the plasma regime a slightly smaller but flat PZR is measured with value of about $\pi_R \approx +80 \times 10^{-11} Pa^{-1}$. According to the first PZR measurement on bulk Si, the longitudinal $\pi-$coefficient along the $\langle 110 \rangle$ crystal direction in $p-$ and n-type material is $+71.8 \times 10^{-11} Pa^{-1}$ and $-31.2 \times 10^{-11} Pa^{-1}$ respectively [17] (see Table 2.2). These numbers are widely accepted and are represented as black and red dotted lines in Fig. 6.7. Since PZR is measured using DC voltages, π_R is estimated via stress induced changes to the current flowing through the device (see Eq. (3.2)). Therefore π_R can be written differently for the three voltage regimes considered here:

In the Ohmic regime, the only parameter that can be significantly changed by stress in Eq. (6.3) is μ_n i.e.

$$\pi_{R,Ohmic} = -\frac{\Delta I}{I}\frac{1}{dX} = -\frac{d\mu_n}{\mu_n}\frac{1}{dX}. \tag{6.9}$$

As already discussed in Chapter 2, the bulk Si PZR is due to stress induced changes in the effective mass, and hence in the mobility [14]. For $n-$type bulk Si, $-\frac{d\mu_n}{\mu_n}\frac{1}{dX} = -31.2 \times 10^{-11} Pa^{-1}$ [17], a value consistent with the PZR measured in the Ohmic regime here (see red dotted line in Fig. 6.7). This strongly suggests that the measured negative PZR is simply the bulk, $n-$type silicon effect.

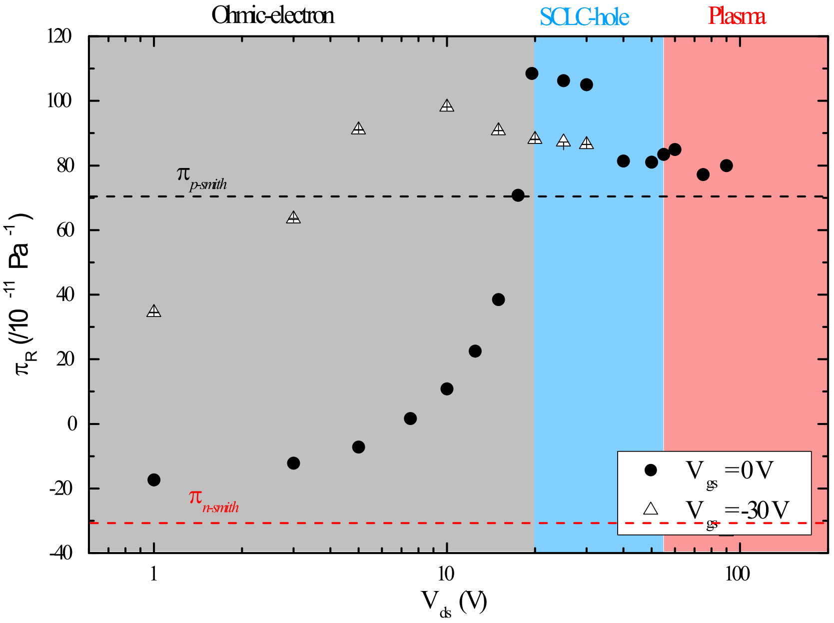

Fig. 6.7 The measured PZR versus applied voltage of the defect engineered device with $V_{gs} = -30\ V$ (triangles) and $V_{gs} = 0\ V$ (black dots).

In the unipolar SCLC regime, current is expressed as Eq. (6.7) and both μ_p and θ can be changed by stress as demonstrated in Chapter 4.

$$\pi_{R,SCLC} = -\frac{\Delta I}{I}\frac{1}{dX} = -\frac{d\mu_p}{\mu_p}\frac{1}{dX} - \frac{d\theta}{\theta}\frac{1}{dX} = -\frac{d\mu_p}{\mu_p}\frac{1}{dX} - [\frac{d\omega_e}{\omega_e}\frac{1}{dX} - \frac{d\omega_c}{\omega_c}\frac{1}{dX}]. \qquad (6.10)$$

The first term in Eq. (6.10), $-\frac{d\mu_p}{\mu_p}\frac{1}{dX} = +71.8 \times 10^{-11} Pa^{-1}$ [17] is the PZR for bulk, $p-$type silicon. The second term is zero as already discussed in section 4.4 since $\frac{d\omega_e}{\omega_e}\frac{1}{dX} = \frac{d\omega_c}{\omega_c}\frac{1}{dX}$ in the steady-state. In this case only p-type bulk Si PZR is expected in the unipolar SCLC regime and interestingly, the measured value is only slightly larger than the accepted $p-$type bulk value (see Fig. 6.7).

In the plasma regime the current is described in Eq. (6.8) where μ_n and μ_p are dependent on stress according to the bulk PZR effect. Assuming τ is a stress independent, the $\pi-$coefficient becomes:

$$\pi_{R,Plasma} = -\frac{\Delta I}{I}\frac{1}{dX} = -\frac{d\mu_n}{\mu_n}\frac{1}{dX} - \frac{d\mu_p}{\mu_p}\frac{1}{dX} = \pi_{n,bulk} + \pi_{p,bulk}, \qquad (6.11)$$

where $\pi_{n,bulk}$ is bulk $n-$type $\pi-$coefficient and $\pi_{p,bulk}$ is bulk $p-$type $\pi-$coefficient. Since the signs of $\pi_{n,bulk}$ and$\pi_{p,bulk}$ are opposite (see Table 2.2), Eq. (6.11) shows that in the plasma regime the bulk electron and hole PZR effect partially compensate one another. Taking for the purposes of this analysis the values measured here in the Ohmic regime and in the unipolar SCLC regime, one expects $\pi_{R,Plasma} = (-20+110)\times 10^{-11} = +90\times 10^{-11}\ Pa^{-1}$. This is very close to the measured value in the red regime in Fig. 6.7.

The apparently anomalous variation in π_R can therefore be well understood simply by considering the usual bulk PZR in combination with voltage-induced carrier type changes. To further verify this conclusion a negative gate voltage $V_{gs} = -30\ V$ is applied to force holes into the device and create a $p-$type channel. The measured DC PZR shown as triangles in Fig. 6.7 is now positive in the Ohmic regime as would be expected for majority hole conduction.

Anomalous PZR has been reported elsewhere and its origin is still under debate. Almost all published works relate anomalous PZR to the surface states [47, 29, 46, 48, 143, 144]. Lugstein's group used chemical deposition techniques to cover lightly doped $p-$type silicon nano-wires (SINWs) with different dielectrics and showed this modified the conduction type. Moreover this surface-chemistry-induced type change was correlated with a change in the sign of the PZR $\pi-$coefficient [48]. This is further evidence that the measured "anomalous" PZR is actually not anomalous at all, but rather depends only on the majority carrier in the device.

6.5 Impedance spectroscopy

To successfully simulate impedance spectroscopy results in Chapter 4 at least six trap types were needed to account for the continuous distribution of traps at the silicon/oxide interface. In the single trap type, defect engineered devices considered here, the impedance spectroscopy measurement are shown in Fig. 6.8. Decreasing C_0 and increasing G_0 as a function of frequency indicates that the device is in the SCLC limit in the presence of traps according to Kassing's model [74]. After divacancy defect implantation reduced conductance and increased capacitance are observed. The π_R of the pre-implanted (or initial) SCLC device is shown in Fig. 6.8(d) (dotted curve), two obvious peaks can be seen with a positive and a negative magnitude values. On the other hand, the π_C is shown in Fig. 6.8(c) (dotted curve) with a negative peak at relative low frequencies.

The π_C and π_R of defect engineered SCLC device are shown as solid lines in Fig. 6.8(c) and (d). For the π_R of defect engineered SCLC device, DC PZR is also presented and label as "DC" in Fig. 6.8(d). Interestingly, both π_R and π_C of defect engineered SCLC device have a similar shape to those measured on the initial, pre-implanted, SCLC device, except that the peak position is shifted downwards in frequency. According to the discussion in Chapter 4,

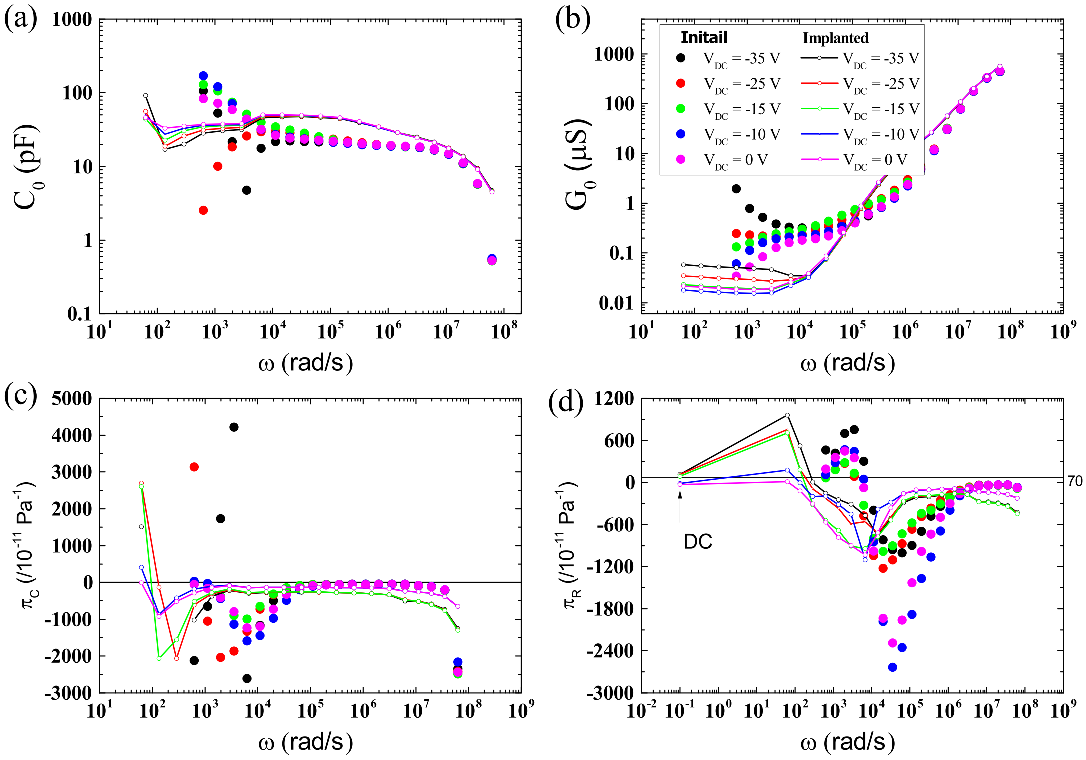

Fig. 6.8 Impedance spectroscopy of initial SCLC device (dot curves) and defect-engineered SCLC device (dot-line curves).(a) capacitance, (b) conductance, (c) PZC and (d) PZR is shown as a function of frequency under several V_{ds}.

the peak position of the piezo-response yields a rough estimated of the capture rate ω_c of the fast trap, so this observation indicates that ω_c decreases after the introduction of silicon divacancy defects.

However, it's still difficult to simultaneously model the frequency dependence of G_0, C_0, π_R and π_C of the defect engineered SCLC device using Kassing's model with a single set of defect parameters [73, 74]. This may be because the trap capture rate ω_c and emission rate ω_e used in Kassing's model are considered as constants in order to simplify the model (see Eq. (2.66) and (2.67)). However according to the Shockley-Read-Hall model, ω_c and ω_e are space- and time-dependent due to the space- and time-dependence of p_t and p (see Eq. (2.64) and (2.65)). This may explain the reason for difficulty of describing impedance spectroscopy using Kassing's one trap model, even though only one type of trap exists in the device layer.

Reproducibility of the piezo-response of defect-engineered devices

Fig. 6.9 shows an example of stress induced relative changes in (a) conductance $-\frac{dG_0}{G_0}$ and (b) capacitance $-\frac{dC_0}{C_0}$ of initial and defect engineered device at $\omega = 11000\ rad/s$. The initial (red dots) and implanted (black dots) raw data are shown as a function of time, and each raw data point is the mean value of ten measurements. The average value of these data points is the recorded as piezo-response at $\omega = 11000\ rad/s$, and they are shown as inserts in Fig. 6.9. The figure-of-merit (FOM) defined as the average value divided by the standard error, is 70 and 380 for $-\frac{dG_0}{G_0}$ of initial and implanted device respectively; and FOM is 1.6 and 154 for $-\frac{dC_0}{C_0}$ of initial and implanted device respectively. FOM reflects the confidence of measurement, the higher the FOM, the better the reproducibility of measurement. Interestingly, at $\omega = 11000$ rad/s, the defect engineered SCLC device shows a better reproducibility compare to initial SCLC device.

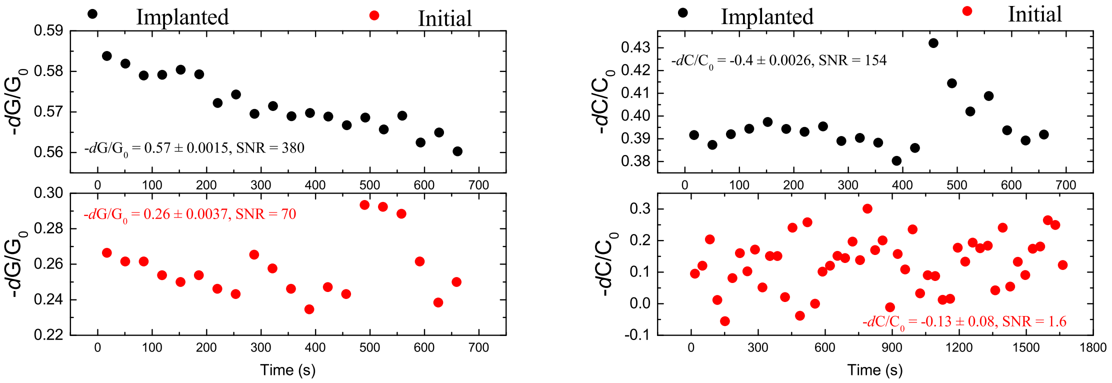

(a) FOM of PZR

(b) FOM of PZC

Fig. 6.9 Raw data of stress induced relative change in G_0 and C_0 at $\omega = 11000\ rad/s$. The mean value, standard deviation and FOM value of them are shown in the panels.

Fig. 6.10 presents FOM of (a) PZR and (b) PZC of initial and implanted device as a function of frequency. Symbols showing here are consistent with the Fig. 6.8, the dotted curves and dotted-line curves correspond to initial and implanted device results respectively, the colours correspond to different V_{DC}. FOM of PZR and PZC in defect engineered SCLC device are larger than that measured in initial SCLC device for almost all frequencies, especially at high frequencies. The better reproducibility of defect engineered SCLC device is probably due to the lower sensitivity of the volume defects to environmental fluctuations such as changes in humidity. It indicates that defect engineered SCLC devices might be better adapted for applications than SCLC devices whose functionality depends on interface defects.

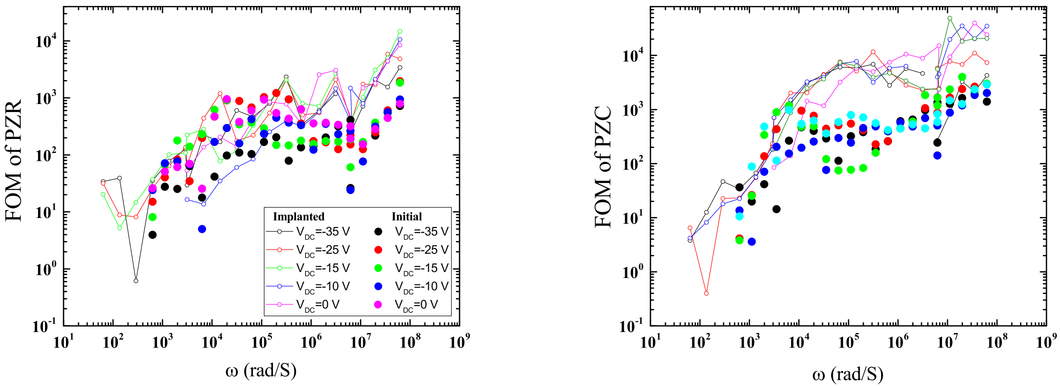

(a) Figure-of-merit (FOM) of PZR as a function of frequency.

(b) Figure-of-merit (FOM) of PZC as a function of frequency.

Fig. 6.10 Figure-of-merit of defect-engineered and initial SCLC device.

6.6 Conclusions: the emerging microscopic picture of anomalous steady-state PZR

In this chapter the PZR of defect-engineered SCLC devices was reported. Three voltage regimes are identified in the I-V characteristic. The electrons are majority carriers for low V_{ds} the $n-$type bulk silicon PZR is observed. With increasing V_{ds} holes are injected into the device and dominate current flow, so that conduction through the device is $p-$type and $p-$type bulk silicon PZR is measured. At high V_{ds} both holes and electrons are injected into the device and the measured PZR is shown to be a combination of $p-$ and $n-$type bulk silicon PZR. This observation indicates that the reported anomalous PZR is a misnomer: in fact the sign of the PZR follows that of the majority carrier. Impedance spectroscopy is on the defect engineered devices is also discussed, and despite the presence of a single dominant trap type it is still difficult to simultaneously model G_0, C_0, π_R and π_C using a single set of defect parameters in Kassing's one trap model. This may be because the trap capture rate (ω_c) and emission rate (ω_e) are space-dependent instead of being constants. In effect the data reveals the limitations of analytical models when trying to understand the small-signal behaviour of SCLCs.

Chapter 7

Conclusions and perspectives

7.1 Towards a better understanding of unusual piezo-resistance effects in nano-silicon

This thesis is a contribution to the study of giant, anomalous piezo-resistance in fully-depleted silicon micro- and nano-objects. To investigate the relationship between the giant or anomalous piezo-resistance and surface depletion in nano-structures, fully-depleted SOI devices are used in the thesis in which the surface depletion layer widths are larger than thickness of the device layer.

Impedance spectroscopy on these devices reveals a giant, anomalous PZR in the non-steady-state that reaches $-1100 \times 10^{-11}\ Pa^{-1}$ around measurement frequencies close to characteristic charge trapping rates. This technique is used to prove that the giant, anomalous PZR arises from stress-induced changes to trap capture and emission rates. Interestingly, in the steady-state limit only the usual bulk silicon PZR is observed, even in the presence of the stress dependent trapping dynamics. This observation supports the large number of reports of standard PZR in depleted silicon nano-objects, and further brings into question claims of steady-state giant PZR. The impedance spectroscopy method also reveals a quadrature response corresponding to a novel, giant PZC. The interpretation based on stress dependent trapping dynamics is reinforced by an observed voltage dependence of the PZR that can be attributed to the voltage dependence of phonon-assisted tunneling emission from the traps. The even symmetry of the giant PZR and the PZC in stress suggests that the electro-mechanically active traps are those associated with intrinsic Si/oxide interface defects. To test this the stress dependence of the pinned surface Fermi energy as a function of both compressive and tensile stress is measured using XPS mapping techniques. An observed even symmetry in stress-induced shifts of the pinned surface Fermi energy of oxidized

(001) silicon surfaces supports the conclusions drawn from the impedance spectroscopy measurements.

One difficulty encountered when trying to model the frequency dependence of the small-signal conductance, capacitance, PZR and PZC of SCLCs was the inability to reproduce the experimental curves with a small number of parameters. For this reason multiple trap types were artificially introduced. Attempts to produce samples that might more closely resemble available models, silicon divacancy defects were engineered into SCLC devices. While the impedance spectroscopy of these devices did not prove easier to model, unusual "anomalous" PZR measured using DC techniques was observed. It was shown that sign changes in the PZR are correlated with majority carrier type changes induced by the applied voltage in the SCLC regime.

7.2 Suggested future research directions

There are several possible interesting research directions that becomes possible thanks to the work reported on in this thesis.

1. The inability to simulate impedance spectroscopy curves in the SCLC limit in the presence of traps using approximate analytic models deserves revisiting since this type of transport is observed in many materials including semiconductor nano-structures, organic semiconductors and amorphous semiconductors. The problem is identified here as being likely due to the constant values of trapping and emission rates used in analytic models. In fact the original Shockley-Read-Hall model shows that trapping and emission rates are, in general, space and time dependent in the SCLC limit. Resolution of the full problem is likely to require a numerical methods.

2. To properly reveal the role of silicon divacancy defects in the anomalous PZR it would be interesting to cyclically remove and implant new defect. Removal can be achieved by annealing to 500°C [145] and re-implantation can be done on existing devices. A second possibility would be to photo-excite the devices with a sub-bandgap wavelength light (> 1200 *nm*) in order to block charge trapping at the defects. Because unusual PZR is related to stress dependent trapping dynamics, it would be interesting to explore photo-quenching effect in this way. Such experiments performed as a function of wavelength may help to identify the electro-mechanically active traps.

3. The stress dependence of surface Fermi level measurement on the silicon cantilever is significantly affected by the surface oxidation thickness (see Chapter 5). Surface

functionalization, for example hydrogenation with buffered HF could be used to test the effect of surface termination on the piezo-response, and may also be used to make an homogeneous surface oxide.

4. Mechanical spectroscopy: It has been shown that giant PZR occurs at measurement frequencies close to the characteristic charge trapping rates of fast traps. It would be also be interesting to explore the piezo-response of SCLCs in the presence of traps using a time varying mechanical stress and a constant applied DC voltage. One idea would be to design mechanical resonators whose resonant frequency is higher than the characteristic trapping rate. The resonator could then be driven at a frequency below, approximately equal to, or above the characteristic trapping rate. The piezo-response might reasonably be expected to be a strong function of mechanical frequency. Typical trapping rates estimated in this thesis for interface defects are around 10^6 rad/s and the divacancy defects are slight lower. While high, these frequencies are well within the range of typical MEMS resonant frequencies.

5. MEMS and micro-sensor based on silicon PZR are only suitable for temperatures below 200°C due to the relative low band gap energy (1.12 eV). For applications that need to work in high-temperature environments, materials with a larger band gap are under interesting. SiC is one of the most interesting material among them not only due to its large energy band gap (2.3 to 3.4 eV) but also due to its chemical inertness and large Young's modulus [146, 147]. So that study PZR of SiC nano-structure is another possible direction after this work.

References

[1] W. Thomson, "XIX. On the electro-dynamic qualities of metals:—Effects of magnetization on the electric conductivity of nickel and of iron," *Proceedings of the Royal Society of London*, vol. 8, pp. 546–550, 1857.

[2] J. W. Cookson, "Theory of the Piezo-Resistive Effect," *Physical Review*, vol. 47, no. 2, pp. 194–195, 1935.

[3] H. Tomlinson, "On the increase in resistance to the passage of an electric current produced on certain wires by stretching," *Proceedings of the Royal Society of London*, vol. 26, no. 179-184, pp. 401–410, 1878.

[4] H. Tomlinson, "I. The influence of stress and strain on the action of physical forces," *Philosophical Transactions of the Royal Society of London*, vol. 174, pp. 1–172, 1883.

[5] H. Rolnick, "Tension coefficient of resistance of metals," *Physical Review*, vol. 36, no. 3, pp. 506–512, 1930.

[6] M. Allen, "The Effect of Tension on the Electrical Resistance of Single Bismuth Crystals," *Physical Review*, vol. 42, no. 6, pp. 848–857, 1932.

[7] M. Allen, "The Effect of Tension on the Electrical Resistance of Single Antimony Crystals," *Physical Review*, vol. 43, no. 7, pp. 569–576, 1933.

[8] M. Allen, "The Tension Coefficients of Resistance of the Hexagonal Crystals Zinc and Cadmium," *Physical Review*, vol. 49, no. 3, pp. 248–253, 1936.

[9] M. Allen, "The Effect of Tension on the Electrical Resistance of Single Tetragonal Tin Crystals," *Physical Review*, vol. 52, no. 12, pp. 1246–1249, 1937.

[10] P. W. Bridgman, "Some Properties of Single Metal Crystals.," *Proceedings of the National Academy of Sciences of the United States of America*, vol. 10, no. 10, pp. 411–5, 1924.

[11] P. W. Bridgman, "General survey of the effects of pressure on the properties of matter," *Proceedings of the Physical Society*, vol. 41, no. 1, pp. 341–360, 1928.

[12] P. W. Bridgman, "The Resistance of 72 Elements, Alloys and Compounds to 100,000 Kg/Cm^2," *Proceedings of the American Academy of Arts and Sciences*, vol. 81, no. 4, p. 165, 1952.

[13] P. W. Bridgman, "The Electrical Resistance of Metals under Pressure," *Proceedings of the American Academy of Arts and Sciences*, vol. 52, no. 9, p. 573, 1917.

[14] A. C. H. Rowe, “Piezoresistance in silicon and its nanostructures,” *Journal of Materials Research*, vol. 29, no. 06, pp. 731–744, 2014.

[15] P. K. Stein, “1936-a banner year for strain gages and experimental stress analysis - An historical perspective,” *Experimental Techniques*, vol. 30, no. 1, pp. 23–41, 2006.

[16] J. Bardeen and W. Shockley, “Deformation potentials and mobilities in non-polar crystals,” *Physical Review*, vol. 80, no. 1, pp. 72–80, 1950.

[17] C. S. Smith, “Piezoresistance Effect in Germanium and Silicon,” *Physical Review*, vol. 94, no. 1, pp. 42–49, 1954.

[18] Y. Kanda, “A graphical representation of the piezoresistive coefficients in silicon,” *IEEE Trans. Electron Devices*, vol. ED-29, no. 1, pp. 64–70, 1982.

[19] A. Diebold, “The ITRS metrology roadmap,” in *2009 International Semiconductor Device Research Symposium*, pp. 1–2, IEEE, 2009.

[20] S. Thompson, M. Armstrong, C. Auth, S. Cea, R. Chau, G. Glass, T. Hoffman, J. Klaus, Z. Ma, B. Mcintyre, A. Murthy, B. Obradovic, L. Shifren, S. Sivakumar, S. Tyagi, T. Ghani, K. Mistry, M. Bohr, and Y. El-Mansy, “A Logic Nanotechnology Featuring Strained-Silicon,” *IEEE Electron Device Letters*, vol. 25, pp. 191–193, apr 2004.

[21] R. He and P. Yang, “Giant piezoresistance effect in silicon nanowires.,” *Nature nanotechnology*, vol. 1, no. 1, pp. 42–46, 2006.

[22] Y. Tanimoto, T. Toriyama, and S. Sugiyama, “Characteristics of Polycrystalline Si Nano Wire Piezoresistors,” *IEEJ Transactions on Sensors and Micromachines*, vol. 121, no. 4, pp. 209–214, 2001.

[23] T. Toriyama, D. Funai, and S. Sugiyama, “Piezoresistance measurement on single crystal silicon nanowires,” *Journal of Applied Physics*, vol. 93, no. 1, pp. 561–565, 2003.

[24] T. Toriyama, Y. Tanimoto, and S. Sugiyama, “Single crystal silicon nano-wire piezoresistors for mechanical sensors,” *Journal of Microelectromechanical Systems*, vol. 11, no. 5, pp. 605–611, 2002.

[25] M. M. McClarty, N. Jegenyes, M. Gaudet, C. Toccafondi, R. Ossikovski, F. Vaurette, S. Arscott, and A. C. H. Rowe, “Geometric and chemical components of the giant piezoresistance in silicon nanowires,” *Applied Physics Letters*, vol. 109, no. 2, p. 023102, 2016.

[26] K. Reck, J. Richter, O. Hansen, and E. V. Thomsen, “Piezoresistive effect in top-down fabricated silicon nanowires,” in *Proceedings of the IEEE International Conference on Micro Electro Mechanical Systems (MEMS)*, pp. 717–720, IEEE, 2008.

[27] K. Reck, J. Richter, O. Hansen, and E. V. Thomsen, “Increased Piezoresistive Effect in Crystalline and Polycrystalline Si Nanowires,” *Nsti Nanotech 2008, Vol 1, Technical Proceedings - Materials, Fabrication, Particles, and Characterization*, vol. 1, no. 100, pp. 920–923, 2008.

[28] A. Koumela, D. Mercier, C. Dupré, G. Jourdan, C. Marcoux, E. Ollier, S. T. Purcell, and L. Duraffourg, "Piezoresistance of top-down suspended Si nanowires," *Nanotechnology*, vol. 22, no. 39, p. 395701, 2011.

[29] Y. Yang and X. Li, "Giant piezoresistance of p-type nano-thick silicon induced by interface electron trapping instead of 2D quantum confinement," *Nanotechnology*, vol. 22, no. 1, p. 015501, 2011.

[30] J. X. Cao, X. G. Gong, and R. Q. Wu, "Giant piezoresistance and its origin in Si(111) nanowires: First-principles calculations," *Physical Review B - Condensed Matter and Materials Physics*, vol. 75, no. 23, pp. 3–6, 2007.

[31] D. Shiri, Y. Kong, A. Buin, and M. P. Anantram, "Strain induced change of bandgap and effective mass in silicon nanowires," *Applied Physics Letters*, vol. 93, no. 7, p. 073114, 2008.

[32] K. Nakamura, D. V. Dao, B. T. Tung, T. Toriyama, and S. Sugiyama, "Piezoresistive effect in silicon nanowires - A comprehensive analysis based on first-principles calculations," in *20th Anniversary MHS 2009 and Micro-Nano Global COE - 2009 International Symposium on Micro-NanoMechatronics and Human Science*, pp. 38–43, IEEE, 2009.

[33] P. W. Leu, A. Svizhenko, and K. Cho, "Ab initio calculations of the mechanical and electronic properties of strained Si nanowires," *Physical Review B - Condensed Matter and Materials Physics*, vol. 77, no. 23, p. 235305, 2008.

[34] G. Dorda, "Effective mass change of electrons in silicon inversion layers observed by piezoresistance," *Applied Physics Letters*, vol. 17, no. 9, pp. 406–408, 1970.

[35] F. G. Allen and G. W. Gobeli, "Work function, photoelectric threshold, and surface states of atomically clean silicon," *Physical Review*, vol. 127, no. 1, pp. 150–158, 1962.

[36] S. Sze and K. K. Ng, *Physics of Semiconductor Devices*. Hoboken, NJ, USA: John Wiley & Sons, Inc., 2006.

[37] A. C. H. Rowe, "Silicon nanowires feel the pinch," *Nature Nanotechnology*, vol. 3, no. 6, pp. 311–312, 2008.

[38] J. S. Milne, A. C. H. Rowe, S. Arscott, and C. Renner, "Giant piezoresistance effects in silicon nanowires and microwires," *Physical Review Letters*, vol. 105, no. 22, pp. 1–4, 2010.

[39] E. Mile, G. Jourdan, I. Bargatin, S. Labarthe, C. Marcoux, P. Andreucci, S. Hentz, C. Kharrat, E. Colinet, and L. Duraffourg, "In-plane nanoelectromechanical resonators based on silicon nanowire piezoresistive detection," *Nanotechnology*, vol. 21, no. 16, p. 165504, 2010.

[40] T. Barwicz, L. Klein, S. J. Koester, and H. Hamann, "Silicon nanowire piezoresistance: Impact of surface crystallographic orientation," *Applied Physics Letters*, vol. 97, no. 2, p. 023110, 2010.

[41] U. Kumar Bhaskar, T. Pardoen, V. Passi, and J. P. Raskin, “Piezoresistance of nanoscale silicon up to 2 GPa in tension,” *Applied Physics Letters*, vol. 102, no. 3, p. 14102, 2013.

[42] H. P. Phan, T. Kozeki, T. Dinh, T. Fujii, A. Qamar, Y. Zhu, T. Namazu, N. T. Nguyen, and D. V. Dao, “Piezoresistive effect of p-type silicon nanowires fabricated by a top-down process using FIB implantation and wet etching,” *RSC Advances*, vol. 5, no. 100, pp. 82121–82126, 2015.

[43] M. M. McClarty, N. Jegenyes, M. Gaudet, C. Toccafondi, R. Ossikovski, F. Vaurette, S. Arscott, and A. C. H. Rowe, “Geometric and chemical components of the giant piezoresistance in silicon nanowires,” *Applied Physics Letters*, vol. 109, no. 2, p. 023102, 2016.

[44] M. V. Fischetti, “Generation of positive charge in silicon dioxide during avalanche and tunnel electron injection,” *Journal of Applied Physics*, vol. 57, no. 8, pp. 2860–2879, 1985.

[45] E. H. Nicollian and J. R. Brews, *MOS (metal oxide semiconductor) physics and technology*. New York, US: John Wiley & Sons Inc, 1982.

[46] A. Lugstein, M. Steinmair, A. Steiger, H. Kosina, and E. Bertagnolli, “Anomalous piezoresistance effect in ultrastrained silicon nanowires,” *Nano Letters*, vol. 10, no. 8, pp. 3204–3208, 2010.

[47] H. Jang, J. Kim, M. S. Kim, J. H. Cho, H. Choi, and J. H. Ahn, “Observation of the inverse giant piezoresistance effect in silicon nanomembranes probed by ultrafast terahertz spectroscopy,” *Nano Letters*, vol. 14, no. 12, pp. 6942–6948, 2014.

[48] K. Winkler, E. Bertagnolli, and A. Lugstein, “Origin of anomalous piezoresistive effects in VLS grown Si nanowires,” *Nano Letters*, vol. 15, no. 3, pp. 1780–1785, 2015.

[49] P. Neuzil, C. C. Wong, and J. Reboud, “Electrically Controlled Giant Piezoresistance in Silicon Nanowires,” *Nano Letters*, vol. 10, no. 4, pp. 1248–1252, 2010.

[50] T. Barwicz, L. Klein, S. J. Koester, and H. Hamann, “Silicon nanowire piezoresistance: Impact of surface crystallographic orientation,” *Applied Physics Letters*, vol. 97, no. 2, p. 023110, 2010.

[51] J. S. Milne, I. Favorskiy, A. C. H. Rowe, S. Arscott, and C. Renner, “Piezoresistance in Silicon at Uniaxial Compressive Stresses up to 3 GPa,” *Physical Review Letters*, vol. 108, no. 25, p. 256801, 2012.

[52] P. J. Dobson, “Physical Properties of Crystals – Their Representation by Tensors and Matrices,” *Physics Bulletin*, vol. 36, no. 12, pp. 506–506, 1985.

[53] L. Onsager, “Reciprocal Relations in Irreversible Processes. I.,” *Physical Review*, vol. 37, no. 4, pp. 405–426, 1931.

[54] M. H. Bao, *Micro mechanical transducers: pressure sensors, accelerometers, and gyroscopes*, vol. 8. 2000.

[55] W. P. Mason and R. N. Thurston, “Use of Piezoresistive Materials in the Measurement of Displacement, Force, and Torque,” *The Journal of the Acoustical Society of America*, vol. 29, no. 10, pp. 1096–1101, 1957.

[56] J. J. Wortman and R. A. Evans, “Young’s modulus, shear modulus, and poisson’s ratio in silicon and germanium,” *Journal of Applied Physics*, vol. 36, no. 1, pp. 153–156, 1965.

[57] C. Herring and E. Vogt, “Transport and Deformation-Potential Theory for Many-Valley Semiconductors with Anisotropic Scattering,” *Physical Review*, vol. 101, no. 3, pp. 944–961, 1956.

[58] J. E. Aubrey, W. Gubler, T. Henningsen, and S. H. Koenig, “Piezoresistance and Piezo-Hall-Effect in n-type Silicon,” *Physical Review*, vol. 130, no. 5, pp. 1667–1670, 1963.

[59] C. Herring, “Theory of the Thermoelectric Power of Semiconductors,” *Physical Review*, vol. 96, no. 5, pp. 1163–1187, 1954.

[60] E. N. Adams, “Elastoresistance in p-Type Ge and Si,” *Physical Review*, vol. 96, no. 3, pp. 803–804, 1954.

[61] X. F. Fan, L. F. Register, B. Winstead, M. C. Foisy, W. Chen, X. Zheng, B. Ghosh, and S. K. Banerjee, “Hole mobility and thermal velocity enhancement for uniaxial stress in Si up to 4 GPa,” *IEEE Transactions on Electron Devices*, vol. 54, no. 2, pp. 291–296, 2007.

[62] J. . Richter, J. . Pedersen, M. . Brandbyge, E. V. Thomsen, and O. Hansen, “Piezoresistance in p-type silicon revisited,” *Journal of Applied Physics*, vol. 104, no. 2, p. 23715, 2008.

[63] Y. Ohmura, “Piezoresistance effect in p-type Si,” *Physical Review B*, vol. 42, no. 14, pp. 9178–9181, 1990.

[64] K. Suzuki, H. Hasegawa, and Y. Kanda, “Origin of the Linear and Nonlinear Piezoresistance Effects in p-Type Silicon,” *Japanese Journal of Applied Physics*, vol. 23, no. Part 2, No. 11, pp. L871–L874, 1984.

[65] R. Coquand, M. Casse, S. Barraud, D. Cooper, V. Maffini-Alvaro, M. P. Samson, S. Monfray, F. Boeuf, G. Ghibaudo, O. Faynot, and T. Poiroux, “Strain-induced performance enhancement of trigate and omega-gate nanowire FETs scaled down to 10-nm width,” *IEEE Transactions on Electron Devices*, vol. 60, no. 2, pp. 727–732, 2013.

[66] C. D. Child, “Discharge From Hot Cao,” *Physical Review (Series I)*, vol. 32, no. 5, pp. 492–511, 1911.

[67] J. Shao and G. Wright, “Characteristics of the space-charge-limited dielectric diode at very high frequencies,” *Solid-State Electronics*, vol. 3, no. 3-4, pp. 291–303, 1961.

[68] A. Many and G. Rakavy, “Theory of Transient Space-Charge-Limited Currents in Solids in the Presence of Trapping,” *Physical Review*, vol. 126, no. 6, pp. 1980–1988, 1962.

[69] D. Dascalu, “Small-signal Theory of Space-charge-limited Diodes†,” *International Journal of Electronics*, vol. 21, no. 2, pp. 183–200, 1966.

[70] G. Wright, “Transit time effects in the space-charge-limited silicon microwave diode,” *Solid-State Electronics*, vol. 9, no. 1, pp. 1–6, 1966.

[71] S. Chisholm and Chuan-Sung Yeh, “High-frequency admittance of n-v-n space-charge-limited current (SCLC) solid-state devices,” *Proceedings of the IEEE*, vol. 56, no. 12, pp. 2178–2180, 1968.

[72] M. A. Nicolet, H. R. Bilger, and R. J. J. Zijlstra, “Noise in Single and Double Injection Currents in Solids (I),” *physica status solidi (b)*, vol. 70, no. 1, pp. 9–45, 1975.

[73] R. Kassing and E. Kähler, “The small signal behavior of SCLC-diodes with deep traps,” *Solid State Communications*, vol. 15, no. 3, pp. 673–676, 1974.

[74] R. Kassing, “Calculation of the frequency dependence of the admittance of SCLC diodes,” *Physica Status Solidi (a)*, vol. 28, no. 1, pp. 107–117, 1975.

[75] J. M. Alison and R. M. Hill, “A model for bipolar charge transport, trapping and recombination in degassed crosslinked polyethene,” *Journal of Physics D: Applied Physics*, vol. 27, no. 6, pp. 1291–1299, 1994.

[76] S. L. Roy, P. Segur, G. Teyssedre, and C. Laurent, “Description of bipolar charge transport in polyethylene using a fluid model with a constant mobility: model prediction,” *Journal of Physics D: Applied Physics*, vol. 37, no. 2, pp. 298–305, 2004.

[77] Á. Pitarch, G. Garcia-Belmonte, J. Bisquert, and H. J. Bolink, “Impedance of space-charge-limited currents in organic light-emitting diodes with double injection and strong recombination,” *Journal of Applied Physics*, vol. 100, no. 8, p. 84502, 2006.

[78] P. A. Leighton, “Electronic Processes in Ionic Crystals (Mott, N. F.; Gurney, R. W.),” *Journal of Chemical Education*, vol. 18, no. 5, p. 249, 1941.

[79] W. Shockley and W. T. Read, “Statistics of the Recombinations of Holes and Electrons,” *Physical Review*, vol. 87, no. 5, pp. 835–842, 1952.

[80] P. N. Murgatroyd, “Theory of space-charge-limited current enhanced by Frenkel effect,” *Journal of Physics D: Applied Physics*, vol. 3, no. 2, p. 308, 1970.

[81] J. Frenkel, “On Pre-Breakdown Phenomena in Insulators and Electronic Semi-Conductors,” *Physical Review*, vol. 54, no. 8, pp. 647–648, 1938.

[82] O. Mitrofanov and M. Manfra, “Poole-Frenkel electron emission from the traps in AlGaN/GaN transistors,” *Journal of Applied Physics*, vol. 95, no. 11, pp. 6414–6419, 2004.

[83] S. D. Ganichev, E. Ziemann, W. Prettl, I. N. Yassievich, A. A. Istratov, and E. R. Weber, “Distinction between the Poole-Frenkel and tunneling models of electric-field-stimulated carrier emission from deep levels in semiconductors,” *Physical Review B*, vol. 61, no. 15, pp. 10361–10365, 2000.

[84] J. B. Lasky, “Wafer bonding for silicon-on-insulator technologies,” *Applied Physics Letters*, vol. 48, no. 1, pp. 78–80, 1986.

[85] W. Kern, “The Evolution of Silicon Wafer Cleaning Technology,” *Journal of The Electrochemical Society*, vol. 137, no. 6, p. 1887, 1990.

[86] J. F. Ziegler, M. D. Ziegler, and J. P. Biersack, “SRIM - The stopping and range of ions in matter (2010),” *Nuclear Instruments and Methods in Physics Research, Section B: Beam Interactions with Materials and Atoms*, vol. 268, no. 11-12, pp. 1818–1823, 2010.

[87] W. K. Hofker, “Implantation of boron in silicon,” *Microelectronics Reliability*, vol. 15, no. 3, p. 189, 1976.

[88] G. L. Pearson and J. Bardeen, “Electrical Properties of Pure Silicon and Silicon Alloys Containing Boron and Phosphorus,” *Physical Review*, vol. 75, no. 5, pp. 865–883, 1949.

[89] K. Nishiyama, M. Arai, and N. Watanabe, “Radiation Annealing of Boron-Implanted Silicon with a Halogen Lamp,” *Japanese Journal of Applied Physics*, vol. 19, no. 10, pp. L563–L566, 1980.

[90] R. B. Fair, J. J. Wortman, and J. Liu, “Modeling Rapid Thermal Diffusion of Arsenic and Boron in Silicon,” *Journal of The Electrochemical Society*, vol. 131, no. 10, p. 2387, 1984.

[91] H. Card, “Aluminum—Silicon Schottky barriers and ohmic contacts in integrated circuits,” *IEEE Transactions on Electron Devices*, vol. 23, no. 6, pp. 538–544, 1976.

[92] F. Laermer and A. Urban, “Challenges, developments and applications of silicon deep reactive ion etching,” *Microelectronic Engineering*, vol. 67-68, pp. 349–355, 2003.

[93] C. Chang, Y. Fang, and S. Sze, “Specific contact resistance of metal-semiconductor barriers,” *Solid-State Electronics*, vol. 14, no. 7, pp. 541–550, 1971.

[94] J. Suhling and R. Jaeger, “Silicon piezoresistive stress sensors and their application in electronic packaging,” *IEEE Sensors Journal*, vol. 1, no. 1, pp. 14–30, 2001.

[95] S. Timoshenko and J. N. J. N. Goodier, *Theory of elasticity.* New York: McGraw-Hill, 3rd ed. ed., 1970.

[96] D. Chong, W. Lee, B. Lim, J. Pang, and T. Low, “Mechanical characterization in failure strength of silicon dice,” in *The Ninth Intersociety Conference on Thermal and Thermomechanical Phenomena In Electronic Systems (IEEE Cat. No.04CH37543)*, vol. 2, pp. 203–210, IEEE, 2004.

[97] E. Oberg, F. D. Jones, H. L. Horton, H. H. Ryffel, and C. J. Mccauley, *Machinery's Handbook 29 th Edition*. 2012.

[98] A. Sagar, "Piezoresistance in n-Type GaAs," *Physical Review*, vol. 112, no. 5, pp. 1533–1533, 1958.

[99] T. Toriyama and S. Sugiyama, "Analysis of piezoresistance in p-type silicon for mechanical sensors," *Journal of Microelectromechanical Systems*, vol. 11, no. 5, pp. 598–604, 2002.

[100] P. N. Murgatroyd, "Theory of space-charge-limited current enhanced by Frenkel effect," *Journal of Physics D: Applied Physics*, vol. 3, no. 2, p. 308, 1970.

[101] G. Papaioannou, V. Ioannou-Sougleridis, S. Cristoloveanu, and C. Jaussaud, "Photoinduced current transient spectroscopy in silicon-on-insulator films formed by oxygen implantation," *Journal of Applied Physics*, vol. 65, no. 9, pp. 3725–3727, 1989.

[102] Y. Nishi, K. Tanaka, and A. Ohwada, "Study of Silicon-Silicon Dioxide Structure by Electron Spin Resonance II," *Japanese Journal of Applied Physics*, vol. 11, no. 1, pp. 85–91, 1972.

[103] E. H. Poindexter, G. J. Gerardi, M. Rueckel, P. J. Caplan, N. M. Johnson, and D. K. Biegelsen, "Electronic traps and P b centers at the Si/SiO2 interface: Band-gap energy distribution," *Journal of Applied Physics*, vol. 56, no. 10, pp. 2844–2849, 1984.

[104] Y. S. Choi, T. Nishida, and S. E. Thompson, "Impact of mechanical stress on direct and trap-assisted gate leakage currents in p -type silicon metal-oxide-semiconductor capacitors," *Applied Physics Letters*, vol. 92, no. 17, pp. 1–4, 2008.

[105] A. Toda, S. Fujieda, K. Kanamori, J. Suzuki, K. Kuroyanagi, N. Kodama, D. Yasuhide, and T. Nishizaka, "Impact of mechanical stress on interface trap generation in flash eeproms," in *Reliability Physics Symposium, 2005. Proceedings. 43rd Annual. 2005 IEEE International*, pp. 250–256, 2005.

[106] G. Kovačević and B. Pivac, "Structure, defects, and strain in silicon-silicon oxide interfaces," *Journal of Applied Physics*, vol. 115, no. 4, p. 043531, 2014.

[107] A. Hamada, "Hot-Electron Trapping Activation Energy in PMOSFET ' s Under Mechanical Stress," *IEEE Electron Device Letters*, vol. 15, no. 9214885, pp. 31–32, 1994.

[108] E. H. Poindexter, "MOS interface states: overview and physicochemical perspective," *Semiconductor Science and Technology*, vol. 4, no. 12, pp. 961–969, 1989.

[109] B. J. O'Sullivan, P. K. Hurley, C. Leveugle, and J. H. Das, "Si(100)-SiO2 interface properties following rapid thermal processing," *Journal of Applied Physics*, vol. 89, no. 7, pp. 3811–3820, 2001.

[110] P. M. Lenahan and P. V. Dressendorfer, "Effect of bias on radiation-induced paramagnetic defects at the silicon-silicon dioxide interface," *Applied Physics Letters*, vol. 41, no. 6, pp. 542–544, 1982.

[111] P. M. Lenahan and P. V. Dressendorfer, “An electron spin resonance study of radiation-induced electrically active paramagnetic centers at the Si/SiO2 interface,” *Journal of Applied Physics*, vol. 54, no. 3, pp. 1457–1460, 1983.

[112] P. M. Lenahan and P. V. Dressendorfer, “Hole traps and trivalent silicon centers in metal/oxide/silicon devices,” *Journal of Applied Physics*, vol. 55, no. 10, pp. 3495–3499, 1984.

[113] W. Low and M.Schieber, *Handbook of Applied Solid State Spectroscopy*. Boston, MA: Springer US, 2006.

[114] F. J. Himpsel, G. Hollinger, and R. A. Pollak, “Determination of the Fermi-level pinning position at Si(111) surfaces,” *Physical Review B*, vol. 28, no. 12, pp. 7014–7018, 1983.

[115] M. Seah and W. Dench, “Quantitative Electron Spectroscopy of Surfaces :,” *Surface And Interface Analysis*, vol. 1, no. 1, pp. 2–11, 1979.

[116] S. Ganesan, A. Maradudin, and J. Oitmaa, “A lattice theory of morphic effects in crystals of the diamond structure,” *Annals of Physics*, vol. 56, no. 2, pp. 556–594, 1970.

[117] E. Anastassakis, A. Pinczuk, E. Burstein, F. Pollak, and M. Cardona, “Effect of static uniaxial stress on the Raman spectrum of silicon,” *Solid State Communications*, vol. 88, no. 11-12, pp. 1053–1058, 1993.

[118] E. Anastassakis, A. Cantarero, and M. Cardona, “Piezo-Raman measurements and anharmonic parameters in silicon and diamond,” *Physical Review B*, vol. 41, no. 11, pp. 7529–7535, 1990.

[119] I. De Wolf, H. E. Maes, and S. K. Jones, “Stress measurements in silicon devices through Raman spectroscopy: Bridging the gap between theory and experiment,” *Journal of Applied Physics*, vol. 79, no. 9, pp. 7148–7156, 1996.

[120] J. J. Wortman and R. A. Evans, “Young’s Modulus, Shear Modulus, and Poisson’s Ratio in Silicon and Germanium,” *Journal of Applied Physics*, vol. 36, no. 1, pp. 153–156, 1965.

[121] E. Landemark, C. J. Karlsson, Y. Chao, and R. I. G. Uhrberg, “Core-level spectroscopy of the clean Si(001) surface: Charge transfer within asymmetric dimers of the 2×1 and c (4×2) reconstructions,” *Physical Review Letters*, vol. 69, no. 10, pp. 1588–1591, 1992.

[122] J. Gallet, M. G. Silly, M. E. Kazzi, F. Bournel, F. Sirotti, and F. Rochet, “Chemical and kinetic insights into the Thermal Decomposition of an Oxide Layer on Si(111) from Millisecond Photoelectron Spectroscopy,” *Scientific Reports*, vol. 7, no. 1, p. 14257, 2017.

[123] R. T. Sanderson, “Bond energies,” *Physical & Theoretical Chemistry*, vol. 28, no. December 1965, pp. 1553–1565, 1965.

[124] T. Eickhoff, V. Medicherla, and W. Drube, “Final state contribution to the Si 2p binding energy shift in SiO2/Si(1 0 0),” *Journal of Electron Spectroscopy and Related Phenomena*, vol. 137-140, no. SPEC. ISS., pp. 85–88, 2004.

[125] I. Jiménez and J. L. Sacedón, “Influence of Si oxidation methods on the distribution of suboxides at Si/SiO2 interfaces and their band alignment: A synchrotron photoemission study,” *Surface Science*, vol. 482-485, no. PART 1, pp. 272–278, 2001.

[126] M. Hochella and A. Carim, “A reassessment of electron escape depths in silicon and thermally grown silicon dioxide thin films,” *Surface Science*, vol. 197, no. 3, pp. L260–L268, 1988.

[127] M. Morita, T. Ohmi, E. Hasegawa, M. Kawakami, and M. Ohwada, “Growth of native oxide on a silicon surface,” *Journal of Applied Physics*, vol. 68, no. 3, pp. 1272–1281, 1990.

[128] M. Sohgawa, M. Agata, T. Kanashima, K. Yamashita, K. Eriguchi, A. Fujimoto, and M. Okuyama, “Nondestructive and contactless monitoring technique of Si surface stress by photoreflectance,” *Japanese Journal of Applied Physics, Part 1: Regular Papers and Short Notes and Review Papers*, vol. 40, no. 4 B, pp. 2844–2848, 2001.

[129] E. Chason, S. T. Picraux, J. M. Poate, J. O. Borland, M. I. Current, T. Diaz de la Rubia, D. J. Eaglesham, O. W. Holland, M. E. Law, C. W. Magee, J. W. Mayer, J. Melngailis, and A. F. Tasch, “Ion beams in silicon processing and characterization,” *Journal of Applied Physics*, vol. 81, no. 10, pp. 6513–6561, 1997.

[130] S. R. Christopoulos, H. Wang, A. Chroneos, C. A. Londos, E. N. Sgourou, and U. Schwingenschlögl, “VV and VO2 defects in silicon studied with hybrid density functional theory,” *Journal of Materials Science: Materials in Electronics*, vol. 26, no. 3, pp. 1568–1571, 2015.

[131] J. W. Corbett and G. D. Watkins, “Silicon Divacancy and its Direct Production by Electron Irradiation,” *Physical Review Letters*, vol. 7, no. 8, pp. 314–316, 1961.

[132] D. Hall, D. Wood, N. Murray, J. Gow, A. Chroneos, and A. Holland, “In situ trap properties in CCDs: the donor level of the silicon divacancy,” *Journal of Instrumentation*, vol. 12, no. 01, pp. 01025–01025, 2017.

[133] G. D. Watkins and J. W. Corbett, “Defects in irradiated silicon: Electron paramagnetic resonance of the divacancy,” *Physical Review*, vol. 138, no. 2A, 1965.

[134] D. K. Schroder, *Semiconductor material and device characterization*. John Wiley & Sons Ltd, 1998.

[135] D. V. Lang, X. Chi, T. Siegrist, A. M. Sergent, and A. P. Ramirez, “Bias-Dependent Generation and Quenching of Defects in Pentacene,” *Physical Review Letters*, vol. 93, no. 7, p. 076601, 2004.

[136] A. Salleo, F. Endicott, and R. A. Street, “Reversible and irreversible trapping at room temperature in poly(thiophene) thin-film transistors,” *Applied Physics Letters*, vol. 86, no. 26, pp. 1–3, 2005.

[137] D. Knipp, R. A. Street, A. Völkel, and J. Ho, “Pentacene thin film transistors on inorganic dielectrics: Morphology, structural properties, and electronic transport,” *Journal of Applied Physics*, vol. 93, no. 1, pp. 347–355, 2003.

[138] R. Schmechel and H. von Seggern, “Electronic traps in organic transport layers,” *physica status solidi (a)*, vol. 201, no. 6, pp. 1215–1235, 2004.

[139] A. Rose, “Space-Charge-Limited Currents in Solids,” *Physical Review*, vol. 97, no. 6, pp. 1538–1544, 1955.

[140] M. A. Lampert, “Double injection in insulators,” *Physical Review*, vol. 125, no. 1, pp. 126–141, 1962.

[141] M. A. Lampert and A. Rose, “Volume-Controlled, Two-Carrier currents in solids: The Injected Plasma Case,” *Physical Review*, vol. 121, no. 1, pp. 26–37, 1961.

[142] G. Masetti, M. Severi, and S. Solmi, “Modeling of Carrier Mobility Against Carrier Concentration in Arsenic-, Phosphorus-, and Boron-Doped Silicon,” *IEEE Transactions on Electron Devices*, vol. 30, no. 7, pp. 764–769, 1983.

[143] Y. Zhang, X. Liu, C. Ru, Y. L. Zhang, L. Dong, and Y. Sun, “Piezoresistivity characterization of synthetic silicon nanowires using a MEMS Device,” *Journal of Microelectromechanical Systems*, vol. 20, no. 4, pp. 959–967, 2011.

[144] Y. Zhang, X. Liu, C. Ru, Y. L. Zhang, L. Dong, and Y. Sun, “Piezoresistivity characterization of synthetic silicon nanowires using a MEMS Device,” *Journal of Microelectromechanical Systems*, vol. 20, no. 4, pp. 959–967, 2011.

[145] R. Poirier, V. Avalos, S. Dannefaer, F. Schiettekatte, and S. Roorda, “Divacancies in proton irradiated silicon: Comparison of annealing mechanisms studied with infrared spectroscopy and positron annihilation,” *Nuclear Instruments and Methods in Physics Research Section B: Beam Interactions with Materials and Atoms*, vol. 206, pp. 85–89, 2003.

[146] M. Mehregany, C. Zorman, N. Rajan, and Chien Hung Wu, “Silicon carbide MEMS for harsh environments,” *Proceedings of the IEEE*, vol. 86, no. 8, pp. 1594–1609, 1998.

[147] H. P. Phan, D. V. Dao, K. Nakamura, S. Dimitrijev, and N.-T. Nguyen, “The Piezoresistive Effect of SiC for MEMS Sensors at High Temperatures: A Review,” *Journal of Microelectromechanical Systems*, vol. 24, no. 6, pp. 1663–1677, 2015.

[148] J. C. Balland, J. P. Zielinger, C. Noguet, and M. Tapiero, “Investigation of deep levels in high-resistivity bulk materials by photo-induced current transient spectroscopy. I. Review and analysis of some basic problems,” 1986.

[149] J. C. Balland, J. P. Zielinger, M. Tapiero, J. G. Gross, and C. Noguet, “Investigation of deep levels in high-resistivity bulk materials by photo-induced current transient spectroscopy. II. Evaluation of various signal processing methods,” 1986.

[150] J. P. Zielinger, B. Pohoryles, J. C. Balland, J. G. Gross, and A. Coret, “Investigation of deep levels in PbI2 by photoinduced current transient spectroscopy,” *Journal of Applied Physics*, vol. 57, no. 2, pp. 293–301, 1985.

[151] D. V. Lang, “Deep-level transient spectroscopy: A new method to characterize traps in semiconductors,” *Journal of Applied Physics*, vol. 45, no. 7, pp. 3023–3032, 1974.

Appendix A

PICTS spectroscopy

Photo-induced current transient spectroscopy (PICTS) is a variation of deep level transient spectroscopy (DLTS) used to investigate deep level traps in high-resistivity materials and devices[101, 148–150]. By utilizing a periodic above band gap optical excitation to generate electron-hole pairs, traps are readily filled by photo-carriers. Immediately after the end of the optical excitation, a sharp current drop due to recombination is observed, followed by a slower delay due to trapped charge carrier emission. By monitoring the detrapping of trapped charge carriers as a function of temperature, important parameters about the traps present can be determined. The current transient due to detrapping (of holes) is given by:

$$i(t) = qAE\mu_p\tau_p\frac{p_t(0)}{\tau_t} + i(t_\infty) \tag{A.1}$$

where q is the electronic charge, A is a constant related to the illuminated sample surface and the penetration depth of the photoexcitation, E the applied electric field, μ_p the hole mobility, τ_p the recombination lifetime of free holes, $p_t(0)$ the initial density of filled traps, τ_t the thermal emission time constant, and $i(t_\infty)$ the quiescent current (i.e., the dark current). Following the approach used in DLTS [151], a double boxcar weighting function is applied to the current transient such that the current difference at times t_1 and t_2 is considered:

$$i(t_1) - i(t_2) = (qAE\mu_p\tau_p\frac{p_t(0)}{\tau_t})[exp(-\frac{t_1}{\tau_t}) - exp(-\frac{t_2}{\tau_t})] \tag{A.2}$$

By differentiating Eq. A.2 with respect to τ_t, one can easily show that the difference $i(t_1) - i(t_2)$ goes through a maximum when $\tau_t = \tau_M$ where τ_M is determined according to:

$$\frac{t_2 - t_1}{\tau_M} = ln\left|\frac{t_2 - \tau_M}{t_1 - \tau_M}\right| \tag{A.3}$$

In PICTS as in DLTS, the maximum current difference occurring when Eq. A.3 holds, is measured as a function of temperature, and a global "maximum of maximum differences" occurring at a temperature T_M may be observed. In this case the trap activation energy along with its capture cross section can be determined using Shockley-Read-Hall (SRH) theory [79]. In SRH theory, the thermal emission time constant follows an Arrhenius-type dependence:

$$e_p = \frac{1}{\tau_t} = \sigma_C v_{th} N_V exp(\frac{E_T - E_V}{k_B T}) \tag{A.4}$$

where e_p is the hole emission rate, σ_C the capture cross section, v_{th} the thermal velocity of holes, N_V the effective density of states in the valence band, $E_T - E_V$ the trap energy level with respect to the top of the valence band, and k_B the Boltzmann constant. By determining τ_M (and the corresponding maximum emission rate, $e_M = 1/\tau_M$) at the temperature T_M for a series of different t_1 and t_2 times (keeping t_2/t_1 constant) and plotting $ln(e_M/T_M^2)$ versus $1/T_M$, one can calculate $E_T - E_V$ from the slope and σ_C from the intercept for a specific trap level.

PICTS Experimental setup

Illumination of the sample was provided by a 940 nm commercial high speed emitting diode with a rise and fall time of 20 ns. A signal generator (Agilent 33210A) was used to apply a 100 ms pulse to the emitting diode at a rate of 1 Hz, which delivered an optical pulse of approximately 55 mW to the sample. In addition, the sample bias, V_{ds}, was fixed throughout the whole PICTS temperature scan. The PICTS measurements were performed using a custom built DLTS setup with the temperature ramped from 86 K to 300 K in 2 K increments. Individual current transients measured using a current amplifier (SR570) at each temperature step was averaged up to 30 transients, improving the signal to noise ratio (SNR) proportional to $\sqrt{N}$ transients. The averaged current transients were then recorded by a computer for further double boxcar analysis.

PICTS measurements

Fig. A.1(a) shows the PICTS spectrum as a function of applied source drain voltage, V_{SD}, displaced vertically with increasing voltage for clarity. For $V_{SD} = 1V$, a clear peak centered about 106 K can be seen. An Arrhenius plot (Fig. A.1(b)) constructed from a set of different t_1 and t_2 times via Eqns. A.3 and A.4 reveals the trapping level lie approximately 0.182 eV above the valence band. The origin of this discrete trap level is unclear. As V_{SD} is increased, the peak at approximately 106 K disappears. Instead, an asymmetric broad hump centered about 180 K is observed. This continuous non-zero distribution is usually associated with interface states described by a continuum of states within the band gap. It is also noted that changes to V_{SD} significantly shift the broad PICTS signal in temperature, and that a change in the shape of the broad distribution is also apparent. It is tempting to ascribe the observed V_{SD} dependence either to the Poole-Frenkel effect or to phonon-assisted tunneling emission from traps, but no clear tendency (for example in the peak PICTS signal position, or in the characteristic PICTS relaxation times) that would permit an identification of either phenomenon[83] is evident with the data.

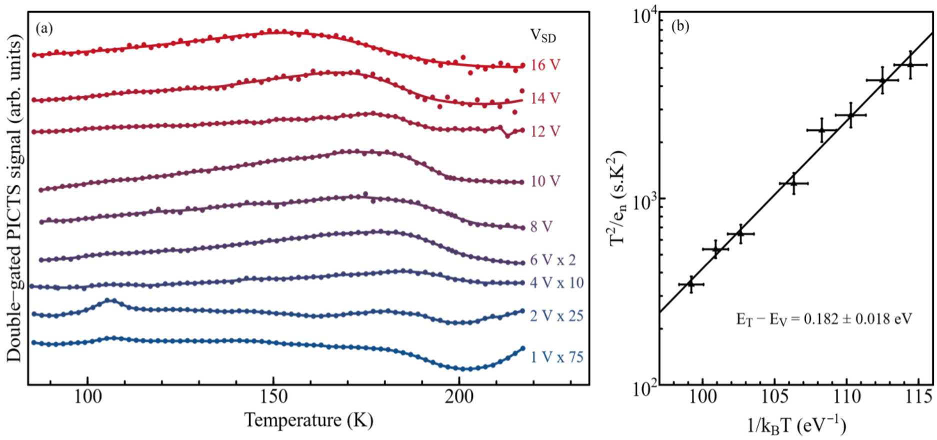

Fig. A.1 (a) Individual PICTS spectrum plotted as a function of V_{SD} displaced vertically for clarity. $t_2/t_1 = 2$, t_1=175 ms, t_2=350 ms. A smoothing spline fit is fitted to the raw PICTS data as a guide the reader's eye. (b) Arrhenius plot constructed from a series of PICTS spectra at $V_{SD} = 1V$.

At elevated temperatures, current transient fluctuations (Fig. A.2(b)) likely due to random telegraph noise start to dominate. As the random telegraph noise amplitude is comparable to the transient amplitude, double boxcar analysis used for PICTS is not appropriate. Therefore, the PICTS spectra are limited to the temperature range of 86 K to 220 K, although measurements up to room temperature were performed. Note also that in the room temperature piezoresponse measurements reported on in chapter 3, the random telegraph noise is averaged out so that and only the mean value of the conductance and capacitance are considered.

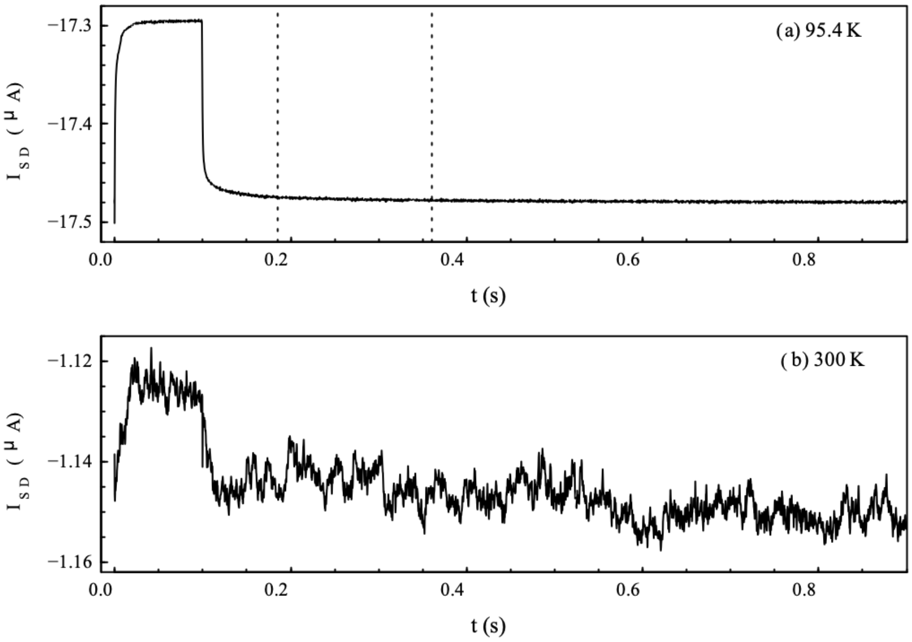

Fig. A.2 Raw PICTS transient measured at (a) 95.4 K and (b) 300.0 K with $V_{SD} = 6V$. A clean transient in (a) is observed, where double Boxcar analysis (dotted lines) is applied to construct the PICTS spectrum (see Fig. A.1). At elevated temperatures in (b), the amplitude of the random telegraph noise is comparable to the photo-induced current transient. Boxcar analysis at high temperatures is therefore avoided

université
PARIS-SACLAY

ÉCOLE DOCTORALE
INTERFACES
Approches Interdisciplinaires :
Fondements, Applications et Innovation

Titre : La piézo-réponse du silicium limitée par la charge d'espace en présence de pièges électroniques

Mots clés : Nanostructures de silicium, piézorésistance, défauts de surfaces, spectroscopie d'impédance, limite de charge d'espace, contrainte mécanique

Résumé : La contrainte mécanique ainsi que les réductions en taille sont deux ingrédients de la feuille de route des semi-conducteurs utilisées pour guider des innovations futures. Cette thèse se concentre sur l'effet de la contrainte sur la résistance du nano-silicium. En utilisant la « spectroscopie d'impédance », on démontre que des changements géants de résistance sous contrainte sont induits par des changements de la dynamique de piégeage de charge sur les défauts de surface. L'utilisation de la spectroscopie d'impédance est cruciale car cet effet n'est présent que lorsque la mesure est effectuée à des fréquences comparables aux taux de piégeage caractéristiques du matériau. Bien qu'un effet géant ne soit pas observé à fréquence nulle, des effets anormaux sont présents à cause de l'injection des porteurs minoritaires depuis les contacts. L'ensemble des résultats conduit à une mise au point claire d'un grand nombre d'effets contradictoires publiés dans la littérature sur le nano-silicium.

Title : Space charge limited piezo-response of silicon in the presence of electronic traps

Keywords : Silicon nanostructures, piezoresistance, surface defects, impedance spectroscopy, space charge limit, mechanical stress

Abstract : Mechanical stress and reductions in device size are two independent ingredients of the semiconductor roadmap used to plan future technological innovations. This thesis addresses the effect of mechanical stress on the resistance of nano-silicon. Using a technique called impedance spectroscopy, it is shown that giant stress-induced changes in the resistance result from changes to the charge trapping dynamics at surface crystal defects. contradictory effects reported in nominally identical nano-silicon devices.

The use of impedance spectroscopy is key since the effect is observed only at measurement frequencies comparable to the characteristic charge trapping rates. Giant effects are not observed using standard measurements of the electrical resistance at zero frequency, although in defect engineered devices minority carrier charge injection from the contacts is shown to result in apparently anomalous stress-induced resistance changes. The results shed new light on the large number of contradictory effects reported in nominally identical nano-silicon devices.

Université Paris-Saclay
Espace Technologique / Immeuble Discovery
Route de l'Orme aux Merisiers RD 128 / 91190 Saint-Aubin, France